Dissertation
submitted to the
Combined Faculties of the Natural Sciences and Mathematics
of the Ruperto-Carola-University of Heidelberg, Germany
for the degree of
Doctor of Natural Sciences

Put forward by
Anke Biekötter
born in Ibbenbüren
Oral examination: 24.07.2019

Know its limits

A global view on Higgs couplings at the LHC

Referees: Prof. Dr. Tilman Plehn

Prof. Dr. Jan Pawlowski

Abstract

After the discovery of a Higgs boson, one of the pivotal tasks of the *Large Hadron Collider* (LHC) is the thorough investigation of the Higgs potential. Its local and global structure is reflected in the couplings of the Higgs boson to other Standard Model particles and in its self-coupling, respectively. Therefore, we can improve our understanding of the Higgs potential by increasing the precision of individual Higgs-coupling measurements and by combining data from different sectors and experiments to obtain a global view.

First, we aim at increasing the sensitivity of an individual search channel, namely *invisible* Higgs decays in weak boson fusion, by including subjet-level information on the tagging jets.

Second, we perform global fits of the Higgs-gauge sector using Standard Model effective field theory, a comprehensive and phenomenologically powerful framework to describe and interpret deviations from the Standard Model. We include LHC Run I+II Higgs and di-boson data in combination with electroweak precision observables and focus on the interplay of fermionic and bosonic dimension-six operators.

Finally, we estimate the reach of a potential 27 TeV LHC-upgrade for Higgs couplings, including di-Higgs production to set limits on the Higgs self-coupling and thereby probe the global structure of the Higgs potential.

Zusammenfassung

Nach der Entdeckung eines Higgs-Bosons gehört die gründliche Untersuchung des Higgspotentials zu den zentralen Aufgaben des *Large Hadron Collider* (LHC). Die lokale und globale Struktur des Higgspotentials spiegelt sich in seinen Kopplungen mit anderen Teilchens des Standardmodells sowie seiner Selbstkopplung wieder. Daher können wir unser Verständnis des Higgspotentials vervollständigen, indem wir einzelne Higgskopplungsmessungen verbessern und die Ergebnisse von verschiedenen Sektoren und Experimenten kombinieren, um so ein globales Bild der Higgskopplungen zeichnen.

Zuerst beschäftigen wir uns mit der Verbesserung der Suche nach *unsichtbaren* Higgszerfällen in der Produktion durch Eichbosonfusion durch die Berücksichtigung von Variablen, welche die Jet-Substruktur beschreiben.

Zweitens führen wir globale Untersuchungen des Higgs-Eich-Sektors im Rahmen von effektiver Feldtheorie durch, welche eine umfassende und phänomenologisch aussagekräftige Beschreibung und Interpretation von Abweichungen vom Standardmodell ermöglicht. Unsere Analyse basiert auf LHC Daten aus den ersten beiden Messdurchgängen für Higgsproduktion und Eichbosonpaarproduktion in Kombination mit elektroschwachen Präzisionsdaten. Der Fokus unserer Untersuchungen liegt auf dem Einfluss von kinematischen Verteilungen und den Wechselwirkungen von fermionischen und bosonischen Dimension-sechs Operatoren.

Schließlich untersuchen wir, wie die Präzision von Higgskopplungsmessungen an einem potenziellen 27 TeV-Upgrade des LHC verbessert werden könnte. Wir berücksichtigen Higgspaarproduktion, um die Higgs-Selbstkopplung und somit die globale Struktur des Higgspotentials zu untersuchen.

Contents

1 Introduction **1**

2 Standard Model Effective Field Theory for the Higgs Sector **3**
2.1 The Higgs sector of the Standard Model . . . 3
2.2 Effective field theory . . . 5
2.3 Constructing SMEFT from the bottom-up . . . 6
2.3.1 Bosonic operators . . . 8
2.3.2 Fermionic operators . . . 9
2.4 Phenomenology of dimension-six operators . . . 11
2.5 Constraining SMEFT operators . . . 13
2.6 The Δ-framework . . . 16

3 Global Fits **19**
3.1 A measure of goodness-of-fit . . . 19
3.1.1 Likelihood ratios and statistical tests . . . 21
3.1.2 Combination of likelihood functions . . . 22
3.1.3 Correlations of measurements and uncertainties . . . 23
3.2 Fitting techniques . . . 24
3.2.1 Grid . . . 24
3.2.2 Migrad . . . 24
3.2.3 Markov chains . . . 25
3.3 Toy Monte Carlos . . . 26

4 Tagging Jets in Invisible Higgs Searches **27**
4.1 Introduction . . . 27
4.2 Dominant backgrounds . . . 29
4.3 Tagging-jet size . . . 31
4.4 Tagging-jet parton content and quark/gluon discrimination . . . 34
4.5 Performance and triggering . . . 39
4.6 Conclusion and outlook . . . 41

5 A Global View on the Higgs-Gauge Sector for LHC Run II **43**
5.1 Introduction . . . 43
5.2 Relevant SMEFT operators . . . 44
5.3 Constraints from the QCD and top sectors . . . 45
5.4 Fitting framework and data set . . . 47
5.5 Global Higgs-gauge analysis in the SMEFT framework . . . 51

5.6 Conclusion and outlook 55

6 A Global View on the Higgs-Gauge Sector at 27 TeV **57**
6.1 Introduction 57
6.2 Global Higgs analysis in terms of coupling modifiers 58
6.3 Global Higgs-gauge analysis in the SMEFT framework 61
6.4 Constraining the Higgs self-interaction in a global fit 64
6.5 Conclusion and outlook 66

7 Conclusion and Outlook **69**

Acknowledgments **73**

A Appendix **75**
A.1 EFT basis 75
A.2 Combination of likelihoods 75
A.3 Invisible Higgs decays - Zh benchmark 77

References **79**

Preface

The research presented in this thesis was conducted at the Institute for Theoretical Physics at Heidelberg University from October 2016 to May 2019. The contents of the Chapters 4-6 are based on work in collaboration with other authors and have previously been published as

[1] A. Biekötter, F. Keilbach, R. Moutafis, T. Plehn and J. Thompson, "Tagging Jets in Invisible Higgs Searches", *SciPost Phys.* **4** (2018) no. 6, 035, `arXiv:1712.03973 [hep-ph]`

[2] A. Biekötter, D. Gonçalves, T. Plehn, M. Takeuchi and D. Zerwas, "The Global Higgs Picture at 27 TeV", *SciPost Phys.* **6** (2019) no. 2, 024, `arXiv:1811.08401 [hep-ph]`

[3] A. Biekötter, C. Corbett, T. Plehn, "The Gauge-Higgs Legacy of the LHC Run II", to appear in *SciPost Phys.*, `arXiv:1812.07587 [hep-ph]`.

1 | Introduction

The motivation behind the prediction of a fundamental scalar particle in the Standard Model (SM), the Higgs boson, was to grant a mechanism for the generation of the masses of the electroweak gauge bosons via electroweak symmetry breaking (EWSB) [4–6]. The discovery of a Higgs boson at the Large Hadron Collider (LHC) [7, 8] strongly hints at EWSB indeed being the mechanism behind the mass generation of the SM particles. One of the pivotal tasks of the LHC and future colliders is to probe both the local and global structure of the Higgs potential, which is reflected in the couplings of the Higgs boson to other SM particles and in its self-coupling, respectively. In this thesis, we present a global view on Higgs couplings at the LHC to extend our understanding of the EWSB sector and to set universal constraints on new physics that might be hiding in it.

The couplings of the Higgs boson to other SM particles manifest the local properties of its potential in the vicinity of the electroweak vacuum after EWSB. LHC measurements of the various predicted Higgs production and decay channels are crucial to explore and constrain these couplings. So far, the (preliminary) results of LHC Run II are compatible with the couplings predicted for the SM Higgs boson [9, 10]. Its four dominant production modes at the LHC have been observed with no significant deviation from the SM expectations. Moreover, LHC Run II has established the Higgs decays into the kinematically accessible third generation fermions in addition to the decays into pairs of the electroweak gauge bosons. Tight constraints have been set on the Higgs branching ratio to a pair of muons, to $Z\gamma$ or to *invisible*, i.e. to undetectable, particles.

While single-Higgs production measurements probe the local structure of the Higgs potential and provide only indirect constraints on the realization of EWSB, the examination of the global structure of the potential requires (at least) di-Higgs production. This process is sensitive to the trilinear Higgs self-coupling, which the LHC will only constrain to multiple times its SM value, even after its high-luminosity run [11]. For measurements in the percent range, future colliders are required [12, 13]. In any collider experiment, precise measurements of Higgs couplings to other SM particles are a crucial ingredient for the extraction of Higgs self-coupling from multi-Higgs production [2, 11, 12], which emphasizes the relevance of the local properties of the Higgs potential on a global scale.

The exploration of the structure of the Higgs potential is not only indispensable to gain a deeper understanding of EWSB on a fundamental level, it also provides important constraints for physics beyond the SM (BSM). The motivations for extension of the SM Higgs sector and their impact on Higgs couplings are versatile: The Higgs boson might be the mediator to a dark sector [14–32] resulting in, for instance, an increased Higgs branching ratio to invisible particles and global rescalings of its couplings to other SM particles. A modified Higgs potential or an extended Higgs sector has direct implications for vacuum stability [33–36] and electroweak baryogenesis [37–49], which requires a strong first-order phase transition to ensure a deviation from thermal equilibrium [50]. If in fact electroweak baryogenesis is the mechanism responsible for the baryon-antibaryon asymmetry in the universe, the remnants of the electroweak phase transition may have observable consequences, e.g. , in the form of gravitational waves [38, 51–53].

Driven by the question what current data reveal about the EWSB sector and new physics that might be hiding in it, in this thesis we aim at increasing the precision of Higgs-coupling measurements and combining them in a comprehensive framework. This requires us to rethink the way we perform, interpret and combine experimental analyses in a way that fully exploits the available data. To tackle

this challenge, we take a multi-prong approach: First, we focus on the improvement of an individual Higgs-production and decay channel by applying modern analysis techniques. Second, we perform global analyses of the Higgs-gauge sector for the LHC and a potential future upgrade of the LHC in a model-independent framework.

Data driven analysis techniques are applied to the experimental analyses of individual search channels more and more frequently. They replace simple cut-and-count strategies and vetoes by more advanced multivariate analyses and machine learning to profit from to the full information provided by the data. A prime test bed for the application of these new approaches is given by jets, not only because the LHC generates ample of them, but also because their substructure relies on relatively simple physical principles. In Chapter 4, we apply a multivariate analysis to the tagging jets in weak-boson-fusion Higgs production with an invisible decay of the Higgs boson. Based on the observation that the tagging jets in the weak-boson-fusion Higgs signal are more likely to be quark-initiated, we examine the potential of variables targeting quark/gluon discrimination to suppress the gluon-dominated QCD backgrounds.

An economic use of the available Higgs data calls for a combination of measurements from different experiments, sectors and scales. Such comprehensive study can aid in making small effects of new physics visible on a global scale and demands for a universal parametrization of those. Historically, deviations from the SM Higgs couplings were described by coupling modifiers in the Δ-framework [54] (or the closely related κ-framework introduced in Ref. [55]). A phenomenologically more powerful framework to probe the data for hints of possible BSM physics in an almost model-independent way is given by SM effective field theory (SMEFT) [56–61], introduced in Chapter 2. It directly links the Higgs and gauge sectors and allows for the modelling of modified Lorentz structures. We confront the SMEFT framework with data using the fitting tool SFitter [62]. As discussed in Chapter 3, SFitter allows for an exhaustive treatment of statistical, systematic and theoretical uncertainties as well as their correlations.

Motivated by the experimental advances of LHC Run II, we perform a global fit of the Higgs-gauge sector based on Higgs and di-boson measurements as well as electroweak precision data in Chapter 5. We include momentum-related kinematic distributions and examine the impact of the different LHC Run II measurements on the reach of our global analysis in detail. On the theory side, we broaden our view on the Higgs sector by expanding the set of considered dimension-six operators from 10 to 18 with respect to previous SFitter analyses [63, 64]. This extension of our operator set will bring us a significant step closer to a global SMEFT fit at dimension six. We discuss how the additional fermionic Higgs-gauge operators have a relevant impact on a global fit of the Higgs-gauge sector despite the strong constraints from electroweak precision data.

An upgrade of the LHC to an energy of 27 TeV is among the realistic proposals for future colliders following the high-luminosity LHC era. The capability of such a 27 TeV hadron collider to produce a statistically relevant number of di-Higgs events prompts us to perform a global fit of the Higgs-gauge sector including a modified Higgs potential. In Chapter 6, we assess the sensitivity of a high-energy upgrade of the LHC to the Wilson coefficients of dimension-six operators in the SMEFT framework. We thoroughly examine the correlations of operators influencing the extraction of the trilinear Higgs self-coupling and thereby probe the relevance of precise constraints on the local properties of the Higgs potential for the study of its global structure.

In Chapter 7, we will summarize our results and give an outlook to further improvements and extensions of the concepts discussed in this thesis. Each of the lines of research mentioned above will aid in constructing a global view of Higgs couplings at the LHC as well as its proposed future upgrade and will bring us one step closer to probing if EWSB is indeed described by the simple structure of the SM Higgs potential. The derived limits on Higgs couplings in the SMEFT framework can be mapped onto constraints for UV-complete BSM models [65, 66]. Furthermore, they provide a key ingredient for future tests of the global structure of the Higgs potential. In summary, the thorough investigation of Higgs couplings at the LHC is crucial to gain a deeper understanding of the structure of the Higgs sector and EWSB on a fundamental level.

2 | Standard Model Effective Field Theory for the Higgs Sector

The discovery of a scalar particle with a mass of $m_h = 125$ GeV at the LHC [7, 8] and subsequent precision analyses of this new boson suggest that it is indeed the Higgs boson of the Standard Model [4–6] or behaves very similar to it. Apart from confirming our ideas about the role of symmetries in theories of fundamental interactions, findings to date – or more so their absence – have led to a shift in the focus of experimental analyses [67]. Increasingly, targeted searches for new particles or effects relying on "smoking gun" signatures are replaced by more holistic precision tests of Standard Model dynamics in ever more extreme phase space regions. Confronted with a large abundance of models describing new physics at the TeV-scale on the one side and a plethora of experimental precision measurements on the other side, our aim is to describe deviations from the Standard Model expectations in a model independent and reproducible way. A framework apt to address this challenge of a comprehensive description of new physics is effective field theory (EFT) [57–61]. In Higgs physics, effective field theories can be used to model the low energy effects of TeV-scale theories, describing not only small deviations from the SM couplings in magnitude, but also modifications of their Lorentz structures.

This chapter is loosely based on Refs. [68, 69] and is organized as follows: We will first introduce the Higgs sector of the SM in Section 2.1 to establish the notations and give an overview of the dominant Higgs-production modes at the LHC and its decays. In Section 2.2, we will introduce the EFT framework from the top-down using Fermi's theory of the muon decay as an example. Then, in Section 2.3, we will take the opposite approach and construct a basis of dimension-six operators from the bottom up. We will discuss the phenomenology of the dimension-six operators relevant for Higgs physics in Section 2.4 and describe the relevant physical processes constraining our set of dimension-six operators in Section 2.5. In Section 2.6, we will introduce the Δ–framework as an alternative approach to describe deviations from the SM Higgs couplings.

2.1 The Higgs sector of the Standard Model

The electroweak sector of the SM is described as a gauge theory with an $SU(2)_L \times U(1)_Y$ symmetry [70–73]. Electroweak symmetry breaking provides a mechanism to generate the masses of the W and Z boson without breaking this symmetry explicitly. In the SM, EWSB is realized by a complex scalar Higgs doublet ϕ [4–6]. The SM Higgs sector is described by the following Lagrangian

$$\begin{aligned}
\mathcal{L}_{\text{Higgs}} &= (D_\mu \phi)^\dagger (D^\mu \phi) - V(\phi) + \mathcal{L}_{\text{Yukawa}} \,, \\
V(\phi) &= \mu^2 \phi^\dagger \phi + \lambda (\phi^\dagger \phi)^2 \,, \\
\mathcal{L}_{\text{Yukawa}} &= - \sum_{\text{generations}} \left(y_u \begin{pmatrix} \overline{u} \\ \overline{d} \end{pmatrix}_L \tilde{\phi}\, u_R + y_d \begin{pmatrix} \overline{u} \\ \overline{d} \end{pmatrix}_L \phi\, d_R + y_\ell \begin{pmatrix} \overline{\nu} \\ \overline{\ell} \end{pmatrix}_L \phi\, \ell_R + \text{h.c.} \right) \,,
\end{aligned} \tag{2.1}$$

with real parameters μ^2 and λ in the Higgs potential, complex Yukawa couplings y_i, which are matrices in flavor space, and $\tilde{\phi} = i\sigma_2\phi^*$. The covariant derivative is defined as

$$D_\mu\phi = \left(\partial_\mu + ig\frac{\sigma^a}{2}W_\mu^a + i\frac{g'}{2}B_\mu\right) , \tag{2.2}$$

with W_μ^a and B_μ denoting the gauge bosons of the $SU(2)_L$ and $U(1)_Y$ gauge groups, their respective coupling constants g and g', and σ^a being the Pauli matrices. If the quadratic term in the Higgs potential in Eq. (2.1) is negative, i.e. $\mu^2 < 0$, the neutral component of the scalar doublet acquires a non-zero vacuum expectation value (vev) $v = \sqrt{-\mu^2/\lambda}$ and induces the spontaneous breaking from the SM gauge symmetry to $U(1)_Q$. The Higgs doublet can then be written in terms of the physical Higgs field h, its vev v and the would-be Goldstone bosons w^i [74, 75]

$$\phi = \frac{1}{\sqrt{2}}\begin{pmatrix} -w^2 - iw^1 \\ v + h + iw^3 \end{pmatrix} . \tag{2.3}$$

The Goldstone bosons provide the longitudinal degrees of freedom of the massive gauge bosons and we can write the Higgs doublet in the Lagrangian in Eq. (2.1) in the unitary gauge $\phi = \frac{1}{\sqrt{2}}(0,\, v+h)^T$. As the physical Higgs field h and its vev always come in the combination $v+h$ we directly see that the same terms that induce the couplings of fermions and the weak bosons to the Higgs will also generate their masses. Therefore, there is a proportionality between the couplings of the Higgs boson to other SM particles x (which obtain their masses via EWSB) and their masses $g_x \sim m_x$. The trilinear and quartic self-couplings of the Higgs boson are proportional to the parameter λ, rendering those couplings sensitive to the structure of the Higgs potential in Eq. (2.1).

Higgs production and decays

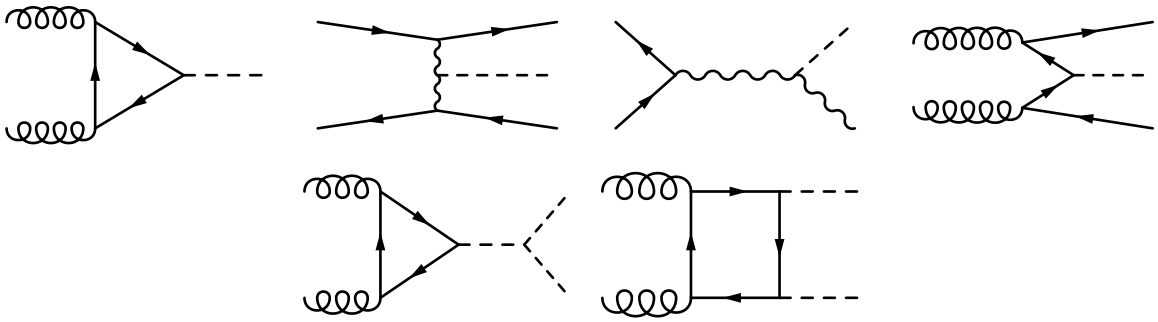

Figure 2.1: Leading order Feynman diagrams of the dominant production modes of the Higgs boson at the LHC. Upper row: gluon fusion (left), weak boson fusion (middle left), associated production with a weak boson (middle right) and $t\bar{t}h$ production (right). Lower row: Di-Higgs production.

As the Higgs boson predominantly couples to heavy particles, its dominant production modes involve the top quark and the weak Z and W bosons. At the LHC, the main production processes of the Higgs boson are gluon fusion (ggF), weak boson fusion (WBF), associated production with a Z or W boson and production in association with a pair of top quarks. The Feynman diagrams for the dominant (single) Higgs-production modes at the LHC are shown in (the upper panel of) Fig. 2.1. We list their production cross section at a $\sqrt{s} = 13\,\text{TeV}$ pp-collider in Tab. 2.1.

We can probe the Higgs self-coupling λ and obtain insight on the structure of the Higgs potential in Eq. (2.1) by measuring di-Higgs production. The relevant Feynman diagrams for this process are given in the lower panel of Fig. 2.1. Di-Higgs production is not only phase-space suppressed by the mass of the Higgs bosons, it suffers in addition from the negative interference between the two dominant diagrams, rendering its cross section accidentally small. In fact, the cross section is around a factor 17 smaller than for Higgs production in association with a top quark pair, see Tab. 2.1, despite the fact that $t\bar{t}h$ production suffers from an even stronger phase-space suppression and di-Higgs production

production channel	cross section [pb]
ggF	48.58
WBF	3.782
Wh	1.373
Zh	0.8839
tth	0.5071
hh	0.03105

Table 2.1: Production channels of the Higgs boson and their SM cross-section predictions for LHC Run II ($\sqrt{s} = 13\,\text{TeV}$) [76].

only involves one additional coupling of $\lambda \sim 0.13$ or $y_t \sim 1$. The strong negative interference of the two diagrams contributing to di-Higgs production makes this process especially sensitive to new physics with modified Higgs sectors which might reduce such cancellations and enhance its cross section.

Since the Higgs boson couples to all massive particles of the SM, it has a broad spectrum of decay modes. It prefers to decay into a pair of the heaviest particles allowed by phase space which is a pair of bottom quarks, see Fig. 2.2. The decay to a pair of Z or W bosons is suppressed by one of the bosons having to be off-shell due to their masses. The decay of a Higgs boson to a pair of gluons, photons or $Z\gamma$ is only possible via loop diagrams. Given the large QCD backgrounds at a hadron collider, the dominant (hadronic) decay modes of the Higgs boson are not the most sensitive experimental signatures. Despite their low branching ratios of 0.2 % and 0.3 % respectively, the di-photon $\gamma\gamma$ and $ZZ^* \to 4\ell$ decay modes of the Higgs boson are considered its *golden channels*.

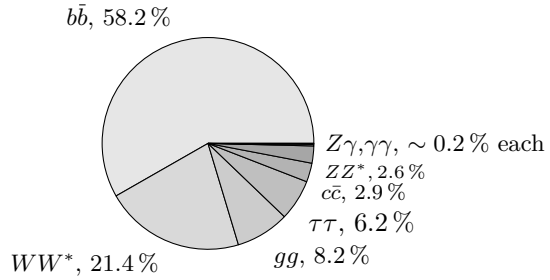

Figure 2.2: SM predictions for the branching ratios of the Higgs boson [76].

2.2 Effective field theory

Effective field theory provides a phenomenologically powerful and theoretically sound framework to describe new physics in an (almost) model-independent way [67]. It is based on the assumption of a hierarchy of scales, i.e. the idea that new physics appears at a scale Λ much larger than the energy scale E of the physical process under consideration (and accessible by experiments). An effective field theory aims at describing all effects relevant at a given scale, while neglecting those which only play a role at a significantly different scale. Applied to particle physics, this means that an effective field theory describes the effects of new particles and structures at an energy scale where these can not (yet) be resolved. Heavy degrees of freedom of a new physics theory are integrated out and their low-energy effects are described by fixing the (propagating) particle content and the underlying symmetry structure and constructing new operators with mass-dimension $d > 4$ from it.

As the action $S = \int \mathrm{d}^4x\, \mathcal{L}(x)$ of a quantum field theory is dimension-less, all terms in a Lagrangian need to have mass dimension $d = 4$. Therefore, in an effective field theory all operators of mass dimension $d > 4$ need to be suppressed by powers of a (new physics) scale Λ which is usually assumed

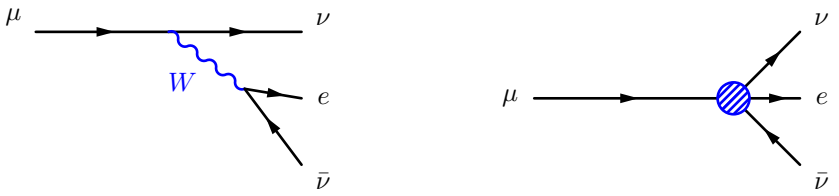

Figure 2.3: The muon decay as described by the full theory of weak interactions (left) and by an effective theory after integrating out the W boson (right).

to be universal. The Lagrangian of an effective field theory is thus given by [56–61]

$$\mathcal{L}_{\text{EFT}} = \sum_i \frac{f_i}{\Lambda^{d-4}} \mathcal{O}_i^{(d)} \,, \tag{2.4}$$

where f_i denote the Wilson coefficients corresponding to the higher-dimensional operators $\mathcal{O}_i$. The contribution of each operator $\mathcal{O}_i^{(d)}$ to amplitudes of physical processes at an energy scale of order $\mathcal{O}(E)$ has a maximum scaling of $(E/\Lambda)^{(d-4)}$. When we assume a large new physics scale Λ, this ratio is small $E/\Lambda \ll 1$ by construction and the effective field theory describes small deviations from the SM predictions, except for observables that vanish or are suppressed by small parameters within the SM [77]. Given a large new physics scale Λ, it is often justified to truncate the effective theory at a given dimension, typically at dimension six for EFTs based on the SM field content, since higher-dimensional terms are suppressed by additional powers of Λ.

An illustrative top-down example for an effective theory, i.e. starting from a full, UV-complete new physics model and integrating out the heavy degrees of freedom [78,79], is Fermi's theory of the muon decay [80]. We display the corresponding Feynman diagrams in Fig. 2.3. At energy scales much lower than the mass of the W boson, $E \ll \Lambda = m_W$, the W boson can be integrated out and the decay of the muon is effectively described by a four-point interaction of fermions. This is equivalent to approximating the W boson propagator in the decay for low momenta p

$$\frac{g^2}{p^2 - m_W^2} \quad \to \quad -\frac{g^2}{m_W^2} \,, \tag{2.5}$$

which at an energy scale of the mass of the muon is a very good approximation $m_\mu^2/m_W^2 \approx 10^{-6}$. The effective Lagrangian of the Fermi theory of the muon decay in terms of a dimension-six operator reads [77]

$$\mathcal{L}_{\text{EFT}} \supset c^{(6)} \left(\bar{e}\gamma_\alpha P_L \nu_e\right) \left(\bar{\nu}_\mu \gamma^\alpha P_L \mu\right) + \text{h.c.}, \qquad c^{(6)} = -\frac{g^2}{2m_W^2} = -\frac{2}{v^2} \,. \tag{2.6}$$

At energies $E \ll m_W$, this four-point contact interaction of the muon decay is a valid approximation for the full electroweak process described by the SM.

2.3 Constructing SMEFT from the bottom-up

In the previous section, we have seen the textbook example for the construction of a top-down EFT, the Fermi theory of the muon decay. Starting from a full theory, in this case the electroweak sector of the SM, we have constructed an effective low-energy description of this theory, valid for $E < m_W$, describing the muon decay with an effective four-fermion operator at dimension six.

In this section, we want to go the opposite way and construct an effective field theory bottom-up. If we restrict ourselves to the field content of the SM, the only operator that we can construct at dimension five is the *Weinberg operator* $(\bar{L}_L \tilde{\phi}^*)(\tilde{\phi}^\dagger L_L)$ which, however, violates lepton number conservation. Consequently, if we want to preserve baryon and lepton number conservation, operators need to be at least of dimension six. Our aim for this section is to construct a complete basis of operators based only on the following five assumptions:

1. **Field content:** We will build new operators from the SM fields only.
2. **Symmetries:** We will only allow operators which are invariant under the SM gauge group $SU(3)_C \times SU(2)_L \times U(1)_Y$ and under proper orthochronous Poincaré transformations. In addition, we require lepton and baryon number conservation.
3. **Counting scheme:** We only keep operators up to mass dimension six.
4. **Flavor:** We assume a universal flavor structure, i.e. we will not distinguish between the different fermion families.
5. **Higgs sector:** We assume the Higgs boson h and the would-be Goldstone bosons to form an $SU(2)_L$ doublet as given in Eq. (2.3), limiting ourselves to SM EFT (or *linear EFT*) in contrast to *non-linear Higgs EFT* which is often simply denoted *Higgs EFT* (HEFT).

Respecting those assumptions and barring Hermitian conjugation, we can construct 59 operators [56–61, 81–86] and our effective Lagrangian is given by

$$\mathcal{L}_{\text{EFT}} = \mathcal{L}_{\text{SM}} + \sum_i^{59} \frac{f_i}{\Lambda^2} \mathcal{O}_i^{(6)} \,. \tag{2.7}$$

The definition of an operator basis is not unique, as operators can be translated into one another using field redefinitions, Fierz identities and integration by parts. Popular basis choices include the *Warsaw* basis [60], the *Strongly interacting Little Higgs* (SILH) basis [87,88] and the *Hagiwara-Ishihara-Szalapski-Zeppenfeld* (HISZ) basis [84]. Here, we will use a convention based on the latter and will follow the approach of Ref. [89,90] for its definition, starting from a set of operators with three redundancies and explicitly using the equations of motion to remove operators with blind directions to electroweak precision data.

We can classify the 59 operators in our basis according to their field content in terms of gauge fields strength tensors X, Higgs doublet ϕ and fermion fields ψ as well as derivatives ∂/D and their properties. In the following, we will list the categories of dimension-six operators and restrict ourselves to a subset of those which we will discuss in more detail. We can loosely classify the operators into two sets, see Tab. 2.2: operators containing bosonic fields only (17 operators) and those containing fermionic fields as well (42 operators).

Out of the 17 purely bosonic operators, 6 are CP violating. We will refer to them as ϕ^2X^2 and ϕ^2XD^2 or $\phi^2X\tilde{X}$ and $\phi^2\tilde{X}D^2$ using the tilde to denote the dual field strength. The remaining CP-even operators can further be subclassified into operators containing gauge fields only (X^3, 2 operators), operators containing the Higgs field only (ϕ^6 and $\phi^4\partial^2$, 2 operators) and operators consisting of both gauge and Higgs fields (ϕ^2X^2 and ϕ^2XD^2, 7 operators). The set of fermionic operators consists of 4-fermion operators (ψ^4, 25 operators), operators containing fermions and the Higgs ($\phi^3\psi^2$, 3 operators), fermionic Higgs-gauge operators ($\phi^2\psi^2D$, 6 operators) and fermionic Higgs-gauge operators with a tensor Lorentz structure ($\phi\psi^2X$, 8 operators) which we will also refer to as dipole operators.

bosonic		#	fermionic		#
gauge only	X^3	2	4-fermion	ψ^4	25
Higgs only	ϕ^6, $\phi^4\partial^2$	2	Higgs-fermion	$\phi^3\psi^2$	3
Higgs-gauge	ϕ^2X^2, ϕ^2XD^2	(8) 7	Higgs-gauge-fermion	$\phi^2\psi^2D$	(8) 6
CP-odd	$\phi^2X\tilde{X}$, $\phi^2\tilde{X}D^2$	6	dipole	$\phi\psi^2X$	8

Table 2.2: Overview of dimension-six operator ordered by field content and structure. We have grayed out operators which are mostly irrelevant for Higgs physics. We also list the number of operators of a given structure (before using the equations of motion).

Not all of the operators in Tab. 2.2 are relevant for Higgs physics and we will therefore only consider a subset of them in the following. Since we expect CP violation to be measured in a dedicated analysis rather than a global fit [91,92], we restrict the set of operators to the P-even and C-even ones and only list CP-odd operators in Eq. (A.1) for completeness. We also neglect all operators describing four-fermion contact interactions except $\mathcal{O}_{LLLL}$ defined in Eq. (2.13). 4-fermion operators do not contribute to any of the main Higgs-production modes, see Section 2.1, and we only keep $\mathcal{O}_{LLLL}$ because of its influence on the well measured Fermi constant G_F which is relevant for our study of electroweak precision data in Section 2.5. Dipole operators flip the fermion chirality due to their Lorentz structure. Their interference with the SM amplitudes is hence small. As they are also expected to be suppressed by the fermion Yukawa, we will generally neglect all dipole operators except $\mathcal{O}_{tG}$ which we will come back to in Eq. (2.15). For current constraints on dipole operators involving light or heavy quarks see e.g. Refs. [93–95].

We will now discuss the bosonic, Higgs-fermion and Higgs-gauge fermion operators in more detail, focussing especially on the vertices they are contributing to. In Section 2.4, we will focus on the phenomenology of the operators on the Lagrangian level and then discuss processes which are capable of setting meaningful limits on those in Section 2.5.

2.3.1 Bosonic operators

operator	$Hf\bar{f}$	HHH	HVV	VVV
$\mathcal{O}_{\phi 1}$	×	×	×	×
$\mathcal{O}_{\phi 2}$	×	×	×	
$\mathcal{O}_{\phi 3}$		×		
$\mathcal{O}_{\phi 4}$	×	×	×	
$\mathcal{O}_{WW}$			×	
$\mathcal{O}_{BB}$			×	
$\mathcal{O}_{W}$			×	×
$\mathcal{O}_{B}$			×	×
$\mathcal{O}_{BW}$			×	×
$\mathcal{O}_{WWW}$				×

Table 2.3: List of bosonic dimension-six operators and their effects on couplings. Some of the operators also contribute to $HHHH$, $HVVV$, $HHVV$ or $VVVV$, but we limit ourselves to listing interactions which are phenomenologically relevant for the processes studied in the following.

We start our discussion of the dimension-six operators by listing the operators containing Higgs or gauge fields only. There are six CP-odd bosonic operators in our basis, see to Eq. (A.1), which we neglect in our analysis. We explicitly write down 12 CP-conserving operators and will later use the equations of motion, Eq. (2.14), to remove one of them. There are two operators which consist of gauge fields only

$$\mathcal{O}_{WWW} = \mathrm{Tr}\left(\hat{W}_{\mu\nu}\hat{W}^{\nu\rho}\hat{W}^{\mu}_{\rho}\right) \qquad \mathcal{O}_{G} = f^{abc}G^{a\rho}_{\nu}G^{b\nu}_{\lambda}G^{c\lambda}_{\rho} \tag{2.8}$$

and eight operators containing Higgs and gauge fields

$$\begin{aligned}
\mathcal{O}_{GG} &= \phi^\dagger\phi\, G^a_{\mu\nu}G^{a\mu\nu} & \mathcal{O}_{W} &= (D_\mu\phi)^\dagger\hat{W}^{\mu\nu}(D_\nu\phi) & \mathcal{O}_{\phi 1} &= (D_\mu\phi)^\dagger\phi\,\phi^\dagger D^\mu\phi \\
\mathcal{O}_{WW} &= \phi^\dagger\hat{W}_{\mu\nu}\hat{W}^{\mu\nu}\phi & \mathcal{O}_{B} &= (D_\mu\phi)^\dagger\hat{B}^{\mu\nu}(D_\nu\phi) & \mathcal{O}_{\phi 4} &= \phi^\dagger\phi\,(D_\mu\phi)^\dagger D^\mu\phi \\
\mathcal{O}_{BB} &= \phi^\dagger\hat{B}_{\mu\nu}\hat{B}^{\mu\nu}\phi & \mathcal{O}_{BW} &= \phi^\dagger\hat{B}_{\mu\nu}\hat{W}^{\mu\nu}\phi\,.
\end{aligned} \tag{2.9}$$

The covariant derivative acting on the Higgs is defined in Eq. (2.2) and the hatted field strengths are rescaled with extra coupling factors $\hat{B}_{\mu\nu} = ig'B_{\mu\nu}/2$ and $\hat{W}_{\mu\nu} = ig\sigma^a W^a_{\mu\nu}/2$ to ensure that they

contribute to vertices with the same coupling orders as their SM counterparts, i.e. that for instance hWW couplings are modified by factors $(1 + f_x\, c)$ rather than $(1 + f_x\, c/g)$ with arbitrary c. This rescaling is motivated by our expectations from known UV-completions. It has, however, no effect on our analysis or its interpretation. Two operators contain the Higgs field only

$$\mathcal{O}_{\phi 2} = \frac{1}{2}\partial^\mu(\phi^\dagger\phi)\partial_\mu(\phi^\dagger\phi) \qquad\qquad \mathcal{O}_{\phi 3} = -\frac{1}{3}(\phi^\dagger\phi)^3\,. \tag{2.10}$$

The effect of the operators in Eqs. (2.8)-(2.10) on Higgs and gauge interactions is summarized in Tab. 2.3. All operators in Eqs. (2.9) and (2.10) affect Higgs interactions. Moreover, many of the operators in Eq. (2.9) and the operator $\mathcal{O}_{WWW}$ lead to anomalous triple gauge couplings and can therefore be constrained using di-boson measurements. We will discuss this source of constraints in more detail in Section 2.5. For a more detailed discussion of the bosonic operators, including an analysis of their (non-SM) Lorentz structures, see Ref. [63, 90, 96, 97]. We will discuss the limits on the operator $\mathcal{O}_G$ in Eq. (2.12) in Section 5.3.

Some of the operators in Eq. (2.9) contribute to the two-point functions of the electroweak gauge bosons. For the operators $\mathcal{O}_{WW}$ and $\mathcal{O}_{ZZ}$ these additional contributions can be removed by a trivial redefinition of the fields and couplings. For $\mathcal{O}_{\phi 1}$ and $\mathcal{O}_{BW}$ however, the situation is more involved and their additional contributions to the kinetic terms or mass terms of the electroweak gauge bosons cannot be fully removed by redefinitions of the fields, as explained e.g. in Ref. [90]. The operator $\mathcal{O}_{BW}$ contributes to W^3–B mixing, while the operator $\mathcal{O}_{\phi 1}$ contributes to the Z boson mass, but not the W boson mass. They are therefore strongly constrained by the S oblique parameter and $\Delta\rho$, or the T oblique parameter, respectively [98, 99]. We will discuss electroweak precision data as a source of constraints on dimension-six operators in Section 2.5. The operator $\mathcal{O}_{\phi 2}$ contributes to the kinetic term of the Higgs field and requires its redefinition, if we want to keep the canonical form of the kinetic term. We will discuss the phenomenology of this operator, resulting in a global shift of the Higgs couplings to other particles and the introduction of a momentum-dependent Higgs self-coupling, in Section 2.4. The operator $\mathcal{O}_{\phi 3}$ is particularly relevant because of its modification of the Higgs potential. We will come back to it in Section 6.4, when we are including the Higgs self-coupling in a global fit. Using the equations of motion for the Higgs and gauge bosons [60] will allow us to remove three operators from our basis, see Eq. (2.14). To avoid blind directions to electroweak precision data [89, 90], we will later choose to remove $\mathcal{O}_{\phi 4}$ from our set of operators.

2.3.2 Fermionic operators

After the discussion of operators involving only the Higgs and the electroweak gauge fields, we will now study a second group of operators containing fermionic (and bosonic) fields. We will distinguish between operators containing fermions and the Higgs only, operator containing fermions, the Higgs and gauge fields with SM-like Lorentz structures, four-fermion operators and finally dipole operators, containing fermions, the Higgs and gauge fields and non-SM like Lorentz structures.

We begin the discussion of with fermionic operators affecting the coupling of the Higgs to fermions and result in Yukawa-like interactions. Restricting ourselves to the third family of fermions, there are three such operators

$$\mathcal{O}_{e\phi,33} = \phi^\dagger\phi\; \bar{L}_3\phi e_{R,3} \qquad \mathcal{O}_{u\phi,33} = \phi^\dagger\phi\; \bar{Q}_3\tilde{\phi}u_{R,3} \qquad \mathcal{O}_{d\phi,33} = \phi^\dagger\phi\; \bar{Q}_3\phi d_{R,3}\,. \tag{2.11}$$

In addition we consider the group of fermionic Higgs-gauge operators. Assuming flavor universality, we

start from a list of eight operators and will reduce their number to six using the equations of motion

$$\begin{aligned}
\mathcal{O}_{\phi Q}^{(1)} &= \phi^\dagger (i\overleftrightarrow{D}_\mu \phi)(\bar{Q}\gamma^\mu Q) & \mathcal{O}_{\phi Q}^{(3)} &= \phi^\dagger (i\overleftrightarrow{D}^a_\mu \phi)(\bar{Q}\gamma^\mu \frac{\sigma_a}{2} Q) \\
\mathcal{O}_{\phi L}^{(1)} &= \phi^\dagger (i\overleftrightarrow{D}_\mu \phi)(\bar{L}\gamma^\mu L) & \mathcal{O}_{\phi L}^{(3)} &= \phi^\dagger (i\overleftrightarrow{D}^a_\mu \phi)(\bar{L}\gamma^\mu \frac{\sigma_a}{2} L) \\
\mathcal{O}_{\phi u}^{(1)} &= \phi^\dagger (i\overleftrightarrow{D}_\mu \phi)(\bar{u}_R\gamma^\mu u_R) \\
\mathcal{O}_{\phi d}^{(1)} &= \phi^\dagger (i\overleftrightarrow{D}_\mu \phi)(\bar{d}_R\gamma^\mu d_R) \\
\mathcal{O}_{\phi e}^{(1)} &= \phi^\dagger (i\overleftrightarrow{D}_\mu \phi)(\bar{e}_R\gamma^\mu e_R) \\
\mathcal{O}_{\phi ud}^{(1)} &= \tilde{\phi}^\dagger (i\overleftrightarrow{D}_\mu \phi)(\bar{u}_R\gamma^\mu d_R)
\end{aligned} \tag{2.12}$$

The operator $\mathcal{O}_{\phi ud}^{(1)}$ contains the charged current $\bar{u}_R\gamma^\mu d_R$ [100–103]. Given the known flavor physics constraints and the fact that it has no equivalent Standard Model structure to interfere with, we will ignore this operator in our analyses.

An important phenomenological consequence of the operators in Eq. (2.12) is the generation of anomalous weak-boson couplings to fermions, see Tab. 2.4. In this table, we have also included the bosonic operators $\mathcal{O}_{\phi 1}$ and $\mathcal{O}_{BW}$ because of their influence on weak-boson couplings to fermions after the field redefinitions. The operators in Eq. (2.12) leave the Higgs coupling to fermions unchanged. They do, however, induce point-like $HVff$ interactions and therefore contribute to Higgs production in association with an electroweak boson, see also the discussion in Sec. 5.5.

25 of the 59 dimension-six operators describe four-fermion contact interactions. Here, we only consider one of them, as it induces a shift in the Fermi constant and is therefore relevant for the description of electroweak precision data

$$\mathcal{O}_{LLLL} = (\bar{L}_1\gamma_\mu L_2)\,(\bar{L}_2\gamma^\mu L_1)\,. \tag{2.13}$$

The equations of motion [60] for the Higgs field and the electroweak gauge fields provide equivalence relations between (the sums of) dimension-six operators that allow us to eliminate three operators from the set that we have defined so far [68, 69]

	$Hf\bar{f}$	Zqq	Wqq'	$HZqq$	$HWqq'$	$Zl\bar{l}$	$Wl\nu$
$\mathcal{O}_{\phi 1}$	×	×	×			×	×
$\mathcal{O}_{BW}$		×	×			×	×
$\mathcal{O}_{\phi Q}^{(3)}$		×	×	×	×		
$\mathcal{O}_{\phi Q}^{(1)}$		×		×			
$\mathcal{O}_{\phi u}^{(1)}$		×		×			
$\mathcal{O}_{\phi d}^{(1)}$		×		×			
$\mathcal{O}_{\phi e}^{(1)}$						×	

Table 2.4: List of dimension-six operators affecting electroweak precision observables and their effect on fermionic couplings testable at the LHC.

$$
\begin{aligned}
2\mathcal{O}_{\phi 2} + 2\mathcal{O}_{\phi 4} &= \left(y^e_{33}(\mathcal{O}_{e\phi,33})^\dagger + y^u_{33}\mathcal{O}_{u\phi,33} + y^d_{33}(\mathcal{O}_{d\phi,33})^\dagger + \text{h.c.}\right) - \frac{\partial V(h)}{\partial h} \\
2\mathcal{O}_B + \mathcal{O}_{BW} + \mathcal{O}_{WW} + g^2\left(\mathcal{O}_{\phi 4} - \frac{1}{2}\mathcal{O}_{\phi 2}\right) &= -\frac{g^2}{4}\sum_{\text{flavor}}\left(\mathcal{O}^{(3)}_{\phi L} + \mathcal{O}^{(3)}_{\phi Q}\right) \\
2\mathcal{O}_B + \mathcal{O}_{BW} + \mathcal{O}_{BB} + g'^2\left(\mathcal{O}_{\phi 1} - \frac{1}{2}\mathcal{O}_{\phi 2}\right) &= \\
&\quad - \frac{g'^2}{2}\left(-\frac{1}{2}\mathcal{O}^{(1)}_{\phi L} + \frac{1}{6}\mathcal{O}^{(1)}_{\phi Q} - \mathcal{O}^{(1)}_{\phi e} + \frac{2}{3}\mathcal{O}^{(1)}_{\phi u} - \frac{1}{3}\mathcal{O}^{(1)}_{\phi d}\right) . \qquad (2.14)
\end{aligned}
$$

We choose to eliminate the leptonic operators $\mathcal{O}^{(1)}_{\phi L}$ and $\mathcal{O}^{(3)}_{\phi L}$ and the bosonic operator $\mathcal{O}_{\phi 4}$ to avoid *blind directions* to electroweak precision data [90]. A blind direction is defined by two (or more) operators which contribute to all observables in the same linear combination, rendering it impossible to disentangle the effects of a single of those operators.

The last category of dimension-six operators that we want to discuss is that of *dipole operators*, fermionic Higgs-gauge operators with a tensor Lorentz structure. In the HISZ basis, there are eight such operators which we list explicitly in Eq. (A.3). We will not consider dipole operators in our analysis, since they are strongly constrained by partial–wave unitarity violation, the top sector or measurements of the electric and magnetic dipole moments [93–95, 104]. Due to their non-SM Lorentz structure, the tree-level interference of dipole operators with the SM is helicity suppressed, as we will discuss explicitly for the operator

$$\mathcal{O}_{tG} = (\bar{Q}\sigma^{\mu\nu}T^a u_R)\,\tilde{\phi}\,G^a_{\mu\nu} \qquad (2.15)$$

in Section 5.3.

This completes the discussion of the set of dimension-six operators included in our studies. Altogether, we have identified 21 operators which are potentially relevant for our study of Higgs physics

$$
\begin{aligned}
&\{\mathcal{O}_G,\, \mathcal{O}_{WWW},\, \mathcal{O}_{\phi 1},\, \mathcal{O}_{\phi 2},\, \mathcal{O}_{\phi 3},\, \mathcal{O}_{GG},\, \mathcal{O}_{WW},\, \mathcal{O}_{BB},\, \mathcal{O}_{BW},\, \mathcal{O}_B,\, \mathcal{O}_W\} \quad \text{bosonic} \\
&\left\{\mathcal{O}_{u\phi,33},\, \mathcal{O}_{d\phi,33},\, \mathcal{O}_{e\phi,33},\, \mathcal{O}^{(3)}_{\phi Q},\, \mathcal{O}^{(1)}_{\phi u},\, \mathcal{O}^{(1)}_{\phi d},\, \mathcal{O}^{(1)}_{\phi e},\, \mathcal{O}^{(1)}_{\phi Q},\, \mathcal{O}_{tG},\, \mathcal{O}_{LLLL}\right\} \quad \text{fermionic,} \qquad (2.16)
\end{aligned}
$$

with the operator definitions given in Eqs. (2.9)–(2.12). We will later discuss in Section 5.3 how additional precision constraints from multi-jet production and the top sector on the operators $\mathcal{O}_G$ and $\mathcal{O}_{tG}$ respectively and the current reach for $\mathcal{O}_{\phi 3}$ at the LHC will render them irrelevant for current global studies of the Higgs sector at 13 TeV. The maximum number of operators included in our LHC Higgs fits is therefore 18 operators. In addition, we will include an invisible Higgs branching ratio as an additional free parameter.

2.4 Phenomenology of dimension-six operators

In this section, we want to examine the phenomenology of new interactions induced by dimension-six operators in more detail. Starting from a short summary of the vertices and field shifts of dimension-six operators, we will take the operator $\mathcal{O}_{\phi 2}$ as an example and study its effects explicitly.

A first, obvious result of dimension-six operators is the introduction of new vertices with higher-order contact interactions. We have already seen this effect in our analysis of Fermi's theory example in Section 2.2 in the form of a four-fermion vertex not present in the SM. Besides, dimension-six operators can also contribute to vertices already present at dimension-four: For two operators with dimension d and $d+2$ to contribute to the same vertex at tree-level, they need to have the same field content after

electroweak symmetry breaking. To achieve this, the higher-dimensional operator must either contain two additional powers of the Higgs doublet or two more derivatives compared to its lower-dimensional counter part. The vertices thus obtain additional contributions which can roughly be described as [77], respectively,

$$\frac{v^2}{\Lambda^2} \qquad \text{or} \qquad \frac{p^2}{\Lambda^2}\,. \tag{2.17}$$

The first type of operators with a v^2 proportionality will leave the Lorentz structure of the vertex unchanged and only contribute to the total rate without influencing the kinematics of the interaction. This is true, for instance, for the fermionic operators with Higgs couplings in Eq. (2.11). After EWSB the operator $\mathcal{O}_{u\phi,33}$ leads to a contribution of the form

$$\mathcal{O}_{u\phi,33} = \phi^\dagger\phi\;\bar{Q}_3\tilde{\phi}u_{R,3} \quad \rightarrow \quad v^2\;\bar{Q}_3\tilde{\phi}u_{R,3} \tag{2.18}$$

which has the exact same structure as the Yukawa terms in the SM Lagrangian in Eq. (2.1).

The second type of dimension-six operators, however, containing extra derivatives, will induce extra momentum dependences in a vertex. It will therefore change the kinematics of interactions and its effects will be more pronounced at high energies, as we will shortly see for the contribution of the operator $\mathcal{O}_{\phi 2}$ to the Higgs self-interaction.

Finally, as we already mentioned in Section 2.3, dimension-six operators can contribute to the two-point functions of the SM fields. In order to restore the canonical form of the kinetic terms, we therefore need to redefine our fields. This leads to global changes of the couplings of the physical fields or a change of their masses. Such changes are, for instance, induced by the operators $\mathcal{O}_{\phi 1}$, $\mathcal{O}_{\phi 2}$ and $\mathcal{O}_{BW}$.

The operator $\mathcal{O}_{\phi 2}$: As an example to show the effects of a dimension-six operator on two-point functions and kinematics, we will now study the phenomenology of the operator $\mathcal{O}_{\phi 2}$. It leads to a rescaling of all Higgs couplings and introduces new kinematic structures to the trilinear Higgs self-coupling. For convenience, we repeat the definition of the operator

$$\mathcal{L}_{\text{EFT}} = \mathcal{L}_{\text{SM}} + \frac{f_{\phi 2}}{\Lambda^2}\mathcal{O}_{\phi 2}\,, \qquad \mathcal{O}_{\phi 2} = \frac{1}{2}\partial^\mu(\phi^\dagger\phi)\partial_\mu(\phi^\dagger\phi)\,. \tag{2.19}$$

In order to study the effects of $\mathcal{O}_{\phi 2}$ on the physical fields, we rewrite the products of the Higgs fields in unitary gauge by $\phi^\dagger\phi = (v^2 + 2v\tilde{h} + \tilde{h}^2)/2$, where we use $\tilde{h}$ for the Higgs field, because it is not yet a mass eigenstate. Explicitly writing out the SM contributions to the kinetic Higgs term and the Higgs self-coupling as given in Eq. (2.1), we obtain the following form for Eq. (2.19)

$$\begin{aligned}\mathcal{L}_{\text{EFT}} &\subset \frac{1}{2}\,\partial^\mu\tilde{h}\,\partial_\mu\tilde{h} - \lambda\left(v\,\tilde{h}^3 + \tilde{h}^4\right) + \frac{f_{\phi 2}}{8\Lambda^2}\,\partial^\mu\left(v^2 + 2v\tilde{h} + \tilde{h}^2\right)\,\partial_\mu\left(v^2 + 2v\tilde{h} + \tilde{h}^2\right) \\ &= \frac{1}{2}\left(1 + \frac{v^2 f_{\phi 2}}{\Lambda^2}\right)\,\partial^\mu\tilde{h}\,\partial_\mu\tilde{h} - \lambda v\tilde{h}^3 + \frac{v f_{\phi 2}}{\Lambda^2}\,\tilde{h}\,\partial^\mu\tilde{h}\,\partial_\mu\tilde{h} - \lambda\tilde{h}^4 + \frac{f_{\phi 2}}{2\Lambda^2}\,\tilde{h}^2\,\partial^\mu\tilde{h}\,\partial_\mu\tilde{h}\,.\end{aligned} \tag{2.20}$$

The first term of the above Lagrangian rescales the kinetic term of the Higgs boson by a factor $(1+v^2 f_{\phi 2}/\Lambda^2)$ while the third and fifth term introduce new momentum-dependent trilinear and quartic Higgs self-couplings respectively. There are hence two important modifications of Higgs couplings due to the operator $\mathcal{O}_{\phi 2}$: First, a rescaling of the Higgs field $\tilde{h}$ is necessary to restore the canonical form of the kinetic term

$$h = \sqrt{1 + \frac{v^2 f_{\phi 2}}{\Lambda^2}}\;\tilde{h}, \tag{2.21}$$

which induces a universal shift of all couplings of the Higgs to other particles x

$$g_x = \frac{1}{\sqrt{1 + \frac{v^2 f_{\phi 2}}{\Lambda^2}}}\;g_x^{\text{SM}}\,. \tag{2.22}$$

Second, the operator contributes to the trilinear (and quartic) Higgs self-coupling with a new Lorentz structure

$$6v\lambda \quad \rightarrow \quad 6v\lambda + 2vf_{\phi 2}\left(p_1 \cdot p_2 + p_1 \cdot p_3 + p_2 \cdot p_3\right), \tag{2.23}$$

where p_x denote the momenta of the three involved Higgs bosons. This new Lorentz structure will become relevant in Section 6.4, where we study the Higgs self-coupling at a potential 27 TeV upgrade of the LHC.

2.5 Constraining SMEFT operators

Having fixed the set of operators for our analyses of the Higgs-gauge sector in the SMEFT framework, we now want to discuss the physical processes which will provide meaningful constraints on their Wilson coefficients. This includes rate measurements of different Higgs production and decay channels and of the di-boson sector at the LHC, as well as electroweak precision observables from LEP and the Tevatron.

Some of the operators in our set induce new Lorentz structures for vertices already present at dimension-four, as we have seen in the previous Section 2.4. They will therefore not only modify total rate measurements, but also influence differential distributions. Additional momentum-dependences of the dimension-six operators often render (momentum-related) kinematic distributions the most powerful source of constraints for the Wilson coefficients.

Higgs sector

All of the operators in Eqs. (2.9)–(2.11) influence the couplings of the Higgs boson to other SM particles. In addition, the fermionic Higgs-gauge operators in Eq. (2.12) affect quark-induced Higgs-production processes. We can therefore constrain their Wilson coefficients through measurements of the total rate of different Higgs-production processes and Higgs decays. As all of the Higgs production and decays channels can potentially be affected by more than one dimension-six operator, correlations between their Wilson coefficients arise.

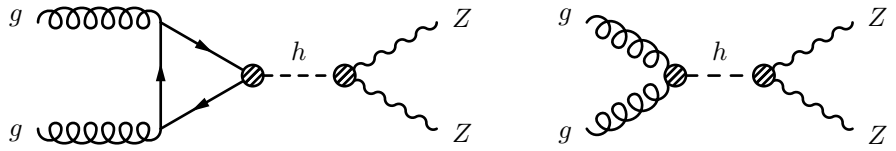

Figure 2.4: Feynman diagrams for the Higgs production and decay channel $pp \rightarrow h \rightarrow ZZ^*$. Blobs indicate the insertion of a dimension-six operator.

Let us consider for instance the channel $pp \rightarrow h \rightarrow ZZ^*$: On the production side, it is influenced by the operators $\mathcal{O}_{GG}$ and $\mathcal{O}_{u\phi,33}$, contributing to the hgg and $ht\bar{t}$ vertices respectively. The decay $h \rightarrow ZZ^*$ obtains modifications from all operators inducing hZZ vertices, i.e. from $\mathcal{O}_{BB}$, $\mathcal{O}_{WW}$, $\mathcal{O}_{B}$, $\mathcal{O}_{W}$, $\mathcal{O}_{BW}$, $\mathcal{O}_{\phi 1}$ and $\mathcal{O}_{\phi 2}$. In total, there are already nine operators influencing this one process, all of which contribute to other Higgs-production or -decay processes as well. This demonstrates the complexity of the correlations and motivates a global fit of all parameters and observables.

As a benchmark for current constraints on the Wilson coefficients of the considered dimension-six operators from the Higgs sector, we quote the typical reach of LHC Run I Higgs measurements

$$\frac{\Lambda}{\sqrt{|f|}} \gtrsim 250 \text{ ... } 500 \text{ GeV} \qquad \text{(pure Higgs analysis for LHC Run I [64])}. \tag{2.24}$$

Triple gauge vertices

Triple-gauge vertices (TGV) are probed at the LHC (and LEP) by studying di-boson production, specifically W^+W^- and WZ production, testing the structure of the WWZ or $WW\gamma$ vertices in kinematic distributions. Example Feynman diagrams for di-boson production are given in Fig. 2.5. Some of the dimension-six operators in Eq. (2.9) contain VVV couplings and directly contribute

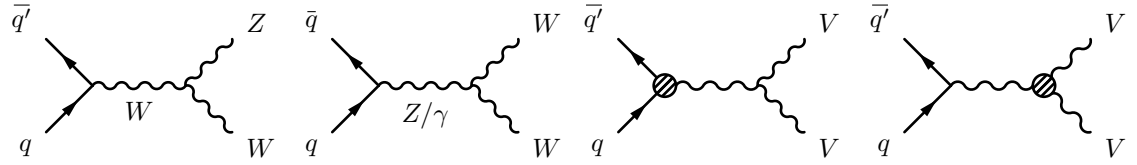

Figure 2.5: Feynman diagrams for di-boson production at the LHC. From left to right: SM production of WZ and W^+W^-; contributions from dimension-six operators influencing $f\bar{f}V$ and VVV couplings.

to TGVs, inducing new Lorentz structures of the self-interactions of the electroweak gauge bosons. We can therefore use di-boson production to constrain the Wilson coefficients of some of the bosonic operators in our basis, see Tab. 2.3. In addition to the modification of the self-interaction of electroweak gauge bosons by purely bosonic dimension-six operators, di-boson production is also influenced by dimension-six operators with $qq'V$ or $qq'VV$ couplings on the production side at the LHC. The full set of dimension-six operators influencing di-boson production at the LHC is therefore given by

$$\begin{aligned}\mathcal{L}_{\text{EFT}} \supset & \frac{f_W}{\Lambda^2}\mathcal{O}_W + \frac{f_B}{\Lambda^2}\mathcal{O}_B + \frac{f_{BW}}{\Lambda^2}\mathcal{O}_{BW} + \frac{f_{\phi 1}}{\Lambda^2}\mathcal{O}_{\phi 1} + \frac{f_{WWW}}{\Lambda^2}\mathcal{O}_{WWW} \\ & + \frac{f_{\phi Q}^{(1)}}{\Lambda^2}\mathcal{O}_{\phi Q}^{(1)} + \frac{f_{\phi d}^{(1)}}{\Lambda^2}\mathcal{O}_{\phi d}^{(1)} + \frac{f_{\phi u}^{(1)}}{\Lambda^2}\mathcal{O}_{\phi u}^{(1)} + \frac{f_{\phi Q}^{(3)}}{\Lambda^2}\mathcal{O}_{\phi Q}^{(3)} \,. \end{aligned} \tag{2.25}$$

In the remaining part of this section, we want to focus on modifications of the gauge-boson self-interactions by bosonic dimension-six operators, i.e. those in the first line of the above Lagrangian, and the new Lorentz structures induced by them.

The deviations from the SM gauge couplings and the new coupling structures are historically written in terms of the parameters $\kappa_\gamma, \kappa_Z, g_1^Z, g_1^\gamma$, λ_γ, and λ_Z [105]. Fixing $g_1^\gamma = 1$ by using electromagnetic gauge invariance, the shifts are defined by

$$\begin{aligned}\Delta\mathcal{L}_{\text{TGV}} = & -ie\,(\kappa_\gamma - 1)\,W_\mu^+ W_\nu^- \gamma^{\mu\nu} - \frac{ie\lambda_\gamma}{m_W^2}\,W_{\mu\nu}^+ W^{-\nu\rho}\gamma_\rho^\mu - \frac{ig_Z\lambda_Z}{m_W^2}\,W_{\mu\nu}^+ W^{-\nu\rho} Z_\rho^{\,\mu} \\ & - ig_Z\,(\kappa_Z - 1)\,W_\mu^+ W_\nu^- Z^{\mu\nu} - ig_Z\,(g_1^Z - 1)\,\left(W_{\mu\nu}^+ W^{-\mu} Z^\nu - W_\mu^+ Z_\nu W^{-\mu\nu}\right) \,, \end{aligned} \tag{2.26}$$

where $e = g s_w$ and $g_Z = g c_w$. We can translate from one notational convention to the other using the relations

$$\begin{aligned}\kappa_\gamma &= 1 + \frac{g^2 v^2}{8\Lambda^2}\,(f_W + f_B - 2f_{BW}) \\ \kappa_Z &= 1 + \frac{g^2 v^2}{8c_w^2\Lambda^2}\left(c_w^2 f_W - s_w^2 f_B + \frac{4c_W^2 s_W^2}{c_W^2 - s_W^2} f_{BW}\right) - \frac{1}{4(c_W^2 - s_W^2)} f_{\phi 1}\frac{v^2}{\Lambda^2} \\ g_1^Z &= 1 + \frac{g^2 v^2}{8c_w^2\Lambda^2}\left(f_W + 2\frac{s_W^2}{c_W^2 - s_W^2} f_{BW}\right) - \frac{1}{4(c_W^2 - s_W^2)} f_{\phi 1}\frac{v^2}{\Lambda^2} \\ \lambda_\gamma &= \lambda_Z = \frac{3g^2 m_W^2}{2\Lambda^2} f_{WWW} \,. \end{aligned} \tag{2.27}$$

The appearance of extra derivatives in the new Lorentz structures of the self-couplings of the electroweak gauge bosons leads to additional momentum-dependences of the vertices compared to the SM ones. The analysis of (momentum-related) differential distributions will hence be crucial to constrain dimension-six operators using measurements of di-boson production [64, 89].

For the more generic scenario of a non-linear or chiral effective Lagrangian [106–109], i.e. not assuming a doublet structure for the Higgs sector, the above parametrization would be extended and the correlations from gauge dependences are lost. Furthermore, the deviations generated by non-linear operators in the TGVs and the Higgs interactions could be completely de-correlated from one another. For the Higgs sector alone, however, there exists a trivial mapping of the linear and non-linear analyses, as shown in Refs. [63, 96].

To get a very rough idea of the constraints that di-boson production (in combination with measurements of the Higgs sector) can place on the Wilson coefficients f_B, f_W and f_{WWW}, we quote the typical reach of global Run I analyses,

$$\frac{\Lambda}{\sqrt{|f|}} \gtrsim 300 \text{ ... } 500 \text{ GeV} \qquad \text{(Higgs-gauge analysis for LHC Run I [64])}. \tag{2.28}$$

Measurements of TGVs were already performed at LEP. However, we note that already the LHC Run I di-boson measurements already clearly outperform the corresponding LEP measurements [64].

Electroweak precision data

The operators given in Eq. (2.12) affect the couplings of fermions to the weak gauge bosons, see Tab. 2.4. This is also true for some of the operators in Eq. (2.9), for which, however, the couplings to fermions only appear as a result of the redefinition of the fields to restore the canonical form of the kinetic terms. The full set of dimension-six operators influencing $f\bar{f}V$ or four-fermion couplings is given by

$$\begin{aligned}\mathcal{L}_{\text{EFT}} \supset & \frac{f_{\phi 1}}{\Lambda^2}\mathcal{O}_{\phi 1} + \frac{f_{BW}}{\Lambda^2}\mathcal{O}_{BW} + \frac{f_{LLLL}}{\Lambda^2}\mathcal{O}_{LLLL} \\ & + \frac{f_{\phi Q}^{(1)}}{\Lambda^2}\mathcal{O}_{\phi Q}^{(1)} + \frac{f_{\phi d}^{(1)}}{\Lambda^2}\mathcal{O}_{\phi d}^{(1)} + \frac{f_{\phi u}^{(1)}}{\Lambda^2}\mathcal{O}_{\phi u}^{(1)} + \frac{f_{\phi e}^{(1)}}{\Lambda^2}\mathcal{O}_{\phi e}^{(1)} + \frac{f_{\phi Q}^{(3)}}{\Lambda^2}\mathcal{O}_{\phi Q}^{(3)} \,.\end{aligned} \tag{2.29}$$

The couplings of the electroweak gauge bosons to fermions are well measured at LEP, the Tevatron and at the LHC, forming the set of so-called electroweak precision data on Z-pole and W-observables. At LEP, they were measured in the processes

$$e^+e^- \to Z/\gamma \to f\bar{f} \quad \text{and} \quad e^+e^- \to W^+W^- \to 4f \,. \tag{2.30}$$

We depict the Feynman diagrams relevant for the Z-pole observables in the SM and the contributions from dimension-six operators in Fig. 2.6. They probe the couplings of the Z boson to fermions as well as the two-point functions of the Z boson and the photon. For the properties of the W boson, the precision of LHC measurements is already at or beyond the level of the LEP and Tevatron measurements. In the following, we will just briefly list the set of electroweak precision observables and discuss their potential for constraining the operators in our basis.

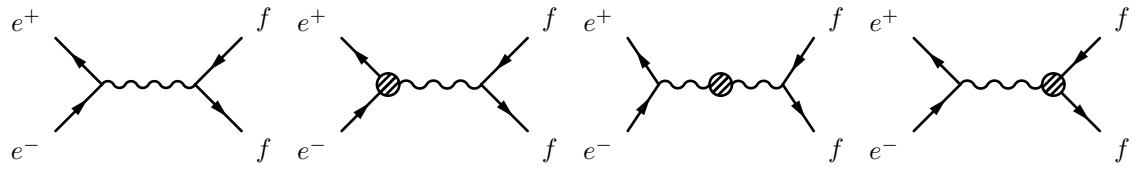

Figure 2.6: Feynman diagrams relevant for electroweak precision Z-pole observables in the SM (left) and contributions from dimension-six operators.

We include the Z-pole observables

$$\Big\{\Gamma_Z,\, \sigma_h^0,\, \mathcal{A}_l(\tau^{\text{pol}}),\, R_l^0,\, \mathcal{A}_l(\text{SLD}),\, A_{\text{FB}}^{0,l},\, R_c^0,\, R_b^0,\, \mathcal{A}_c,\, \mathcal{A}_b,\, A_{\text{FB}}^{0,c},\, A_{\text{FB}}^{0,b}(\text{SLD/LEP-I})\Big\} \,. \tag{2.31}$$

with measurements and correlations taken from Ref [110]. See Tab. 2.5 for explanations. Furthermore, we also include the W-observables

$$\left\{ m_W,\, \Gamma_W,\, \mathrm{BR}(W \to l\nu) \right\}, \tag{2.32}$$

with values taken from Ref. [111].

Due to their high precision, these observables provide strong constraints on dimension-six operators. For the inclusion of electroweak precision data in our global fit performed in Chapter 5, we follow the approach described in Ref. [104]. We use the SM predictions for above observables given in Ref. [112]. For the SM prediction of the W-mass this includes the full one- and two-loop EW and two-loop QCD corrections of $\mathcal{O}(\alpha\alpha_s)$ as well as some 3-loop contributions. The parametrization of the effects of our dimension-6 operators can be found in Ref. [104], where we limit ourselves to linear contributions from the higher-dimensional operators considered in our fit, i.e. we only take into account contributions up to $1/\Lambda^2$. As the typical energy scale of electroweak precision data is around m_Z, this approximation is justified as long as the dimension-6 corrections are small, i.e. $f m_Z^2/\Lambda^2 \ll 1$.

As a reference for the approximate size of the constraints on the Wilson coefficients of the dimension-six operators due to electroweak precision data, we quote individual limits of the standard analyses of the kind

$$\frac{\Lambda}{\sqrt{|f|}} \gtrsim 4 \text{ ... } 10 \text{ TeV} \qquad \text{(electroweak precision data [112])}. \tag{2.33}$$

Comparing these limits with the expected sensitivity of the global LHC analysis from Eq. (2.28), we find that the reach is significantly larger in the fermionic Higgs-gauge sector. Therefore, naively it might seem unnecessary to combine the set of operators of the Higgs-gauge sector with operators constrained by electroweak precision data in a global fit. However, we will see in Section 5.5 that the fermionic Higgs-gauge operators nevertheless lead to non-negligible effects at the LHC.

observable	definition	explanation
Γ_Z		Z boson total decay width
σ_h^0		Z boson production cross section
R_l^0	$\sigma_{\mathrm{had}}/\sigma_{ll}$	ratio of partial decay width w.r.t. hadronic decays
R_q^0	$\sigma_{q\bar{q}}/\sigma_{\mathrm{had}}$	
A_{FB}	$(N_F - N_B)/(N_F + N_B)$	forward-backward asymmetries
$\mathcal{A}_f$	$2\,(g_{Vf}/g_{Af})/[1 + g_{Vf}/g_{Af}]$	asymmetries of left- and right-handed couplings

Table 2.5: Explanation of the Z-pole observables given in Eq. (2.31).

2.6 The $\triangle$-framework

An arguably even simpler description of deviations from the SM in Higgs physics than effective field theory is given by the κ-framework [55,113,114], or the closely related Δ-framework [54] which describes new physics effects by their influence on SM Higgs couplings. The framework relates the measured couplings of the Higgs boson to a particle x, g_x, to their SM values g_x^{SM} via

$$g_x = \kappa_x\, g_x^{\mathrm{SM}} = (1 + \Delta_x)\, g_x^{\mathrm{SM}}\,. \tag{2.34}$$

We recover the SM values for $\kappa_x = 1$ or, equivalently, $\Delta = 0$.

The simplicity of the κ/Δ-framework comes with drawbacks. As this approach is not based on any symmetries, there is no general convention for whether or not to include terms with non-SM-like Lorentz structures in the Lagrangian. As a result, Lagrangians in the Δ-framework might break gauge invariance, depending on the terms included. Furthermore, if we stick to SM-like coupling structures

exclusively, we can only describe modifications of total rates, while we cannot model the effects of new physics on the kinematics as we will see, for instance, in Section 6.2. Finally, since the Δ-framework describes modifications of Higgs couplings only, it cannot be used to combine Higgs measurements with other precision measurements.

3 | Global Fits

In the last Chapter 2, we have introduced effective field theory as a phenomenologically powerful framework to describe new physics effects in a global and (almost) model-independent way. The next challenge that we need to tackle is to find the values of the Wilson coefficients of the dimension-six operators in our basis that fit the experimental observations in the best way. More generally, we are facing the following problem: On the one hand we have a model which provides predictions for physical observables in terms of a set of free parameters. On the other hand we have a set of experimental data. Finding the configuration of model parameters that describes the data in an optimal way may seem like a straight forward task. However, it is complicated by the fact that no measurement is perfect. Any data set will suffer from uncertainties, the shape of which depend on their sources. Statistical, systematic and theoretical uncertainties lead to different probability distributions of the experimentally observed quantities or their predictions. Moreover, observables often depend on secondary measurements in control regions leading to correlations between the uncertainties of different measurements. Taking all of the above effects into account, finding the optimal parameter values of a theory prediction to describe a given data set is the aim of a global fit.

Fitting is a two-step process: First, we need to define a measure of the goodness of a parameter configuration, i.e. we need to define a quantity whose value defines the (relative) quality of a fit. Second, we need to maximize (or minimize) that quantity.

In the following, we will present the SFitter framework [62] for performing global fits, which is used for the global analyses of the Higgs-gauge sector in the rest of this thesis. We will first discuss some basics of statistics and introduce the likelihood as a measure of the quality of a fit in Section 3.1. In Section 3.2, we will discuss the most commonly used algorithms for scanning the model parameter space and finding the parameter configuration that maximizes the likelihood. Finally, in Section 3.3, we will introduce the toy Monte Carlo method as an alternative concept to obtain best-fit points and confidence intervals in a global fit. We will closely follow the approaches of Refs. [111, 115–118].

3.1 A measure of goodness-of-fit

In order to find a model parameter configuration that suits experimental observables in the best way, we first need to define a measure of the quality of a fit. We will now see that the likelihood is the most powerful measure of goodness of fit and demonstrate how to construct and combine likelihood functions in practice. In the next Section 3.2, we will then discuss how to optimize this measure to examine the best-fit points of our model.

When we repeatedly perform the same experiment, we expect to see different outcomes each time as a result of imprecisions related to the measuring device or as a consequence of a more fundamental (e.g. quantum mechanical) stochastic nature of the system. Our expectation of the distribution of those different outcomes is encoded in a *probability density function* f. Integrating it, we can determine the probability P for the measured value of x to be within the interval $[x_{\min}, x_{\max}]$

$$\int_{x_{\min}}^{x_{\max}} f(x)\,\mathrm{d}x = P\,. \tag{3.1}$$

The probability density function (pdf) reflects our expectation of the distribution of the observable x in terms of model parameters α that we have suppressed in the above equation. In general, we should write the pdf as $f(x|\alpha)$, i.e. the probability density of x given α. To clearly separate between measured quantities and the parameters of our description, we will use Latin letters for measurements and Greek letters for model parameters in the following. Our *model* is defined as the totality of the predictions encoded by the parameters α and the assumption of the form of the pdf. The importance of the latter should not be underestimated: A global fit does not only depend on the theoretical modelling of observables, but is also influenced by our premise on the distribution of the data. We refer to a specific representation of a model for fixed parameters α as a *hypothesis* H. For the case of an effective field theory description, the parameters α correspond to the Wilson coefficients f_i of the considered dimension-six operators. The complete model is given by the effective description of the expectation values of the experimental observables as well as the assumptions that we make for the form of the pdfs. Typical choices for the form of the pdf are a Poissonian, Gaussian or flat shape:

1. **Poisson (statistical uncertainties)**
   The Poisson distribution describes the *statistical* uncertainty intrinsic to each measurement, i.e. the probability to observe d events when expecting ν_d events. It is the limit of the multinomial distribution for a small probability p, a large number of tries N and a finite number of expected events $\nu_d = N\,p$. The probability density function for the Poisson distribution is given by

   $$f_{\text{Pois}}(d|\nu_d) = \frac{(\nu_d)^d}{d!}\, e^{-\nu_d}\ . \tag{3.2}$$

   Its variance is $\sigma_d^2 = \nu_d$. As the significance of LHC measurements is typically given in terms of the number of signal s and background b events as $s/\sqrt{b}$, the statistical significance increases with the luminosity $\mathcal{L}$ as $\sqrt{\mathcal{L}}$.

2. **Gauss (systematic uncertainties)**
   In the limit of large event numbers d and ν_d, the Poisson distribution in Eq. (3.2) turns into a Gaussian distribution

   $$f_{\text{Gauss}}(d|\nu_d) = \frac{1}{\sqrt{2\pi}\sigma_d} \exp\left(-\frac{(d-\nu_d)^2}{2\sigma_d^2}\right)\ . \tag{3.3}$$

   In addition to statistical uncertainties, LHC observables are also subject to uncertainties arising from external inputs, related to the apparatus used or assumptions made by the experimenter. Those *systematic* uncertainties include uncertainties on the luminosity, on photon reconstruction efficiency or the jet energy scale. Since these uncertainties are usually extracted from large data sets, we will expect them to follow a Gaussian distribution. In principle, however, systematic uncertainties could follow any distribution and the assumption of a Gaussian distribution is only an approximation.

3. **Flat (theoretical uncertainties)**
   Flat uncertainty distributions are used for situations in which any outcome of a measurement within a specific range σ_d around a central value ν_d is equally probable and we do not expect the probability distribution to have any tails, $d \in [\nu_d - \sigma_d,\, \nu_d + \sigma_d]$. While this typically does not apply to experimental uncertainties, it can be relevant for *theoretical* uncertainties on the signal prediction, e.g. scale uncertainties. Scale uncertainties are usually estimated by varying the central scale μ by a factor 2. The spread between the predicted number of signal events obtained using the scales $\mu/2$ and 2μ defines the width $2\sigma_d$ which in this framework has no statistical interpretation. Within the range spanned by the two scale variations $[\nu_d^{\min},\, \nu_d^{\max}]$ we do no have a reason to favor any of the theoretical predictions and we make the conservative approximation that they are all equally probable. Beyond the boundaries set by $\mu/2$ and 2μ, we do not expect our theoretical prediction to be valid at all. Hence, we do not want any tails for the probability distribution. This behavior is represented in the probability density function for flat uncertainties by a box shape

   $$f_{\text{Flat}}(\nu_d|\nu_d^{\min},\, \nu_d^{\max}) = \frac{1}{2\sigma_d}\Theta\left(\nu_d - \nu_d^{\min}\right)\,\Theta\left(\nu_d^{\max} - \nu_d\right)\ , \qquad \sigma_d = \left(\nu_d^{\max} - \nu_d^{\min}\right), \tag{3.4}$$

using the Heaviside function Θ. Notice that Eq. (3.4) describes the probability density function for the prediction ν_d and not for the measurement d. Nevertheless, in SFitter, we often apply theory uncertainties to the measured signal instead of the theory prediction. This is an approximation made for convenience only.

The interpretation of the probability density functions $f(x|\alpha)$ as a function of α with fixed x is called the *likelihood* $L(\alpha) = L(x|\alpha) = f(x|\alpha)$. It is important to notice that the likelihood cannot be interpreted as a probability in terms of α. Specifically, it is not normalized and it does not correspond to the probability of a model parameter configuration given the data. For practical reasons, instead of handling the likelihood directly, it is common to work with the negative log-likelihood $-2\log L(\alpha)$. This has the advantage that a product of likelihood functions becomes a simple sum of log-likelihood functions and normalization factors become additive constants.

3.1.1 Likelihood ratios and statistical tests

Our aim for this section was to find a measure that quantifies the level of agreement between the data and a hypothesis. Let us now come back to this problem in a realistic environment: In practice, instead of a single observable we are usually confronted with a set of measurements $\mathcal{D} = \{x_1, ..., x_n\}$ that we will refer to as the *data*. Our theoretical description of the data is characterized by the parameters $\alpha = \{\alpha_1, ..., \alpha_k\}$ which we want to fit, i.e. for which we want to find the optimal configuration. A measure of the goodness of fit should map the data to a single real number. Such a function is called a *test statistic* $T(\mathcal{D}) \to \mathbb{R}$. The likelihood function is one example of a test statistic. It has been shown by Neyman and Pearson that for a hypothesis test of H_1 against the zero hypothesis H_0 the test statistic leading to the most powerful test is the likelihood ratio [119, 120]

$$T_{\text{NP}} = \frac{L(\mathcal{D}|H_1)}{L(\mathcal{D}|H_0)}\,. \tag{3.5}$$

In a way, our problem of trying to obtain an optimal parameter configuration for describing a given data set is closely related to the problem of hypothesis testing. However, instead of comparing two hypotheses explicitly, we want to quantify the level of agreement between the data and a hypothesis without an explicit reference to an alternative. There exists no equivalent of the Neyman-Pearson lemma in Eq. (3.5) for models with several free parameters. We can, nevertheless, generalize its idea and construct the profile likelihood ratio. Before we discuss this test statistic, we should first introduce the concept of nuisance parameters.

In many applications, the set of model parameters α consists not only of the parameters of interest, i.e. the parameters that we ultimately want to fit, but also additional parameters which are relevant for an accurate description of the model without being of intrinsic interest. We will refer to those parameters as *nuisance parameters*, $\alpha = \{\alpha_{\text{poi}}, \alpha_{\text{nui}}\}$. Let us explain this concept using an explicit example relevant for LHC physics: For LHC measurements, the quantities that we measure, i.e. our data d, will always contain a combination of the signal s that we are interested in and an indistinguishable background b, $d = s+b$. The predicted number of background events ν_b will hence enter our extraction of the signal as a nuisance parameter. One way of dealing with these additional parameter in our likelihood function, is to maximize the likelihood with respect to the nuisance parameters $\sup_{\alpha_{\text{nui}}} L(\alpha)$. This process is called *profiling* and we will write the corresponding profile likelihood as $L_p(\alpha) = L(\alpha, \hat{\hat{\alpha}}_{\text{nui}})$, where the double-hat notation denotes the profiled values of the nuisance parameters.

As a test statistic which is particularly useful for limit setting, we can now introduce the profile likelihood ratio [120]

$$T_p(\alpha) = \frac{L(\alpha, \hat{\hat{\alpha}}_{\text{nui}})}{L(\alpha_{\text{best}})} = \frac{L_p(\alpha)}{L(\alpha_{\text{best}})}\,, \tag{3.6}$$

i.e. the ratio of the profile likelihood and the likelihood at the best-fit point. Comparing the definition of the profile likelihood ratio to the ratio used in the Neyman-Pearson lemma in Eq. (3.5), we find that the parameter configuration maximizing the likelihood plays the role of the zero hypothesis.

The advantage of the profile likelihood ratio is that for large data sample sizes, the distribution of $-2\log T_p(\alpha)$ follows a χ^2 distribution with the number of degrees of freedom being given by the number of parameters α [121, 122]. Using the profile likelihood as a test statistic therefore allows us to make use of the known properties of the χ^2 distribution for limit setting. For the application of fitting in the SMEFT framework, for instance, we can set limits on a Wilson coefficient f_x by treating all other coefficients as nuisance parameters and profiling over them. We can then treat $-2\log T_p(f_x)$ with a single free Wilson coefficient f_x as a χ^2 distribution with one degree of freedom and obtain the 2σ limits by evaluating $\Delta\chi^2 = 4$, see e.g. Ref. [116, 118].

In order to motivate the concept of profiling, let us introduce the p-value, a common measure of the statistical significance of the data and a hypothesis $H(\alpha)$ [116, 118]

$$p = \int_{T_{\text{obs}}}^{\infty} L(T|H)\, \mathrm{d}T = \int_{T_{\text{obs}}}^{\infty} f(T|\alpha)\, \mathrm{d}T = P(T \geq T_{\text{obs}}|\alpha)\,. \tag{3.7}$$

It is defined as the probability of finding the test statistic T in the region of equal or greater incompatibility with the hypothesis than the level of compatibility observed with the actual data, characterized by T_{obs}, assuming that a large value of the test statistics corresponds to poor agreement of data and hypothesis (as is the case for the log-likelihood). A small p-value signals a small probability of finding a test statistic as large as or greater than the observed value T_{obs}. It is used to exclude null hypotheses. Let us now study the influence of nuisance parameters on the p-value. In order to be conservative, i.e. in order not to exclude a null hypothesis based on its small p-value, we should maximize the p-value of the hypothesis that we are testing with respect to variations of the nuisance parameters. This corresponds to maximizing the integrand in Eq. (3.7), the likelihood. Profiling over the nuisance parameters is hence the most conservative approach we can take when working with p-values.

In particle physics, it is common to translate the p-value in Eq. (3.7) into an equivalent significance Z defined such that a Gaussian-distributed variable observed at Z standard deviation above its mean has an upper-tail probability of p, i.e.

$$Z = \Phi^{-1}(1-p)\,, \tag{3.8}$$

where Φ denotes the inverse of the cumulative distribution of the standard Gaussian. A significance $Z = 5$ is typically used in particle physics to claim a discovery. This corresponds to a p-value of $p = 2.9 \times 10^{-7}$.

3.1.2 Combination of likelihood functions

We have found above that the likelihood is the most powerful measure of the goodness of a fit. In Eqs. (3.2), (3.3) and (3.4), we have discussed the likelihood functions for statistical, systematic or theoretical uncertainties respectively for a single measurement d and model parameters $\{\nu_d, \sigma_d\}$. In the real world, however, we usually have to construct a combined likelihood function for several measurements which are subject to various types of uncertainties. When f are the probability density functions of n independent and identically distributed measurements $\mathbf{x}$ in a data set $\mathcal{D}$, then the combined likelihood is given by

$$L(\alpha) = L(\mathcal{D}|\alpha) = \prod_{i=1}^{n} f(x_i|\alpha)\,. \tag{3.9}$$

In practice, the measurements whose likelihood we need to combine often depend on each other. As an example of dependent measurements, let us come back to the discussion of backgrounds as a nuisance parameter, see the paragraph below Eq. (3.5). Often, we do not have access to a signal measurement s directly, but we need to extract it from a measurement d that contains an indistinguishable background b, $s = d - b$. The number of background events b is often measured in a control region and enters our signal determination as a nuisance parameter. The combined likelihood is a convolution of

the measurements in the signal and control regions

$$L_{\text{Pois}}(\nu_s, \nu_b) = L_{\text{Pois}}(d|\nu_s, \nu_b) L_{\text{Pois}}(b_{\text{CR}}|\nu_{b,\text{CR}}) = \frac{(\nu_s + \nu_b)^d}{d!} e^{-(\nu_s+\nu_b)} \frac{(\tau\nu_b)^{b_{\text{CR}}}}{b_{\text{CR}}!} e^{-\tau\nu_b}, \tag{3.10}$$

where $\tau = \nu_{b,\text{CR}}/\nu_b$ is a scale factor. It has been inserted to account for the fact that the expected number of background events in the control region often differs from that in the signal region as one tries to reduce the statistical uncertainty by extracting the number of background events in a larger region. The estimated number of background events ν_b is a typical example of a nuisance parameter. It is irrelevant for our modelling of the signal which we ultimately want to constrain, but enters its extraction from a measurement. As discussed in the paragraph below Eq. (3.5), we deal with nuisance parameters by profiling over them, leading to the combined likelihood

$$L_{\text{Pois}}(\nu_s) = \max_{\nu_b^*} \frac{(\nu_s + \nu_b^*)^d}{d!} e^{-(\nu_s+\nu_b^*)} \frac{(\tau\nu_b^*)^{b_{\text{CR}}}}{b_{\text{CR}}!} e^{-\tau\nu_b^*}. \tag{3.11}$$

In general, we cannot perform the profiling analytically. While there exist analytical solutions for the combination of likelihood functions based on flat and Gaussian probability density functions, the likelihood combination for Poissonian distributions has to be performed numerically. In SFitter, we combine two Poisson likelihoods using the approximate formula [54]

$$\frac{1}{\log L_{\text{comb}}} \approx \frac{1}{\log L_{\text{Pois},1}} + \frac{1}{\log L_{\text{Pois},2}}, \tag{3.12}$$

which becomes exact in the Gaussian limit. In Appendix A.2, we explicitly list the formulae for the combination of Gaussian, Poissonian and flat uncertainties.

3.1.3 Correlations of measurements and uncertainties

The estimates of systematic uncertainties for individual experimental searches are typically based on the same secondary measurements. As an example, the same uncertainty on the luminosity will be used by every experimental analysis of an LHC experiment. In our definition of the (log-)likelihood, we need to take into account the correlation of these systematic uncertainties.

The correlation of two experimental channels i and j is a dimensionless measure of how much these two observables vary together. We can encode this linear relationship in the correlation matrix C

$$C_{ij} = \text{corr}(x_i, x_j) = \frac{V_{ij}}{\sigma_i \sigma_j} = \frac{E[(x_i - \bar{x}_i)(x_j - \bar{x}_j)]}{\sigma_i \sigma_j}, \tag{3.13}$$

where V denotes the covariance which is calculated from the expectation value E of the deviations of the measurements x from their mean value $\bar{x}$. We can directly see from Eq. (3.13) that the correlation matrix is symmetric by construction and has diagonal entries equal to 1. The off-diagonal entries of the correlation matrix are usually denoted *correlation coefficients* $\rho_{ij} = C_{ij}$. In practice, we often do not know these correlation coefficients explicitly, but need to estimate them for individual sources of uncertainties. As only systematic uncertainties will be correlated, we can replace the numerator in Eq. (3.13) by $V_{ij}^{\text{syst}} = \sigma_{i,\text{syst}}\, \sigma_{j,\text{syst}}\, \rho_{ij,\text{syst}}$ and use the full experimental uncertainty, i.e. the sum of systematic and statistical uncertainties, for the denominator

$$C_{ij} = \frac{\sum_{\text{syst}} \sigma_{i,\text{syst}}\, \sigma_{j,\text{syst}}\, \rho_{i,j,\text{syst}}}{\sigma_{i,\text{exp}} \sigma_{j,\text{exp}}}, \qquad \text{with } \sigma_{i,\text{exp}}^2 = \sum_{\text{syst}} \sigma_{i,\text{syst}}^2 + \sum_{\text{Pois}} \sigma_{i,\text{Pois}}^2. \tag{3.14}$$

In SFitter we usually assume a full correlation of systematic uncertainties of the same source, i.e. $\rho_{i,j,\text{syst}} = 0.99$ (we avoid $\rho_{i,j,\text{syst}} = 1$ for numerical reasons only). The full log-likelihood or, equivalently, the χ^2 including correlations is computed as

$$\chi^2 = \chi_i^T C_{ij}^{-1} \chi_j. \tag{3.15}$$

Error propagation is a simple explicit example for the effect of correlations. The uncertainty on a signal extracted from data and background measurements as $s = d - b$ is given by

$$\begin{aligned}\sigma_s^2 &= \left(\frac{\partial s}{\partial x_i}\frac{\partial s}{\partial x_j}\right)\Big|_{x=E[x]} V_{ij}, \qquad x = (d,\, b) \\ &= \left(\frac{\partial s}{\partial d}\sigma_d\right)^2 + \left(\frac{\partial s}{\partial b}\sigma_b\right)^2 + 2\rho\frac{\partial s}{\partial d}\frac{\partial s}{\partial b}\sigma_d\sigma_b \\ &= \begin{cases}\sigma_d^2 + \sigma_b^2 & \text{for } \rho = 0 \text{ (uncorrelated)} \\ (\sigma_d - \sigma_b)^2 & \text{for } \rho = 1 \text{ (fully correlated).}\end{cases}\end{aligned} \tag{3.16}$$

As events with the same experimental signature are usually subject to the same systematic uncertainties, independent of whether they belong to the signal or background component of our data, we assume full correlation between data and background $\rho = 1$.

Theory uncertainties are usually uncorrelated between different measurements in our approach. To introduce correlations of theory uncertainties we make use of nuisance parameters which we include as additional parameters in our fit, i.e. we include factors ξ in the signal prediction $s \to \xi\, s$ which we allow to vary within the range $\xi \in [1-\sigma_s/s,\, 1+\sigma_s/s]$. We profile over these nuisance parameters after our fit.

3.2 Fitting techniques

With the (log-)likelihood, we have defined a measure for comparing the quality of the agreement of a parameter configuration with a given data set. The challenge for fitting tools like SFitter is now to find best fit parameter configuration, i.e. to maximize the likelihood or to minimize the log-likelihood or χ^2. In the following, we will explain several techniques for likelihood maximization. Starting from a simple grid fit, we will discuss more complex fitting algorithms like Migrad which is using gradient descent and Markov chain Monte Carlos. In the next Section 3.3, we will present toy Monte Carlos as an alternative approach to obtain best-fit points and confidence limits.

All of the above mentioned fitting techniques come with advantages and drawbacks for specific applications. Best-fit points and limits in a multidimensional parameter space can be obtained with toy Monte Carlos in a computationally inexpensive way. For correlations and scans of complex likelihood functions with multiple minima, however, a Markov chain fit is potentially more suitable.

3.2.1 Grid

Arguably the most intuitive fitting technique for a model with n free parameters is to build an n-dimensional grid of the parameter space and find the point in the grid with the largest likelihood. Clearly, this is not only a very simple approach, but also a very inefficient one, since the density of points tested in a grid is completely unrelated to the likelihood. The computation time grows as x^n with x being the number of points tested per parameter which makes it intractable for a large number of fitting parameters.

3.2.2 Migrad

Migrad [123, 124] is a minimization algorithm based on gradient descent. Starting from a point α_k in parameter space, it chooses the next point α_{k+1} by moving along the gradient of the function $l(\alpha)$ that we want to minimize (in our case the log-likelihood) using a predefined step size s_k

$$\alpha_{k+1} = \alpha_k - s_k \nabla l(\alpha). \tag{3.17}$$

Following the gradient, the algorithm will lead eventually converge to a local minimum of the function $l(\alpha)$. The effective step size $\alpha_{k+1} - \alpha_k$ will become smaller and the evaluation of the log-likelihood more detailed close to the minimum as the gradient tends to zero in the vicinity of the minimum. In contrast to a grid fit, the test point density in a MIGRAD fit will therefore be larger close to the best fit point.

The method of steepest descent that we have discussed so far only specifies the direction of the next step, but not its length s_k. For correlated parameters this methods will converge very slowly. To overcome this issue, the Newton method uses the inverse of the Hessian matrix as the variable step size

$$\alpha_{k+1} = \alpha_k - H_l(\alpha)^{-1} \nabla l(\alpha) = \alpha_k - \left(\frac{\partial l(\alpha)}{\partial \alpha_i \partial \alpha_j} \right)^{-1} \nabla l(\alpha) \,. \tag{3.18}$$

The algorithm is effectively approximating $l(\alpha)$ as a quadratic function and the step suggested by it is the step to the minimum of this quadratic approximation. Larger step sizes will therefore be proposed further away from the minimum. While each step in the minimization is computationally very expensive in the Newton method as it includes calculating the matrix of second derivatives and the inversion of such a matrix, the convergence of the algorithm is very efficient. If $l(\alpha)$ is in fact a quadratic function, the algorithm converges in one step. MIGRAD is using a variant of this method.

3.2.3 Markov chains

A Markov chain is a sequence of points in parameter space for which the conditional probability distribution of choosing the next point α_{k+1} in parameter space depends only on the present point α_k and not on any previous part of the chain [125]. Markov chains are a well-established tool for the maximization of likelihoods with non-trivial functional dependencies, e.g. with multiple minima, or a large number of parameters [62, 126].

In practice, the probability distribution used as a criterion for the acceptance of new points is the likelihood. We randomly choose a point α_{test} in parameter space and compare its likelihood to the likelihood of the current point of the Markov chain. If the likelihood of the test point is larger than that of the current point, we directly accept it as the next element of the chain. Otherwise, we test if the likelihood of the point fulfills the condition

$$\frac{L(\alpha_{\text{test}})}{L(\alpha_k)} \geq r \,, \tag{3.19}$$

with r being a random number in the range $[0, 1]$ and accept the point if the condition is fulfilled [127, 128]. The algorithm will move towards the best fit point and explore the area close to it. In the ideal case Markov chains scale only linearly with the number of input parameters, allowing for fits of a multidimensional parameter space.

To increase the performance of the Markov chain, we have two handles: We can either make the generation of test points more efficient or we can modify the probability of accepting points as described by Eq. (3.19). Taking the first of the two approaches, we can choose our test points from a random distribution around the current element of the chain α instead of choosing αtest completely randomly. As the likelihood is usually a continuous function of the fit parameters, points close to an element with a (large) likelihood can be expected to have a similarly large likelihood. We can therefore choose test points from e.g. a Breit-Wigner or a Gaussian distribution around the current point.

Alternatively, we can also increase the efficiency of the Markov chain by modifying the acceptance criterion for new chain elements. A common approach coined *cooling* reduces the probability of a point with a smaller likelihood to be accepted as the next element of the chain depending on its position in the chain [54, 129]. For this, we divide the Markov chain into 100 segments labelled with $j = 1 \cdots 100$ and replace the right hand side of Eq. (3.19) by

$$\frac{L(\alpha_{\text{test}})}{L(\alpha_k)} \geq r^{\frac{100}{j \cdot c}} \,, \tag{3.20}$$

with a cooling factor $c \sim 10$. At an early stage of the Makov chain, i.e. for small values of j, when our aim is to perform a rough scan to make sure that we will find multiple minima, the right hand side is close to zero and almost all points are accepted. With increasing j the threshold for a test point to be accepted as the next element of the chain is raised. Therefore, the Markov chain will focus on finding better estimates of the best fit point during its later stages.

Markov chains are useful for broader scans of the parameter space and for finding multiple minima. If one is only interested in finding the best-fit point in parameter space, there are more efficient algorithms like MIGRAD which are better suited for such problems. The breadth of the scanned parameter space makes Markov chains particularly useful for examining correlations.

3.3 Toy Monte Carlos

So far, the algorithms discussed to find the best fit points of a fit were based on the minimization of the log-likelihood. Given a set of measurements, we were trying to find the point in parameter space that best describes the data. The *toy Monte Carlo method* is a different approach for obtaining best fit points and confidence limits. It is also know under the name of *Monte Carlo (replica) method* in the parton distribution function (PDF) fitting community [130–132]. The idea of the toy Monte Carlo method is to create large number($\mathcal{O}$(10k) for most of our fits) of artificial data sets, based on the experimental central values, uncertainties, and correlation associated with each measurement. For the generation of each pseudo measurement, we shift the data within their uncertainties, respecting the different nature of different sources of uncertainties (flat, Poissonian, Gaussian), and their correlations. The resulting set of artificial replicas can then be analyzed using textbook methods.

We create a replica of measurement i with experimental value x_i^{exp} using

$$\begin{aligned} x_i^{\text{toy}} &= x_i^{\text{exp}} + \Delta^{\text{shift}} + \text{sign}(\Delta^{\text{shift}})\Delta^{\text{flat}}\,, \\ \Delta^{\text{shift}} &= \Delta^{\text{Gaus}} + \Delta^{\text{Pois}} + \Delta^{\text{syst}}\,, \end{aligned} \tag{3.21}$$

where

$$\begin{aligned} \Delta^{\text{Gaus}} &= r^{\text{Gaus}} \sqrt{\sum_j (\sigma_j^{\text{Gaus}})^2} & \Delta^{\text{Pois}} &= \frac{r^{\text{Pois}}(\tau x_i^{\text{toy}})}{\tau} - x_i^{\text{toy}} \\ \Delta^{\text{syst}} &= \sum_{j=1}^{N_{\text{syst}}} r_j^{\text{syst}} \sigma_j^{\text{syst}} & \Delta^{\text{flat}} &= \sum_{j=1}^{N_{\text{flat}}} \sigma_j^{\text{flat}}\,. \end{aligned} \tag{3.22}$$

The parameters r^{Gaus}, $r_j^{\text{syst}} \in \text{Gauss}(0,\,1)$ are random numbers drawn from a normal distribution. $r^{\text{Pois}}(x)$ is a random integer drawn from a Poissonian distribution with mean x and τ denotes the factor between the size of the signal and control regions, see Eq. (3.10) and the discussion below.

For each of those smeared pseudo data sets we calculate the best-fit point using an appropriate fitter (e.g. Minuit [123, 124]). We then create one-dimensional histograms of these best-fit points in terms of the model parameters, implicitly profiling over the other model parameters. For large data sets, these histograms will follow a Gaussian distribution. We deduce the mean and confidence limits of the model parameters using textbook methods.

4 | Tagging Jets in Invisible Higgs Searches

Invisible Higgs decays are a generic signature of many interesting models of physics beyond the Standard Model. Improved limits on an invisible Higgs branching ratio hence provide important constraints on e.g. Higgs portal models in the context of dark matter [133] or electroweak baryogenesis [42]. As a contribution to the total Higgs width, an invisible Higgs branching ratio is also an important ingredient for global fits of Higgs couplings, see Chapter 5 and 6. In a global analysis, an invisible Higgs branching ratio is closely correlated with the effects of other significant contributions to the Higgs width such as modified bottom-Yukawa coupling or a renormalization of the Higgs wave function which results in a total rescaling of all Higgs couplings. In Chapter 6, we will explicitly make use of the analysis developed and discussed in this chapter to constrain an invisible Higgs branching ratio at a potential 27 TeV upgrade of the LHC in a global fit.

In this chapter, we will examine the most sensitive search channel for invisible Higgs decays, weak boson fusion. Making use of multivariate analysis techniques, we perform a dedicated study of the tagging jets and central jet activity. First, we will analyze the different background contributions to the WBF signal and show why a precise understanding of single-top production is crucial. We then study the dependence of the rate of the weak boson fusion process on the jet-radius parameter of the tagging jets. To disentangle the WBF signal from its QCD backgrounds, we will include subjet-level information on the tagging jets and additional jet activity in our analysis and demonstrate how these observables relieve some of the pressure on other, critical observables like a central jet veto. Finally, we will compare the sensitivity of WBF to an invisible Higgs branching ratio with associated Higgs production and discuss how an increase of trigger thresholds at the HL-LHC could influence the expected upper limits.

This chapter is based on work in collaboration with Fabian Keilbach, Rhea Moutafis, Tilman Plehn and Jennifer M. Thompson [1]. All tables and figures as well as a significant part of the text are taken from the corresponding publication.

4.1 Introduction

The lack of discoveries beyond the Higgs boson at the LHC [4–8] have forced both experimentalists and theorists to change the way we perform, analyze and describe searches for new physics. Quietly and against all odds, particle physicist have transformed the LHC from the discovery machine that it was intended to be into a precision experiment, turning hadron-collider physics into a field of experimental and theoretical precision. This paradigm shift has forced us to reexamine our understanding of QCD and jets. Rather than regarding jets as contained objects describing partons from hard processes only, we now try to make use of their sub-structure to fully exploit their potential as analysis objects. Advances in machine learning methods and multivariate analysis techniques, have further fueled the focus on jet sub-structure analyses. Searches for Higgs decays to invisible particles in hadronic final states feature interesting QCD structures and are subjet to large backgrounds. This makes them a prime candidate to test and profit from these new technical developments. Looking into the future,

there is a strong motivation to give up on jets as contained objects altogether and to use them as containers for sub-jet level observables and an optional link to jet-based observables instead.

In the Standard Model, Higgs decays to invisible particles only arise from the decay into Z bosons and a subsequent decay to neutrinos, $h \to ZZ^* \to 4\nu$, and are therefore extremely rare. Nevertheless, since numerous BSM scenarios predict an invisibly decaying Higgs [25, 26, 134–138], such a signature is among the most interesting of the LHC. For example, invisible Higgs decays may be related to dark matter (DM) in the context of Higgs portal models. Minimal models with direct couplings of the Higgs boson to DM [139–141] have mostly been excluded for $2m_{\text{DM}} < m_h$ [142,143]. However, the Higgs may provide a portal to more general hidden/dark sectors and thus decay into light dark matter particles or long-lived particles that escape detection [14–32]. We refer to Ref. [133] for a review on dark matter Higgs portal models. Such models might also allow for a strong first-order phase transition which makes them relevant in the context of baryogenesis [42]. An invisible Higgs branching ratio would emerge as a common signature of Higgs portal models, independent of their exact particle content.

Invisible Higgs decays can be searched for at the LHC in various experimental final states. Let us start our discussion of possible signatures with a recap of the cross section of different Higgs production processes at the LHC, as given in Tab. 2.1. The Higgs production mechanism with the largest cross section is gluon fusion. However, with the Higgs being the only final state particle of this process to leading order, gluon fusion is obviously not apt for invisible Higgs searches, because its only signature would be missing energy. In order to actually observe an event in the detector, we need the Higgs to recoil against a visible particle. In gluon-fusion Higgs production, this could for instance be a hard jet or a vector boson radiated from the top-quark loop. Nevertheless, the emission of an additional particle will reduce the cross section of these *mono-X* signatures through a factor α_s or α and a supplementary phase-space suppression, rendering this process subdominant to other search channels for invisible Higgs decays.

WBF is the Higgs production process with the second largest cross section at the LHC, its rate being an order of magnitude smaller than the rate of gluon fusion. Its signature, featuring large missing transverse energy and two jets, makes this process the most sensitive search channel for an invisible Higgs branching ratio [144–148]. The massive W-propagators in WBF generate a large transverse momentum of the Higgs boson, resulting in large missing transverse energy. Paired with the existence of two forward tagging jets [149–156], this experimental signature allows for an efficient triggering and suppression of the backgrounds. The largest backgrounds to WBF arise from QCD V+jets production. They can be handled through a systematic analysis of the tagging-jet kinematics and the central jet activity.

In addition to WBF, the LHC reach for an invisible Higgs branching ratio receives important contributions from boosted Higgs production in association with either a W or a Z boson [157–161]. For this production process, there are two promising experimental signatures to search for invisible Higgs decays. First, a leptonic Z-decay recoiling against missing energy ensures a good trigger efficiency and a powerful handle in reducing all QCD backgrounds. Second, we can study hadronic decays of the vector boson, leading formally to same V+2 jets final state as WBF, however in a very different phase-space region. Formally of the same perturbative order as the WBF production process, the production rate for both processes is, especially for the leptonic case, significantly smaller than the rate of WBF Higgs production. Finally, searches for invisible Higgs decays are also performed in $t\bar{t}h$ production [162–164]. This channel will, however, remain a challenge both statistically and systematically, even at the high-luminosity LHC. For the corresponding Feynman diagrams of all discussed processes and their cross section (not including decays of vector bosons), we refer to Fig. 2.1 and Tab. 2.1 respectively.

Experimental searches for invisible Higgs decays by CMS rely on WBF [165], Zh production [166], a combination of both production processes [167, 168] and $t\bar{t}h$ [169]. Similarly, in ATLAS there are searches in WBF [170, 171], Zh production [172–174], and a combination including the hadronic Zh channel [175, 176]. The most stringent constraints on the invisible Higgs branching ratio currently come from the combined Run I+II CMS WBF analysis [165] which sets a limit of 19%. At the end of the high-luminosity run, we expect constraints at the level of 2 ... 3% [148]. While the previously cited experimental limits on an invisible Higgs branching ratio usually rely on SM Higgs-production

rates, those assumptions can be avoided in a global fit of the Higgs-gauge sector [3, 63, 64]. We will find in Chapter 5 that a global fit of current LHC Run II data limits the invisible Higgs branching ratio to 38% at 95% CL. At future colliders, we expect the same signatures to constrain the invisible Higgs branching ratio to around 1% at a 27 TeV upgrade of the LHC in a global fit, as discussed in Chapter 6, and to the sub-percent level at a future 100 TeV hadron collider [177].

In this study we focus on the WBF production channel and examine possible enhancements on its sensitivity through an improved understanding of the tagging jets and the central-jet activity. We start our analysis by discussing the relevant backgrounds in Section 4.2. In particular, we focus on the difference between the irreducible Z+jets backgrounds and the W+jets backgrounds arising from a contamination by single-top production in the W+jets backgrounds. In Section 4.3, we analyze the dependence of the total WBF rate on the jet-radius parameter of the tagging jets. The main part of our study is dedicated to an analysis of the quark vs gluon content of the tagging jets in Section 4.4. We examine the potential of using jet-substructure variables aiming at quark/gluon discrimination to reduce QCD backgrounds. With future updates of the LHC trigger thresholds for the high-luminosity LHC in mind, we finally ask the crucial question by how much the sensitivity of the WBF signature gets degraded by stronger trigger requirements in Section 4.5. In particular, we check how the WBF sensitivity compares to the reach of a Zh benchmark analysis for different increases of the trigger thresholds.

4.2 Dominant backgrounds

Higgs production in WBF is the most sensitive channel to search for invisible decay modes of the Higgs boson at the LHC [144, 148]. As a result of the recoil against the tagging jets, the transverse momentum of the Higgs boson is automatically at the level of $p_{T,h} \gtrsim m_W/2$, leading to the signature of large missing transverse energy. Moreover, the absence of a color connection between the tagging jets reduces the central jet activity which allows us to control QCD backgrounds [149–154]. The expected sensitivity of the WBF channel to the invisible Higgs branching ratio is at the level of 2 ... 3% at the LHC for integrated luminosities of 3 ab^{-1}. A potential 27 TeV upgrade of the LHC will be able to constrain the invisible Higgs branching ratio to around 1% in a global fit, as we will later discuss in Chapter 6. At a 100 TeV hadron collider limits below the one percent level are accessible [177, 178]. As a reference, we also quote the current LHC Run II limit of 38% on an invisible Higgs branching ratio, based on a global fit allowing non-SM-like Higgs-production cross sections, see Chapter 5.

Limitation on the LHC reach in the WBF channel arise mainly from our understanding of the backgrounds and their central-detector QCD features. The main backgrounds come from V+jets production. The irreducible background from Z+jets production with a decay $Z \to \nu\bar{\nu}$ and the nominally reducible W+jets production with the lepton of the decay $W \to \ell\bar{\nu}$ remaining unobserved can both contribute at a similar level. We distinguish between the two hard jets of the backgrounds being produced through a hard QCD process, $\sigma(Vjj) \propto \alpha_s^2\alpha$ and through a hard electroweak process $\sigma(Vjj) \propto \alpha^3$, with $V = Z, W$. The separation of these two components will be useful for the discussion of their hadronic activity and parton content later on.

The Z-background can be measured in a control region through the visible decays $Z \to \ell\ell$. However, as the Z branching ratio to leptons is smaller than its invisible counterpart, this control background sample will contain less events than the signal region sample. The W+jets background with the leptonic decay $W \to \ell\bar{\nu}$ should behave very similar to the Z+jets background. Differences occur, however, as a result of the phase-space effects of the lost lepton and their interplay with the detector efficiency, preferring a forward or soft lepton.

We generate our event samples for the WBF signal and its background processes for a 14 TeV high-luminosity LHC at LO using Sherpa2.2.1 [179] with up to three or four hard jets combined in the Ckkw scheme [180]. For the matrix element, we employ Comix [181]. As already mentioned, we separate the QCD and electroweak sub-processes for both background contributions. For the WBF signal we also take into account the contribution from gluon fusion, denoted as the QCD signal

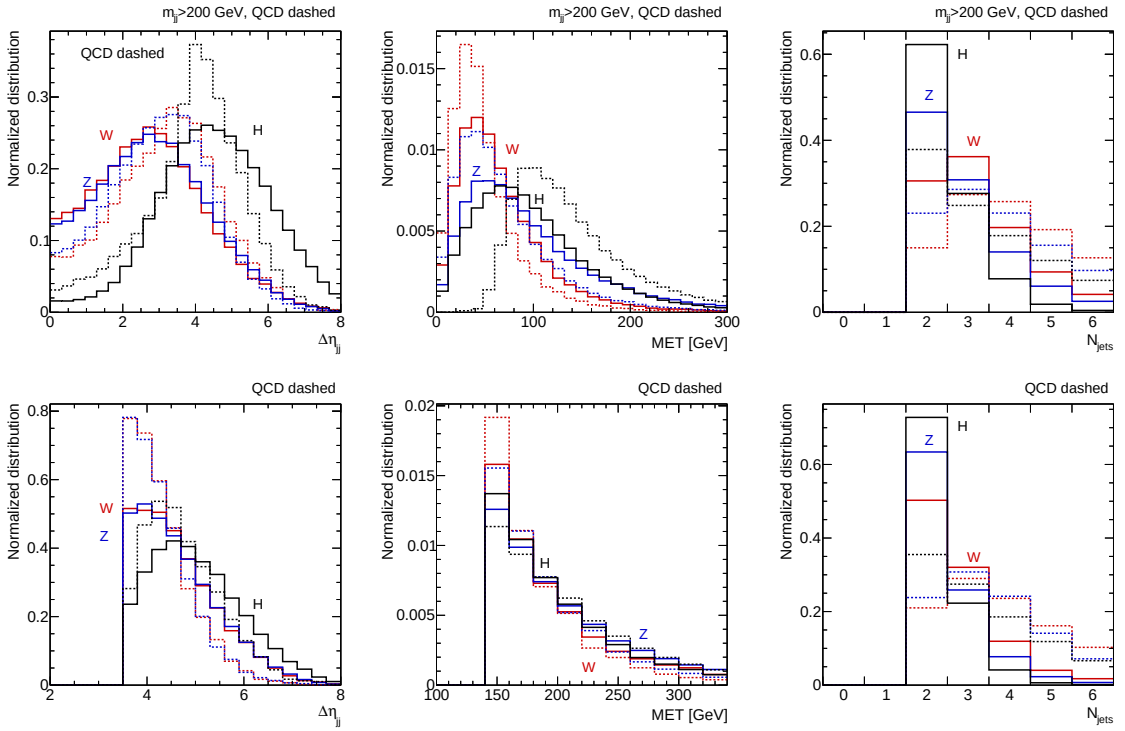

Figure 4.1: WBF signal and background distributions after the minimal requirement $m_{jj} > 200$ GeV (upper panels) and after the pre-selection cuts of Eq.(4.3). The $\Delta\eta_{jj}$ (left) distribution for the V+jets Z backgrounds look very similar. Deviations between W and Z backgrounds appear for the missing energy distribution (center) and N_{jets} (right). Figures taken from Ref. [1].

contribution [182]. We generate the corresponding event sample at LO with two hard jets using Sherpa with OpenLoops [183–189]. Jet are clustered with a radius parameter of $R = 0.4$ using the anti-k_T algorithm implemented in FastJet [190–192] and we define the two hardest jets in each event as the tagging jets. Detector effects are taken into account using the fast detector simulation Delphes3.3 [193] with the ATLAS card. We have updated the lepton efficiency in the detector card to match the numbers in Refs. [194, 195].

In the upper panels of Fig. 4.1 we show the distributions of the pseudo-rapidity separation $\Delta\eta_{jj}$, missing transverse energy $\not{E}_T$ and the number of jets N_{jets} for the W and Z backgrounds in comparison to the Higgs signal after the minimal requirement

$$m_{jj} > 200 \text{ GeV} . \tag{4.1}$$

This kinematic cut significantly reduces the contribution of the $Vh \to (jj)h$ topology to the signal process and selects the diagrams corresponding to the WBF signature that we are interested in. Comparing the $\Delta\eta_{jj}$ (and m_{jj}) distributions of the backgrounds, we find that for both the electroweak and the QCD sub-processes the distributions of the Z+jets and W+jets contributions behave very similarly. For the missing transverse energy distribution, we observe that the W+jets background is significantly softer than its Z+jets counterpart in the both QCD case and in the electroweak case. This is an artifact of detector effects: In order for the W+jets process to contribute to the $\not{E}_T$+jets signature of the WBF signal, the lepton of the decay of the W boson must remain unreconstructed. However, a lepton not leaving enough tracks in the detector to be reconstructed, is not equivalent to not depositing any energy in the detector at all. An undetected lepton will still deposit energy in the calorimeter and contribute to the towers and tracks visible in the detector which the missing transverse energy is reconstructed from. We have explicitly checked that this detector effect is indeed responsible for the observed difference in the $\not{E}_T$ distribution.

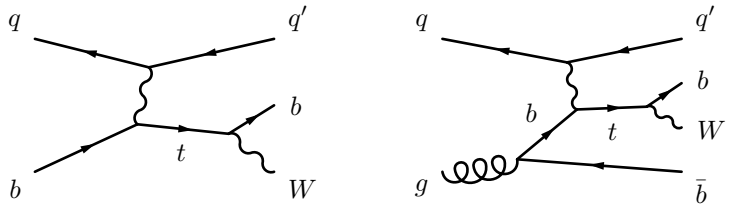

Figure 4.2: Example Feynman diagrams for the single-top contribution to the W+jets background.

In the right panel of Fig. 4.1, we display the number of jets with $p_{T,j} > 20$ GeV and $|\eta_j| < 4.5$ for the signal and background samples. Clearly, the number of events with more than two jets is significantly lower for the WBF signal than for its backgrounds. Surprisingly, however, we find a significantly different behavior for the electroweak Z+jets and W+jets backgrounds, as the W+jets background is likely to have a larger number of jets. The reason for this behavior is a contamination from the single-top process to this background category,

$$pp \to bW^+ + \text{jet(s)}. \tag{4.2}$$

We display the corresponding Feynman diagrams in Fig. 4.2. After the minimal requirement $m_{jj} > 200$ GeV, the single-top contribution to the W+jets background is 30% for two-jet events and up to 50% for three-jet events. Eventually, we should therefore understand this difficult process with high precision during the future LHC runs.

In order to mimic trigger effects and reject generic backgrounds, we will require a set of basic cuts before applying a dedicated signal vs background analysis. We will make use of the CMS pre-selection cuts in Ref. [168] which require two tagging jets with a large angular separation and sizeable missing transverse energy

$$\begin{aligned}
p_{T,j_{1,2}} &> 40\,\text{GeV} & |\eta_{j_{1,2}}| &< 4.5 & \not{E}_T &> 140\,\text{GeV} \\
\eta_{j_1}\,\eta_{j_2} &< 0 & |\Delta\eta_{jj}| &> 3.5 & m_{jj} &> 600\,\text{GeV} \\
p_{T,j_3} &> 20\,\text{GeV} & |\eta_{j_3}| &< 4.5 & &\text{(if 3rd jet available)}\,.
\end{aligned} \tag{4.3}$$

In addition, we will veto any lepton with a transverse momentum larger than $p_{T,\ell} > 7$ GeV. In the lower panels of Fig. 4.1 we show the normalized distributions of the WBF Higgs signal and its dominant backgrounds after the application of these pre-selection cuts. The QCD Z+jets and W+jets backgrounds now resemble each other much more closely. This is a result of the reduced single-top contamination in the W+jets sample which decreases to below 5% for two-jet events and below 12% for three-jet events.

4.3 Tagging-jet size

In the following two sections, we perform a systematic analysis of the tagging jets in the Higgs WBF signal and its backgrounds. We first focus on the influence of the jet-radius parameter on the rate on the WBF signal and background processes. While the jet size in ATLAS and CMS analyses is typically chosen following experimental considerations, it has been shown in the literature that the jet-radius parameter of the tagging jets in WBF Higgs production has a significant impact on the effect of higher-order corrections to the rate [196]. This is obviously an effect of real parton emission and the combination of these additional partons into the tagging jets. We will further analyze this behavior of the WBF cross section and compare it with the jet-radius parameter dependence of the associated Zh production rate with hadronic Z decays. This comparison will allow us to test whether the strong R-dependence of the WBF signal is a result of the specific process or merely an artifact of phase-space effects. Our simulations are based on the tool chain discussed in the previous Sec.4.2. We merge up to three hard jets, employ parton showering and again define the tagging jets as the hardest two jets with $p_{T,j} > 20$ GeV using the anti-k_T algorithm in FastJet, now varying the jet-radius parameter within the range $R = 0.4 \ldots 1.0$.

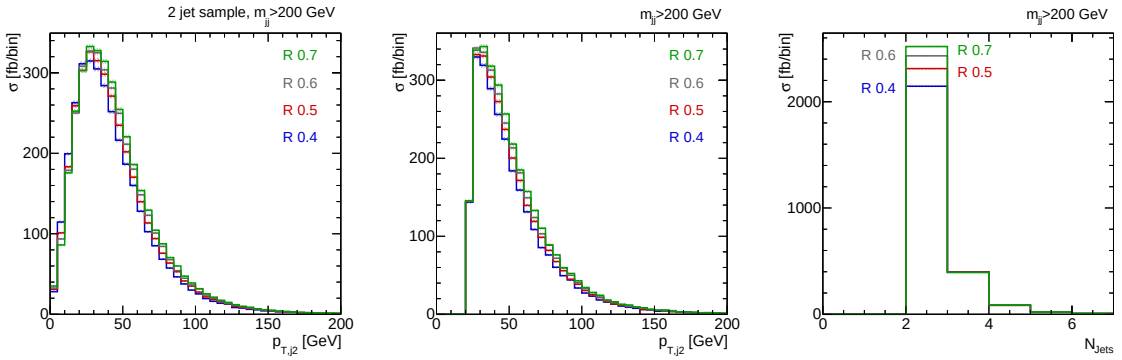

Figure 4.3: WBF signal distributions for the exclusive two-jet sample (left) and the full sample (center and right) requiring only $m_{jj} > 200$ GeV. Figures taken from Ref. [1].

In Fig. 4.3, we display the dependence of the WBF signal on the jet-radius parameter R for the signature

$$pp \to jj\, h_{\text{inv}}\,. \tag{4.4}$$

As this definition in principle includes the Vh topology with $V \to jj$, we again apply the minimal cut $m_{jj} > 200$ GeV as in Eq. (4.1) to select the WBF diagrams only in a two-jet plus parton shower setup with no $p_{T,j}$ cut. Comparing the transverse momentum distribution of the second tagging jet for different jets sizes in the left panel of Fig. 4.3, we find that the $p_{T,j}$ spectrum becomes harder with an increasing jet-radius parameter. Obviously, this increase is due to the tagging jet picking up additional jet radiation with a larger jet size. The induced shift of the peak of the $p_{T,j}$ distribution due to an increase of the jet-radius parameter from $R = 0.4$ to $R = 0.7$ is of the order of 5 GeV. The effect remains when we include a third merged hard jet in our sample, as displayed in the middle panel of Fig. 4.3. Notice that in addition to the increase of the transverse momentum of the tagging jets, we also find a growth of the total rate and an increment of the number of two-jet events with the jet-radius parameter. The additional collected hadronic activity in the wider jets helps passing the basic cut $m_{jj} > 200$ GeV. The fact that the number of three-jet and four-jet events remains constant is an accidental result of the trade-off between the growing rate and the merging of hard jets with an increasing jet-radius parameter.

Next, we display the total rate of the WBF signal and Z-background rates as a function of the jet-radius parameter R in the left panel of Fig. 4.4. We apply the pre-selection cuts of Eq. (4.3) to estimate the effects of the jet size in a realistic environment. We show different curves for samples with two or three hard jets merged. For the QCD Z+jets backgrounds we also display the R-dependence

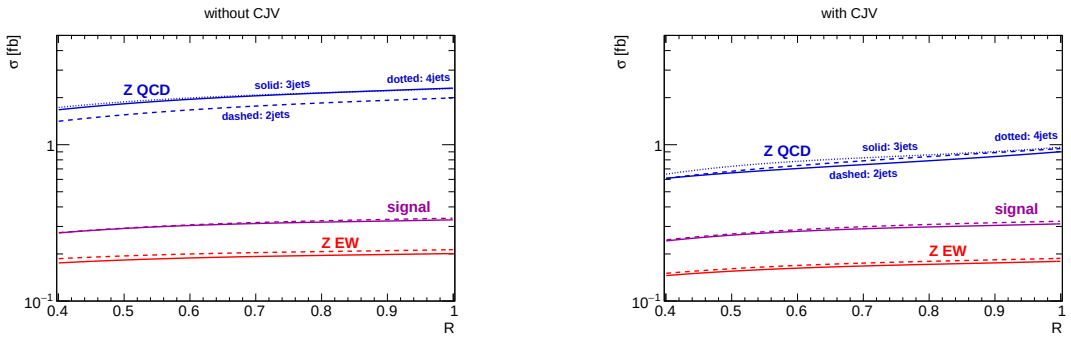

Figure 4.4: WBF signal and Z background cross section dependence on R without (left) and with (right) central jet veto. We always require the basic acceptance cuts of Eq. (4.3). Figures taken from Ref. [1].

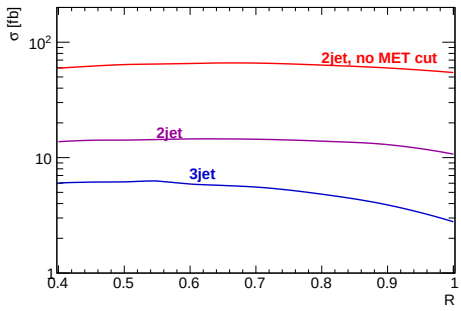

Figure 4.5: Dependence of the $(Z \to jj)h$ rate on R with the basic cuts of Eq. (4.7). Figure taken from Ref. [1].

for a sample with up to four merged hard jets. All rates increase with larger jet sizes, as expected. Moreover, we cannot observe any difference between the samples simulating additional hard jets and those generating theses jets in the parton shower.

Comparing the slopes of the R-dependencies of the WBF signal and its electroweak and QCD Z+jets background processes in the left panel of Fig. 4.4, we find that the QCD background growth slightly faster with an increased jet-radius parameter. The reason for this behavior is the larger rate of jet radiation for the QCD process because of its external gluons. In order to compare more similar topologies and setups for the QCD and electroweak processes, we apply a standard central jet veto on jets with

$$p_{T,j_3} > 20 \text{ GeV} \qquad \min \eta_{j_{1,2}} < \eta_{j_3} < \max \eta_{j_{1,2}} \,. \tag{4.5}$$

This cut will reduce the considered event samples to those with low jet activity in the central detector, i.e. to samples with additional jet radiation in the direction of the tagging jets only. In the right panel of Fig. 4.4 we see that this cut leaves the rates of the electroweak signal and backgrounds largely unchanged, while it dramatically cuts on the QCD background. The R-dependence of the different signal and background processes does not alter significantly after the application of a central jet veto.

To test if the rather strong dependence of the signal and background rates of the jet size is a feature of the WBF topology, we will analyze a process with the same final state as our signal, but with a different topology, namely

$$pp \to Zh_{\text{inv}} \to jj\, h_{\text{inv}} \,. \tag{4.6}$$

In the Zh channel, the two-jet system has a much clearer structure than for the WBF topology. Its invariant mass is fixed by the mass of the Z boson and the angular separation of the two jets is directly related to the boost of the Z boson. For the generation of Zh events, we again merge up to three jets, and employ parton showering and detector simulation. To select the Zh topology, we apply the experimentally motivated cuts [174]

$$\begin{aligned} N_{\text{jets}} &= 2,3 & p_{T,j_1} &> 45\,\text{GeV} & p_{T,j_{2,3}} &> 20\,\text{GeV} \\ \Delta R_{jj} &= 0.7 \ldots 2.0 & m_{jj}(2\,\text{jets}) &= 70 \ldots 100\,\text{GeV} & m_{jj}(3\,\text{jets}) &= 50 \ldots 100\,\text{GeV} \\ \not{E}_T &= 120 \ldots 160\,\text{GeV} \,. \end{aligned} \tag{4.7}$$

In Fig. 4.5 we display the R-dependence of the Zh topology. We find that for small jets, the dependence on the jet-radius parameter is relatively weak. For larger jets we observe a drop of the three-jet rate around $R = 0.55$ and around $R = 0.9$ for the two-jet rate. These declines of the rate are a characteristic of the Zh topology which results in a boosted Z-boson recoiling against the missing momentum and, potentially, a third jet. The two jets originating from the decay of the boosted Z boson are thus expected to have a relatively small angular separation. The observed drops in the two-jet and three-jet

rates correspond to the points where the large jet size finally captures both partons emerging from the Z boson decay and merges them into a single jet. To prove this assumption, we study the two-jet sample without the hard cut on $\not{E}_T$ applied as part of the cuts in Eq. (4.7). Relieving this cut will allow for less boosted Z bosons in our event sample which result in a larger angular separation of the emerging jets, making it less likely that they are merged. Indeed, we now observe a relative growth of the cross section for the two-jet sample without the hard cut on $\not{E}_T$ which is comparable to the one for the WBF signal.

Altogether, we find that the R-dependence of rate measurements is not a feature of the WBF signal and its backgrounds. In fact, we observe a much stronger impact of the jet-radius parameter on the rate of the Zh topology. The influence of the R parameter on rates is an effect of extra jet radiation, depending on the relevant phase-space regions rather than on the process tested.

4.4 Tagging-jet parton content and quark/gluon discrimination

After the pre-selection cuts of Eq. (4.3) the backgrounds to invisible Higgs decays in WBF is clearly dominated by QCD processes radiating a weak boson, $V = W, Z$, see Fig. 4.4. The standard procedure of reducing these QCD backgrounds is applying a veto on central jets [144,148]. To further discriminate between the signal and the QCD backgrounds, we should make use of the kinematic information on the additional jets beyond the level of a veto [148]. Here, we will examine the potential of using observables linked to quark vs gluon discrimination [197–201] to control the QCD backgrounds [202]. We should start our discussion of quark/gluon discrimination with a definition of what we mean by a quark or gluon jet. Here, we will pragmatically define a quark (gluon) jet as what results from the showering of a quark (gluon) parton. To understand which observable differences between quark- and gluon-initiated jets we can actually expect, let us have a look at the Altarelli-Parisi splitting functions [203], i.e. the probability density functions for parton splittings. The function $P_{y\leftarrow x}(z)$ describes the probability of a parton x to emit a parton y with the momentum fraction $z = p_y/p_x$ (leaving a momentum of $(1-z)$ for the second parton)

$$\begin{aligned} P_{g\leftarrow q}(z) &= C_F \left(\frac{1+(1-z)^2}{z} \right) \\ P_{g\leftarrow g}(z) &= 2\, C_A \left[\frac{1-z}{z} + \frac{z}{1-z} + z(1-z) \right] \\ P_{q\leftarrow g}(z) &= \frac{1}{2} \left(z^2 + (1-z)^2 \right) , \end{aligned} \tag{4.8}$$

where $C_F = 4/3$ and $C_A = 3$ are the factor of the Casimir operators of the fundamental and adjoint representation respectively. Notice the symmetric form of $P_{g\leftarrow g}(z)$ and $P_{q\leftarrow g}(z)$ with respect to the exchange of $z \leftrightarrow 1-z$ which is a natural consequence of the final-state particles being indistinguishable. The splitting $q \to q$ follows directly from $P_{q\leftarrow q}(z) = P_{g\leftarrow q}(1-z)$.

What does Eq. (4.8) tell us about the expected behavior of quark and gluon jets? The first and most obvious observation is that quark splittings go with C_F, while the dominant gluon splittings are proportional to C_A. Therefore, we expect the number of splittings of a gluon jet to be larger than the number of splitting of a quark jet by a factor $C_A/C_F = 9/4$. Moreover, we presume the distribution of the momentum on the two resulting partons of a splitting to be different for quark- and gluon-initiated jets. After the splitting of a gluon, described by $P_{g\leftarrow g}(z)$ and $P_{q\leftarrow g}(z)$, an asymmetric distribution of the momentum fraction on the two resulting partons is favored. This asymmetry is very strong for a splitting into two gluons which diverges for $z \to 0$ as well as $z \to 1$ and a lot milder for a splitting into two quarks. For the splitting of a quark as the initial parton, the radiated gluon is likely to be very soft, as described by the divergence for $z \to 0$ of $P_{q\leftarrow g}(z)$. Generally, a gluon jet will lead to wider angle soft emissions, while a quark jet is more likely to result in a quark carrying most of the momentum accompanied with soft gluons.

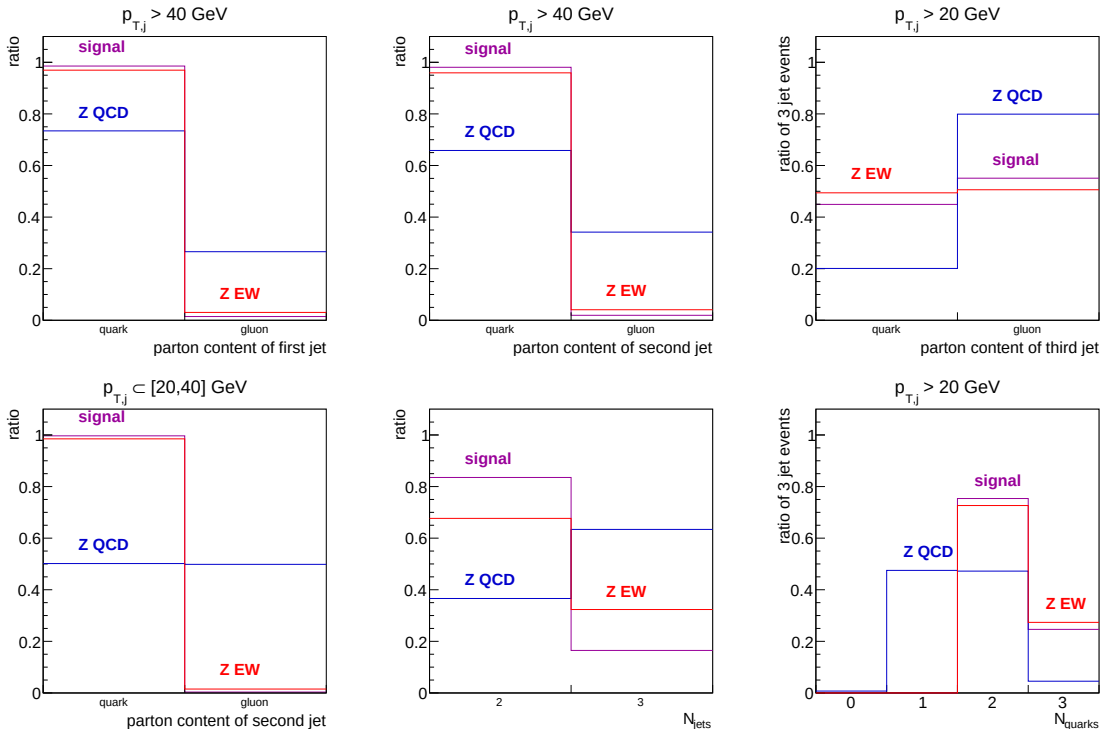

Figure 4.6: Parton content of the first, second, and third jet for the WBF signal and the backgrounds, after the pre-selection cuts of Eq. (4.3). In addition, we show the parton content of the second jet in the slice $p_{T,j_2} = 20 \ldots 40$ GeV, the number of jets, and the number of quarks in three-jet events. Figures taken from Ref. [1].

In order to estimate the potential of the application of quark/gluon discrimination to the WBF signal and the QCD backgrounds, we first examine the partonic nature of their jets. We will show that in fact the jets of the WBF signal events are more likely to be quark-initiated than the jets of the QCD backgrounds. For this parton-level illustration we focus on Z+jets backgrounds as we have seen in Section 4.2 that the W+jets backgrounds behave very similarly. We do not apply a detector simulation, but we still try to stay as close to the kinematic cuts of the detector-level analysis as possible. Therefore, we apply all pre-selection cuts of Eq. (4.3) with the exception of the cut on missing transverse energy. As the $\not{E}_T$ variable is strongly influenced by detector effects, we will use a weaker parton-level cut $p_T > 80$ GeV for the Higgs and the Z-boson.

We expect the two tagging jets in WBF signal events to originate (almost entirely) from quarks, as confirmed in Fig. 4.6. If a third jet is present in the WBF signal events, it is, somewhat counter-intuitively, equally likely to be initiated by a quark or gluon. Around 50% of the events for which the third jet is a quark come from events with two quarks and one gluon where the gluon is harder than at least one of the quark jets, the other half is due to three quark events. The simple corresponding Feynman diagrams are given in Fig. 4.7.

The electroweak Z+jets background shows essentially the same partonic nature as the signal for all jets, see Fig. 4.6. However, the percentage of events with three jets is slightly larger for the electroweak

Figure 4.7: Three-jet contribution to the WBF signal with two or three quarks in the final state.

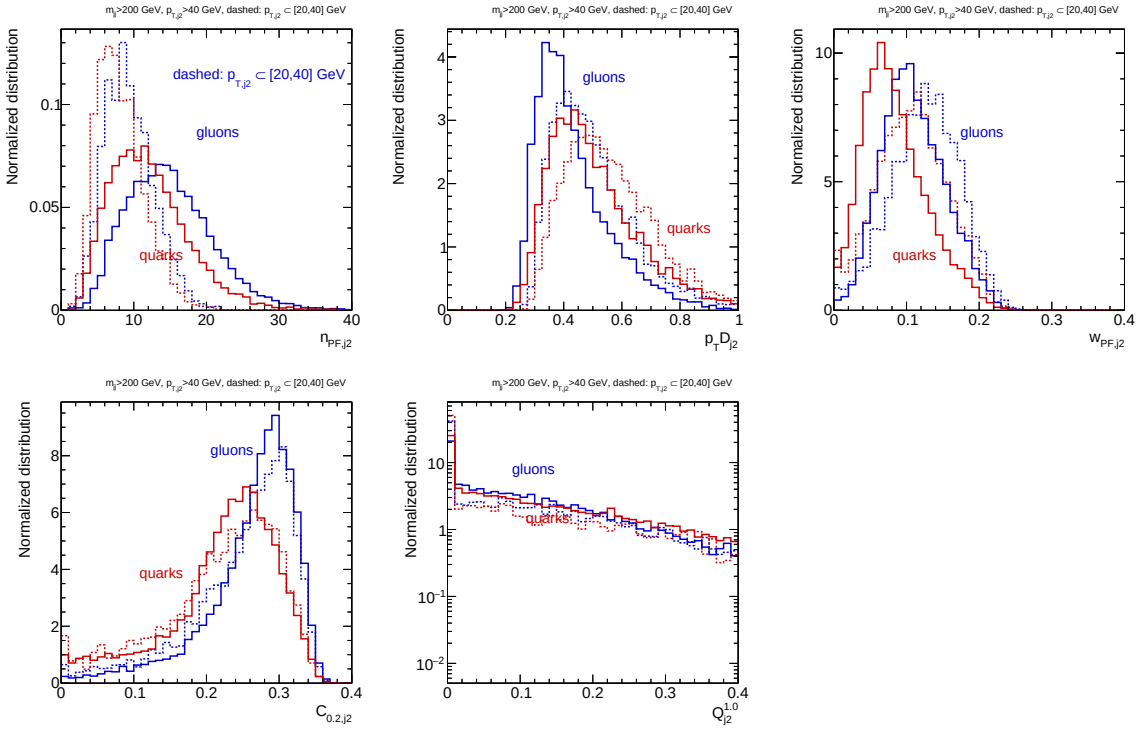

Figure 4.8: Distribution of the quark vs gluon discrimination variables listed in Eq. (4.9) for the second jet in a pure QCD Zjj sample. We show partonic two-quark and two-gluon final states requiring $m_{jj} > 200$ GeV combined with the two slices $p_{T,j_2} = 20 \ldots 40$ GeV and $p_{T,j_2} > 40$ GeV. Figures taken from Ref. [1].

Z+jets background, reflecting the large number of topologies contributing to this background [149–154]. The composition of the jets in the QCD background in terms of quark- and gluon-initiated jets is completely different. The hardest tagging jet arises from a gluon in approximately 30% of the events. For the second jets, this fraction grows to around 35% and reaches 80% for a possible third jet. Comparing the composition of the different jets in terms of quarks and gluons for the QCD backgrounds and the signal, we expect the second tagging jet to have the best discrimination power. We know, however, that the parton content also depends on the transverse momentum cut on the jet, as displayed in the lower panels of Fig. 4.6. The discrimination power of a potential third jet will benefit from a lower p_T threshold.

The above considerations show that indeed the composition of the jets in terms of their parton content may be useful to separate between the WBF signal and QCD backgrounds. We will now study appropriate observables to discriminate between quark- and gluon-initiated jets. Those observables are generally based on the fact that gluons will lead to more and wider emission splittings than quarks, as discussed in and right below Eq. (4.8). Standard variables which can be easily expressed in terms of particle flow (PF) objects or charged tracks as implemented in DELPHES3.3 include [199, 204–207]

$$
\begin{aligned}
n_{\text{PF}} &= \sum_{i_{\text{PF}}} 1 & C &= \frac{\sum_{i_{\text{PF}},j_{\text{PF}}} E_{T,i} E_{T,j} \ (\Delta R_{ij})^{0.2}}{\left(\sum_{i_{\text{PF}}} E_{T,i}\right)^2} \\
p_T D &= \frac{\sqrt{\sum_{i_{\text{PF}}} p_{T,i}^2}}{\sum_{i_{\text{PF}}} p_{T,i}} & Q^\kappa &= \frac{\sum_{i_{\text{trk}}} q_i \, p_{T,i}^\kappa}{\sum_{i_{\text{trk}}} p_{T,i}^\kappa} \\
w_{\text{PF}} &= \frac{\sum_{i_{\text{PF}}} p_{T,i} \, \Delta R_{i,\text{jet}}}{\sum_{i_{\text{PF}}} p_{T,i}} \, .
\end{aligned}
\tag{4.9}
$$

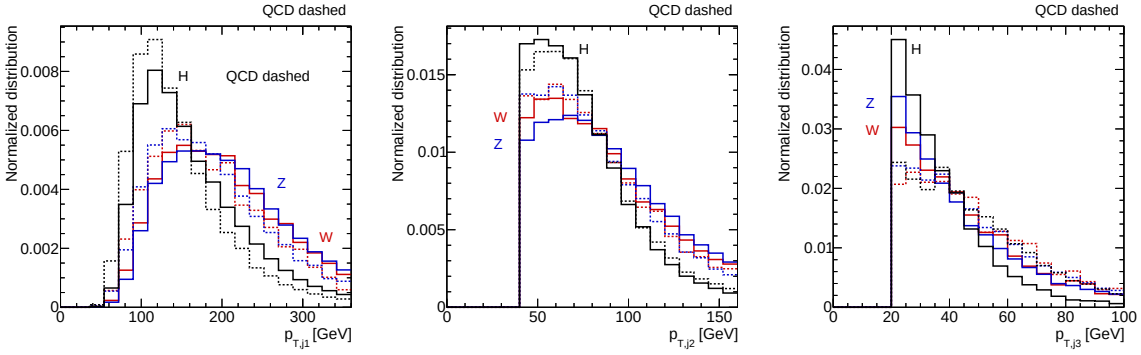

Figure 4.9: Transverse momentum distribution of the three jets for the WBF signal and the EW and QCD (dashed) V+jets background, after the pre-selection cuts of Eq. (4.3). Figures taken from Ref. [1].

First, we compare these variables for two idealized samples of exclusive QCD Zjj events, consisting either purely of two quarks or two gluons in the final state. We apply a parton shower and the DELPHES3.3 detector simulation on the samples and only require the minimal selection cut $m_{jj} > 200$ GeV. We define all observables in Eq. (4.9) except for Q^κ on particle flow objects inside an anti-k_T jet with a radius parameter $R = 0.4$. In Fig. 4.8, we present the distributions of the quark/gluon discrimination variables. We show the results for the second tagging jet in two slices

$$p_{T,j_2} = 20 \ldots 40\,\text{GeV} \qquad \text{and} \qquad p_{T,j_2} > 40\,\text{GeV}\,. \tag{4.10}$$

In all distributions except for $Q^{1.0}$, we observe a clear difference between the samples containing quarks or gluons only. The number of particle flow objects n_{PF,j_2} is larger for the gluon jets, as they are more likely to split and will therefore lead to more individual tracks in the jet area. Moreover, jets with a larger transverse momentum will lead to more particle flow objects. In fact, the influence of the momentum on the distributions of n_{PF,j_2} is significantly larger than the variation induced by the different splitting functions of quarks and gluons. The $p_T D$ variable is a measure for the energy decomposition of the jet momentum on its individual constituents. It is 1 for a jet consisting of a single component and tends to 0 for an equal decomposition of the jet momentum on an infinite number of constituents. Gluons will therefore lead to lower values of $p_T D$. Overall, the distribution of the $p_T D$ variable is similar to that of n_{PF,j_2}, with a reduced dependence on the transverse momentum of the jet. The variables w_{PF} and C make use of the angular distance between the constituents of a jet and its central jet axis or the other jet constituents respectively. As we expect wider splitting for gluons, we observe smaller values for theses observables for the sample of purely quark-initiated jets. For the object-object correlator C, the quark/gluon discrimination is almost entirely de-correlated from the transverse momentum of the jet. Finally, for $Q^{1.0}$ we find very similar distributions of the quark and gluon samples. We will therefore ignore this variable in the following study of quarks/gluon discrimination for WBF events. On the other hand side, the similarity of the discrimination power of the four other variables in our toy example and their strong dependence on the transverse momentum suggests testing those discriminators in a more realistic environment. We will therefore compare their performance for WBF using a dedicated multivariate analysis.

After having established that the WBF signal and its QCD background indeed differ in the parton content of the tagging jets and that we can define observables on PF-level which allow to separate quarks and gluons, we will now apply quark/gluon discrimination variables to the fully simulated tagging jets in our Higgs to invisibles search. We use the same SHERPA simulation as before with two jets for the gluon-fusion signal contribution and up to three hard jets merged for all other samples and a DELPHES3.3 fast detector simulation. We again cluster our jets using the anti-k_T algorithm with $R = 0.4$. After showering and detector simulation, the parton content of the jets in our event samples is no longer well-defined. The question is now how much of the basic parton-level differences

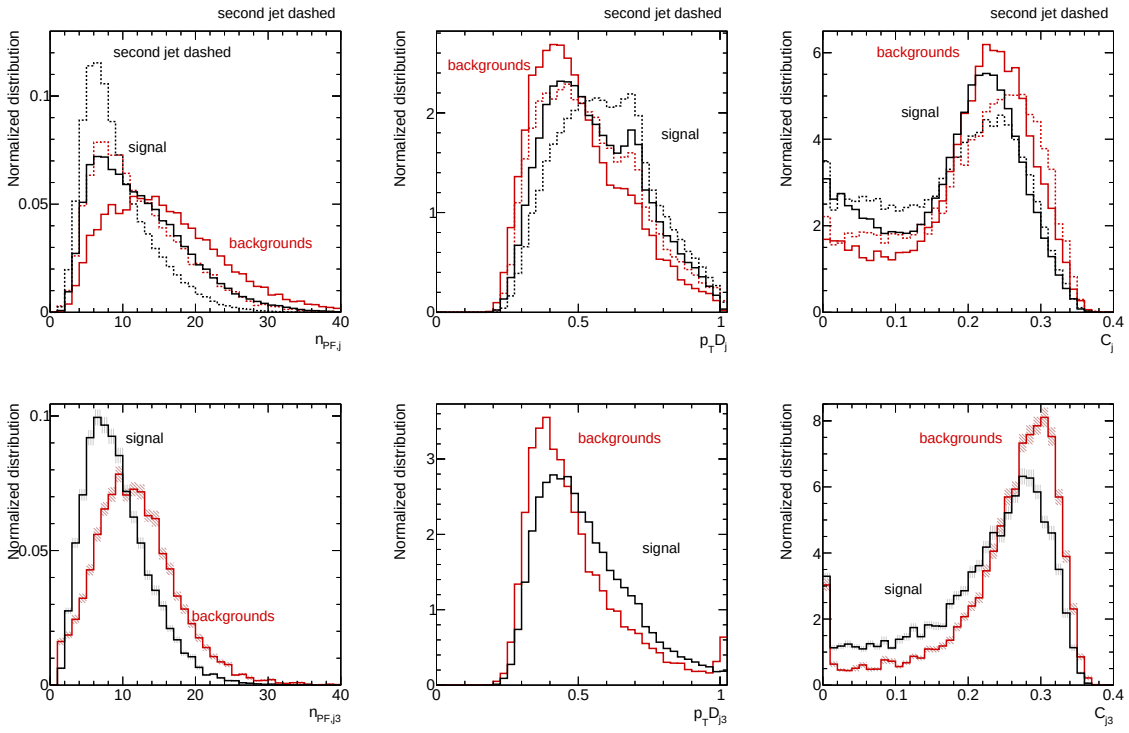

Figure 4.10: Distribution of the quark vs gluon discrimination variables n_{PF}, $p_T D$, and C for the WBF signal and the combined QCD and electroweak V+jets background, after the pre-selection cuts of Eq. (4.3). In the top panels we show the tagging jets, while in the bottom panels we show the softer third jet. Figures taken from Ref. [1].

in our signal and background samples remains visible in the hadron-level analysis based on the PF observables defined in Eq. (4.9).

We have already seen above in Fig. 4.8 that some of the distributions of the quark/gluon discrimination variables reflect not only the parton content on the jet, but also its transverse momentum. In our realistic sample of the WBF Higgs signal and the QCD Z+jets background both these effects will of course be present. In Fig. 4.9, we display the transverse momentum distributions of the two tagging jets and a potential third jet for the WBF signal and its QCD and EW backgrounds separately. Neglecting trigger requirements, we allow the third jet to be as soft as $p_{T,j} = 20$ GeV. For the tagging jets of the WBF Higgs signal, the p_T-distributions peak around 100 ... 120 GeV and 50 ... 70 GeV for the first and second jet, respectively. As a result, the pre-selection cuts of Eq. (4.3) will only affect the transverse momentum distributions mildly. The jets of the QCD backgrounds are typically neither forward nor at large transverse momenta. The application of the tagging-jet cuts of Eq. (4.3) results in a spectrum with harder tagging jets than we observe for the signal.

As we have just seen, the backgrounds for the process we are considering are gluon-dominated and harder. Comparing the observation with the distributions in Fig. 4.8, we expect the two effects strengthen each other for n_{PF} as well as $p_T D$ and to weaken each other for w_{PF}. For the observable C which is rather insensitive to the transverse momentum of the jets, we cannot make such statements. Obviously, we would want a quark/gluon discrimination variable to disentangle the effect of the different p_T spectra from the parton nature. However, we expect that systematic uncertainties might significantly affect on this de-correlation for some of the PF observables.

Finally, to check our expectations in Fig. 4.10 we display the distributions of the leading three observables $n_{\mathrm{PF}}, p_T D$, and C for the WBF signal, including its gluon fusion contribution, and the combined V+jets backgrounds. In the first row, we show the distributions for the first and second (dashed) tagging jet, while the distributions for a potential softer third jet are shown in the second row. As

expected, the number of PF objects n_{PF} has the best separation power for the first, hardest jet. For the second jet, however, $p_T D$ shows the best performance. The second peak in the $p_T D$ distribution for the signal and the electroweak backgrounds is an artifact of the pre-selection cuts.

For events with three jets we find that n_{PF} as well as C turn out to be promising observables to separate the WBF Higgs signal from its backgrounds. The fact that the n_{PF} distribution for the third jet peaks at a very similar position as for the second tagging jet is accidental and an effect of the smaller transverse momentum of the third jet.

4.5 Performance and triggering

After discussing subjet-level input variables for WBF in the last section, we now want to examine their potential to increase the LHC sensitivity for invisible Higgs decays. We analyze the reach of the WBF channel in a multivariate analysis using boosted decision trees in TMVA [208, 209]. We compare benchmarks including different sets of jet-level and subjet-level discrimination variables as inputs for the classification. The included variables are listed in Tab. 4.1. For the BDT settings, we choose the AdaBoost algorithm [210] with 70 trees, a maximum depth of 3 and require a minimum node size of 5% of the number of events.

We present our results in terms of the ROC curves, i.e. curves of the signal efficiency vs inverse background efficiency, in Fig. 4.11 for different sets of BDT input variables. As our baseline scenario, in all panels Fig. 4.11, we show the results from a BDT using the full set of standard WBF variables, containing the jet-level (p_T, η, ϕ) information on the tagging jets and a possible third jet, provided $p_{T,j_3} > 20$ GeV. In the left panel, we compare it to a BDT which in addition uses the subjet-level observables n_{PF}, C, $p_T D$. As a measure of the most sensitive observable, we quote the variable most often used for the splittings of the BDT which is $\Delta\eta_{j_1,j_3}$ in both cases. The BDT is making use of this variable reduce the contribution from events with central third jets. On subjet-level, the most powerful discriminators are n_{PF} and the $p_T D$ of the third jet. They are ranked, however, only after the angular separation variables of the jets. This poor ranking of the subjet-level variables is confirmed by the fact their inclusion in the BDT analysis does not lead to a visible improvement of the classification power in the left panel of Fig. 4.11. We find similar results in the central panel, where we again compare the classification power of the BDTs including or not the subjet-level variables as input parameters, this time based on the two tagging jets alone. The most powerful discriminator turns out to be $\Delta\phi_{jj}$ for the tagging jets. The subjet-level information most often used by the BDT is the variable n_{PF,j_1}. It is however, only ranked fifth. Even for a $2 \to 3$ process, the information on the event kinematics seems to be saturated already by the large number of jet-level observables listed in Tab. 4.1. The addition of subjet-level information will hence only have a very limited impact on the performance of the separation of the WBF signal from its backgrounds.

It has been shown in a recent study [148] that the sensitivity of the WBF analysis as a search channel for Higgs decays to invisible particles can be increased by using information on softer central jets. This is complicated by the fact that the energy of those soft central jets is hard to calibrate. Considering a soft central jet as a container for subjet-level observables only and omitting the jet-level p_{T,j_3} as

Set	Variables
jet-level j_1, j_2	p_{T,j_1} p_{T,j_2} $\Delta\eta_{jj}$ $\Delta\phi_{jj}$ m_{jj} $\not{E}_T$ $\Delta\phi_{j_1,\not{E}_T}$ $\Delta\phi_{j_2,\not{E}_T}$
subjet-level j_1, j_2	n_{PF,j_1} n_{PF,j_2} C_{j_1} C_{j_2} $p_T D_{j_1}$ $p_T D_{j_2}$
j_3 angular information	$\Delta\eta_{j_1,j_3}$ $\Delta\eta_{j_2,j_3}$ $\Delta\phi_{j_1,j_3}$ $\Delta\phi_{j_2,j_3}$
jet-level j_1-j_3	jet-level j_1, j_2 + j_3 angular information + p_{T,j_3}
subjet-level j_1-j_3	subjet-level j_1, j_2 + n_{PF,j_3} C_{j_3} $p_T D_{j_3}$

Table 4.1: Sets of variables used for the BDT analysis. Variables with the subscript jj refer to the two tagging jets.

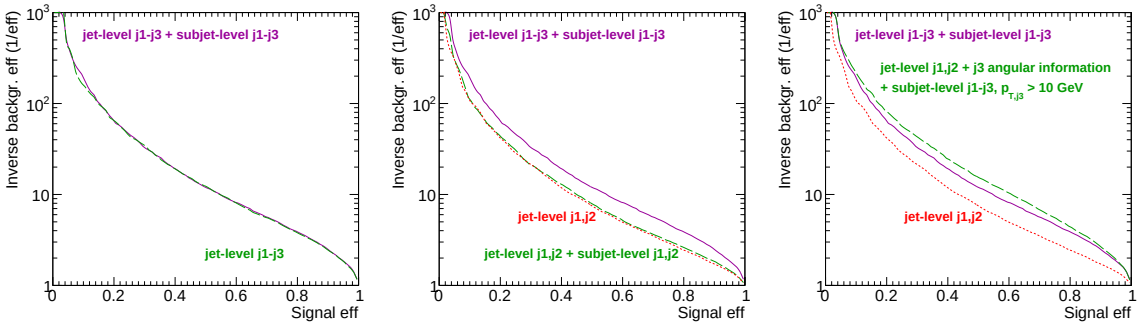

Figure 4.11: Signal efficiency vs inverse background efficiency based on jet-level and additional subjet-level information of the leading three jets (left). In the central panel we show the jet-level and subjet-level of the tagging jets only, while to the right we include the subjet-level information on the third jets with a lower threshold of $p_{T,j_3} > 10$ GeV. Figures taken from Ref. [1].

an input parameter, we want to avoid this limitation. In the right panel of Fig. 4.11, we show the performance of a BDT analysis including the jet-level angular information and subjet-level information on a soft third jet. The most powerful discriminator is now n_{PF,j_3} and we see a significant increase of the performance of the analysis with respect to the previously discussed scenarios. We have explicitly checked that adding the information on the jet-level p_{T,j_3} to the input variables does not further increase the performance of the BDT, i.e. that this information is already encoded in the subjet-level variables. We are aware that including all subjet-level observables of Eq. (4.9) in this analysis is likely overly optimistic. Instead, a proper analysis in terms of track jets with dedicated tunes of the simulation tools should be performed. Our promising results motivate such an in-depth analysis. However, it is beyond the reach of this first preliminary study.

As for many hadronic signatures, a major issue for WBF Higgs analyses at the HL-LHC and invisible Higgs searches in particular will arise from detector limitations and trigger thresholds. We expect the pre-selection cuts of Eq. (4.3) to be overly optimistic for a high-luminosity upgrade of the LHC and will systematically study the impact of raising the trigger thresholds on different variables in the following. For this, we will compare the expected limits on invisible Higgs decays for different pre-selection cuts using an implementation of the CLs method [211] in CheckMate [212]. Specifically, we will test the influence of cuts on the missing transverse energy, the transverse momentum of the tagging jets and their invariant mass. We will rerun our BDT analyses after different pre-selection cuts on those input variables and obtain the corresponding signal and background efficiencies in terms of a ROC curve. For each point on this curve, we can calculate the 95% CLs limit, respecting the cross section after our pre-selection cuts of Eq. (4.3) and assuming a systematic uncertainty of 3%. We then quote the best limit for each cut configuration.

In Fig. 4.12, we show the resulting 95% CLs limits for different trigger threshold for missing energy, the invariant mass and the transverse momentum of the tagging jets for two integrated luminosities of 300 fb^{-1} and 3000 fb^{-1}. We compare the reach of the WBF Higgs analysis with the expected reach of the leptonic Zh analysis which we present in Appendix A.3. We find that the pre-selection cuts on the missing transverse energy or the transverse momentum of the tagging jets significantly reduce the sensitivity of the WBF analysis, while its reach seems to be largely independent of the minimum cut on the invariant mass of the tagging jets or, equivalently, their rapidity separation.

Given the current trigger thresholds, the reach of the WBF analysis for constraining invisible Higgs decays is at the level of 5% for an integrated luminosity of 300 fb^{-1} and at the level of 3% for 3000 fb^{-1}. Increasing the trigger cut on missing transverse energy from its current value $\not{E}_T > 140$ GeV to $\not{E}_T > 200 \ldots 300$ GeV reduces the sensitivity to invisible Higgs decays by roughly a factor of 1.5 ... 2.7. We extend the presented limits on the branching ratio the regime below $\not{E}_T > 140$ GeV. However, we should keep in mind that in this region we will likely have to take into account additional background contribution. We have already discussed the transverse momentum distribution of the tagging jets

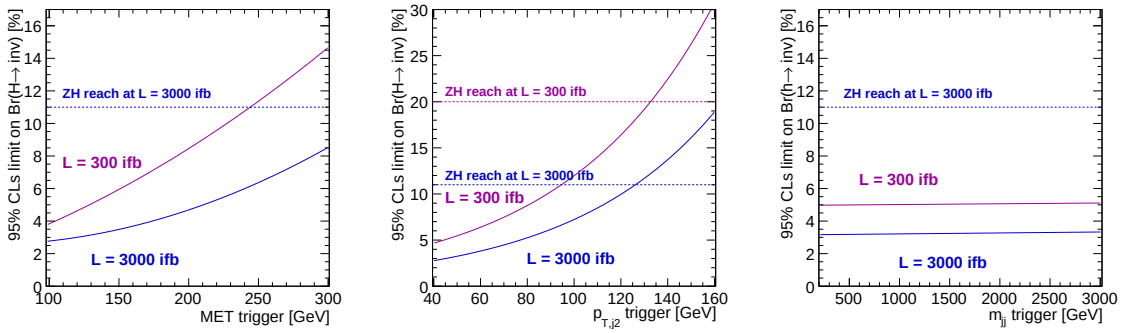

Figure 4.12: CLs limits on invisible Higgs decays from weak boson fusion, as a function of trigger cuts on missing transverse energy (left), the transverse momentum of the tagging jets (center), and the invariant mass of the tagging jets (right). As a reference we also display the reach in the leptonic Zh channel, described in the Appendix A.3. Figures taken from Ref. [1].

and the importance of the trigger threshold on this observable in Fig. 4.9. The minimum $p_{T,j}$ cut has a strong impact on the reach of the WBF search. Increasing the pre-selection cut to the level of $p_{T,j_{1,2}} > 130$ GeV even reduces the WBF sensitivity to below the Zh reference point.

Finally, increasing the trigger on the invariant mass of the tagging jets m_{jj} leaves the sensitivity of the analysis almost unchanged, even up to the level of $m_{jj} > 2500$ GeV. As the invariant mass is strongly correlated with the angular separation of the jets in terms of $\Delta\eta_{jj}$, we have explicitly tested that pre-selection cuts on $\Delta\eta_{jj} > 7$ will equivalently have no impact on the reach of the invisible Higgs branching ratio.

4.6 Conclusion and outlook

The most sensitive channel for the search for invisible Higgs decays at the LHC is Higgs production in WBF. Its unique signature featuring two tagging jets allows to efficiently suppress the backgrounds. In combination with the relatively large cross section, this renders WBF to process with the largest statistical sensitivity to an invisible Higgs branching ratio.

In this chapter, we have discussed several aspects of WBF tagging jet analyses, aiming at an improvement of the invisible Higgs search strategy. Studying the W+jets and Z+jets backgrounds, we find that such backgrounds can indeed be controlled, but that eventually single-top production will limit their correspondence. Moreover, we examined the dependence of the signal cross-section on the jet-radius parameter and established that its growth is not a result of the WBF topology, but instead a consequence of the selected phase-space region.

The main part of this chapter was dedicated to a systematic study of subjet-level observables for the two tagging jets as well as for possible central jets. The use of the additional subjet-level information allows to suppress the dominant QCD background and increase the purity of the event samples. However, in a multivariate analysis, it will not significantly improve the reach of invisible Higgs searches with respect to analyses based on the complete available set of jet-level observables. This signals that subjet-level information will only over-constrain the WBF search channel which is already fully constrained by the jet-level analysis. However, subjet observables allow us to lift the dependence on a central jet veto. Furthermore, studying the reach of the WBF analysis for jets with low transverse momenta motivates to consider jets as containers for subjet-level information rather than the main analysis objects. A detailed study of the sensitivity of the WBF analysis in terms of track jets is left for the future.

Finally, we have analyzed the reach of invisible Higgs search in weak boson fusion as a function of increased trigger and detector thresholds at the HL-LHC. An increased trigger threshold on the transverse momentum threshold of the tagging jets can seriously weaken the limits on invisible Higgs decays from 2% to beyond 10%, eventually rendering WBF less sensitive than the leptonic Zh channel. On the other hand, an increased trigger threshold on the $\Delta\eta_{jj}$ separation of the tagging jets or, equivalently their invariant mass, has hardly any effect on the sensitivity on the WBF analysis.

5 | A Global View on the Higgs-Gauge Sector for LHC Run II

In this chapter, we present a global analysis of the Higgs and electroweak sectors based on LHC Run I and Run II data and electroweak precision observables from LEP, the Tevatron and the LHC in the SMEFT framework. We compare the relative strength of these data sets for constraining Higgs-related dimension-six operators. In particular, we discuss the importance of the incorporation of fermionic Higgs-gauge operators and electroweak precision data in a global fit. Using SFitter, we combine the available LHC rate measurements of the Higgs sector, kinematic distributions for associated Higgs production as well as di-boson production, and electroweak precision observables.

The content of this chapter is based on work in collaboration with Tyler Corbett and Tilman Plehn [3]. Most of the figures and tables as well as a significant part of the text are taken from the corresponding publication. The credit for most of the study of the operator $\mathcal{O}_{tG}$ and the implementation of the constraints from electroweak precision observables is entitled to Tyler Corbett.

5.1 Introduction

One of the great advantages of the SMEFT framework is its applicability to different sectors of particle physics and its capability to combine measurements from those: There exist global analyses not only of LHC measurements in the Higgs and electroweak gauge sectors, but also in the QCD sector [213–219], the top sector [132, 220–224], or the flavor sector [225]. SMEFT also allows the combination of results from different experiments, for instance the combination of LHC Run I Higgs measurements with LEP data [226–230], some including di-boson production as a probe of anomalous triple gauge vertices [64, 231–236].

In the following, we present an SFitter [54, 237, 238] analysis combining measurements of the Higgs and gauge sector at the LHC with electroweak precision data. LEP limits on di-boson production are not included in the fit, because they are outperformed by the LHC limits in the effective Lagrangian framework, which profit from the increased momentum flow through the effective operators with a momentum dependence [239, 240]. With the improved precision at the level of Run II, we should no longer hard-code the electroweak precision constraints into our operator basis, but include them in our global fit [104, 241–245]. The same fermionic operator that are constrained by electroweak precision data will also affect LHC processes in the Higgs-gauge sector due to the Vqq' and $Vhqq'$ couplings they induce. As the fermionic operators appear in different combinations with the usual bosonic operators, their correlations generally weaken the constraints on operators contributing to Higgs physics only. We will study a number of 20 SMEFT operators of the Higgs-gauge sector, plus invisible decays of the Higgs boson. Since two of these operators will turn out to be very precisely constrained by non-Higgs observables, we will neglect them in our global analysis and include 19 parameters in our global fit.

We will take the usual SFitter approach and evaluate event numbers in total rate measurements and kinematic distributions using our in-house framework instead of relying on pre-defined results from ATLAS and CMS in terms of Higgs signal strength modifiers, whenever those event counts are available. We fully correlate systematic uncertainties between different search channels and use our

own, flat, treatment of theoretical uncertainties, as discussed in Chapter 3.

We start our analysis by discussing the relevant operator basis for the gauge-Higgs sector in Section 5.2. We then discuss constraints from multi-jet and top pair production on two of the included operators in Section 5.3 and compare their reach to the expected sensitivity of LHC Higgs searches.

In Section 5.4, we explain the details of our fit as well as the input data set and we present the global analysis of LHC results and electroweak precision observables in Section 5.5. Starting from a comparison of Run I and Run II constraints with a reduced operator basis, we then add fermionic Higgs-gauge operators and their constraints from electroweak precision observables. Specifically, we will focus on the interplay of fermionic and bosonic operators for LHC Higgs searches and we find that, despite the discrepancy between the generic LHC reach given by Eq. (2.28) and the generic reach of electroweak precision data in Eq. (2.33), fermionic Higgs-gauge operators and bosonic operators should be combined in a global fit. The final fitting setup brings us a significant step closer towards a global SFitter SMEFT analysis which, in the future, should be combined with a fit of the top sector.

5.2 Relevant SMEFT operators

Based on our discussion in Chapter 2 and, in particular, Section 2.3, we will now define the operator basis for our global fit of the gauge-Higgs sector for LHC Run II and electroweak precision observables. We assume flavor universality and neglect CP odd operators, dipole operators and Higgs interactions with light-generation fermions as discussed previously. We start from the effective Lagrangian defined in Refs [63, 64, 96]

$$\begin{aligned}\mathcal{L}_{\text{eff, 1}} = &- \frac{\alpha_s}{8\pi}\frac{f_{GG}}{\Lambda^2}\mathcal{O}_{GG} + \frac{f_{WW}}{\Lambda^2}\mathcal{O}_{WW} + \frac{f_{BB}}{\Lambda^2}\mathcal{O}_{BB} + \frac{f_W}{\Lambda^2}\mathcal{O}_W + \frac{f_B}{\Lambda^2}\mathcal{O}_B \\ &+ \frac{f_{\phi 2}}{\Lambda^2}\mathcal{O}_{\phi 2} + \frac{f_{WWW}}{\Lambda^2}\mathcal{O}_{WWW} \\ &+ \frac{f_\tau m_\tau}{v\Lambda^2}\mathcal{O}_{e\phi,33} + \frac{f_b m_b}{v\Lambda^2}\mathcal{O}_{d\phi,33} + \frac{f_t m_t}{v\Lambda^2}\mathcal{O}_{u\phi,33} + \text{invisible decays}\,, \end{aligned} \tag{5.1}$$

using the operator definitions in Eqs. (2.8)–(2.11). For the inclusion of Higgs decays to invisible particles, we refrain from adding them in terms of the effective Lagrangian in Eq. (5.1). For this we would need to either re-scale the decay $H \to 4\nu$ to ridiculous branching ratios or define a new, undetectable, particle with unknown quantum numbers. Instead, we will include invisible Higgs decays as a contribution to the total Higgs width, or, equivalently, as a modification of the invisible Higgs branching ratio. As we have seen in Chapter 4, it is best constrained through WBF Higgs production [1, 144, 148]. The total Higgs width is then consistently constructed out of all partial widths.

In addition, we explicitly include the operators with tree-level contributions to electroweak precision observables, as we know that at the level of 13 TeV data the corresponding operators should not be neglected [66, 103, 104, 241–245]

$$\begin{aligned}\mathcal{L}_{\text{eff,2}} = &\frac{f_{\phi Q}^{(1)}}{\Lambda^2}\mathcal{O}_{\phi Q}^{(1)} + \frac{f_{\phi d}^{(1)}}{\Lambda^2}\mathcal{O}_{\phi d}^{(1)} + \frac{f_{\phi u}^{(1)}}{\Lambda^2}\mathcal{O}_{\phi u}^{(1)} + \frac{f_{\phi e}^{(1)}}{\Lambda^2}\mathcal{O}_{\phi e}^{(1)} + \frac{f_{\phi Q}^{(3)}}{\Lambda^2}\mathcal{O}_{\phi Q}^{(3)} \\ &+ \frac{f_{\phi 1}}{\Lambda^2}\mathcal{O}_{\phi 1} + \frac{f_{BW}}{\Lambda^2}\mathcal{O}_{BW} + \frac{f_{LLLL}}{\Lambda^2}\mathcal{O}_{LLLL}\,. \end{aligned} \tag{5.2}$$

Finally, we will discuss the influence of the operators

$$\mathcal{L}_{\text{eff,3}} = \frac{f_{\phi 3}}{\Lambda^2}\mathcal{O}_{\phi 3} + \frac{f_{tG}}{\Lambda^2}\mathcal{O}_{tG} + \frac{g_s f_G}{\Lambda^2}\mathcal{O}_G\,. \tag{5.3}$$

All operators are defined in Eqs. (2.8)–(2.15). The three operators listed in Eq. (5.3) are in principle relevant for Higgs physics. However, as we will discuss later, they cannot be studied at the LHC yet or are much more strongly constrained from other LHC measurements. They will therefore not be taken into account in our global fit. The first operator we neglect is $\mathcal{O}_{\phi 3}$. It contributes to the hhh vertex [2, 13, 246–249] which cannot be measured at the LHC yet. For a potential high-energy

upgrade of the LHC, the study of the Higgs self-couplings by measuring di-Higgs production will be one of the milestones of its physics program. We will discuss the limits on $\mathcal{O}_{\phi 3}$ in a global fit for a potential 27 TeV upgrade of the LHC in Section 6.4. The operators $\mathcal{O}_G$ and $\mathcal{O}_{tG}$ are highly constrained by measurements of multi-jet production and top pair production respectively. We will discuss their constraints in Section 5.3.

We are left with as set of 18 dimension-six operators, eight of which, given in Eq. (5.2), influence electroweak precision observables at tree level. One of the key improvements of this work with respect to previous SFitter analyses of the Higgs-gauge sector is the inclusion of those operators in our global fit. Since the fermionic Higgs-gauge operators modify the couplings of the weak gauge bosons to fermions, see Tab. 2.4, they are highly constrained by the electroweak precision observables, see our discussion in Section 2.5 and, in particular, Eqs. (2.31) and (2.32) for the list of included Z-pole and W boson observables.

5.3 Constraints from the QCD and top sectors

As a hadron collider, the LHC is heavily influenced by gluon self-interactions and is accurately testing our understanding of them. The anomalous triple gluon coupling should therefore be added to any global analysis of LHC physics

$$\mathcal{O}_G = f_{abc} G^{\rho}_{a\nu} G^{\nu}_{b\lambda} G^{\lambda}_{c\rho} \qquad \text{with} \qquad \mathcal{L}_{\text{eff}} \supset \frac{g_s f_G}{\Lambda^2} \mathcal{O}_G \,, \tag{5.4}$$

with $G^{\rho\nu}_a = \partial^\rho G^\nu_a - \partial^\nu G^\rho_a - i g_s f_{abc} G^{b\rho} G^{c\nu}$. The operator contributes to any gluon-initiated LHC process, in the Higgs sector for instance to gluon fusion Higgs production in association with a hard jet. Due to its contribution to a wide range of processes, it induces a correlation of measurements from different sectors that would in principle force us to perform a global analysis of *all* LHC measurements. In particular, the operator $\mathcal{O}_G$ is relevant in the context of disentangling the effects $\mathcal{O}_{u\phi,33}$ effects from $\mathcal{O}_{GG}$, as it has been shown in the literature [250] that it is impossible to discriminate between $\mathcal{O}_G$ and $\mathcal{O}_{GG}$ using a single kinematic distribution with an additional hard parton.

Currently, the strongest constraints on anomalous triple gluon couplings come from ATLAS multi-jet data at 13 TeV, giving the 95% CL limits [219]

$$\frac{\Lambda}{\sqrt{f_G}} > 5.2\,(5.8)\ \text{TeV} \qquad \text{observed (expected) from multi-jets.} \tag{5.5}$$

Comparing these limits to the ones in Eq. (2.28), we find that the effects of the operator $\mathcal{O}_G$ on Higgs production rates are limited beyond anything a global Higgs analysis would be sensitive to. We can therefore safely neglect the operator in our analysis.

Analyses of the Higgs sector allow for both direct and indirect measurements of the top-Higgs coupling in gluon fusion and Higgs production in association with a top pair [251,252]. We will see in Section 5.5 how the wealth of available $t\bar{t}h$ measurement helps to disentangle the effects of the operator $\mathcal{O}_{u\phi,33}$ with its Higgs-top couplings from Higgs-gluon couplings induced by $\mathcal{O}_{GG}$. In principle, both gluon fusion (with additional hard jets) and Higgs-top associated production are influenced by the chromo-magnetic top operator [66]

$$\mathcal{O}_{tG} = (\bar{Q}\sigma^{\mu\nu} T^a u_R)\, \tilde{\phi}\, G^a_{\mu\nu} \,. \tag{5.6}$$

It is also relevant for top pair production in the context of top-EFT analyses where its effects have been studied extensively, see e.g. Ref. [220]. In Fig. 5.1, we show the corresponding Feynman diagrams of the interactions induced by the operator $\mathcal{O}_{tG}$. The first pair of diagrams is relevant for top pair production, whereas the second pair contributes to $t\bar{t}h$ production. For both processes, there is an interaction proportional to the momentum flowing through the vertex and a four-particle contact interaction (five-particle for the $t\bar{t}h$ case) vertex. In the following, we want to compare the potential of the Higgs and top sectors for constraining f_{tG}

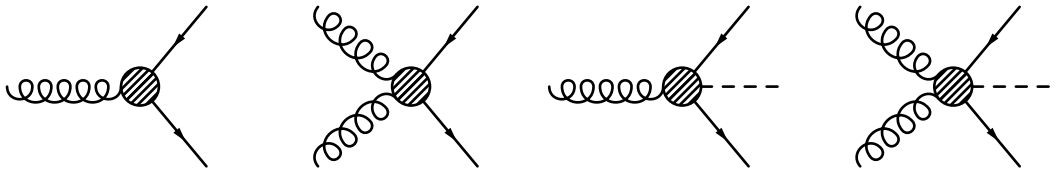

Figure 5.1: Interactions through the chromo-magnetic top operator. The vertices scaling with p^μ come from the derivative in the field strength, while those scaling with v are generated by the nonabelian component. Figure taken from Ref. [3].

In the Higgs sector, we can obtain limits on f_{tG} from gluon fusion or $t\bar{t}h$ production with or without additional jets. Since extra hard gluons in the final state are a typical higher-order effect and likely suppressed, we expect the best constraints from the Higgs sector to be obtained using momentum-related kinematic distributions in $t\bar{t}h$ production. The third vertex in Fig. 5.1 has such momentum dependence, but only includes a single gluon and will therefore be suppressed by an s-channel propagator in the full $t\bar{t}h$ diagram, counteracting the dimension-six momentum enhancement. We estimate the power of Higgs physics for constraining f_{tG} by studying the most promising distribution currently available, the H_T distribution in the all-hadronic

$$pp \to t\bar{t}h \to t\bar{t}\, b\bar{b} \tag{5.7}$$

signature released by CMS [253]. We generate the relevant tth process merged with one additional jet using MADGRAPH5 [254] and PYTHIA8 [255], combined with DELPHES3 [193]. In Fig. 5.2 we reproduce the H_T distribution for two benchmark values of f_{tG}, corresponding to the limits obtained in top sector and Higgs sector fits

$$\begin{aligned} \frac{\Lambda}{\sqrt{|f_{tG}|}} &\gtrsim 1 \text{ TeV} && \text{(top sector [220])} \\ \frac{\Lambda}{\sqrt{|f_{tG}|}} &\gtrsim 320 \text{ GeV} && \text{(Higgs sector [66])}\ . \end{aligned} \tag{5.8}$$

Comparing these top-sector and Higgs-sector constraints with the expected sensitivity for our own study in Fig. 5.2, we see that our limits are not (yet) competitive with the top-sector constraints. The larger sensitivity of top pair production is due both to the large backgrounds that plague $t\bar{t}h$ production and to the small production cross section of $t\bar{t}h$ with respect to $t\bar{t}$ production. In fact, the $t\bar{t}h$ cross section at the LHC is measured to be approximately three orders of magnitude below that of $t\bar{t}$ production at 13 TeV [256, 257].

At higher energies or higher luminosity (where higher energies can be probed with reasonable statistics), however, the hierarchy of the $t\bar{t}h$ and $t\bar{t}$ sensitivity might eventually shift due to the chirality of the final state fermions, as a study of the 14 TeV LHC with a luminosity of 3/ab suggests [251]. In the high energy limit, where the transverse momentum of the top quarks are much larger than the top mass $p_{T,t} \gg m_t$, the top quarks in $t\bar{t}$ production are both of left or both of right chirality $LL + RR$, since the SM $t\bar{t}g$ coupling leaves the chirality unchanged [258], see Fig. 5.3. Both the Higgs-top couplings and the operator $\mathcal{O}_{tG}$ in all its vertices induce a chirality flip. Therefore, in the chiral limit the contributions of the chromo-magnetic operator to top pair production are $LR + RL$ and their interference with the SM is suppressed. For Higgs production in association with a top pair, the chiral limit in the SM is $LR + RL$. Since the chromo-magnetic operator is contributing to both $LL + RR$ and $LR + RL$ final states, as we show in the lower panels of Fig. 5.3, the helicity suppression at high transverse momenta is less pronounced.

At the current LHC energy and luminosity, however, we find that both $\mathcal{O}_{tG}$ and $\mathcal{O}_G$ can be neglected in current global Higgs analyses.

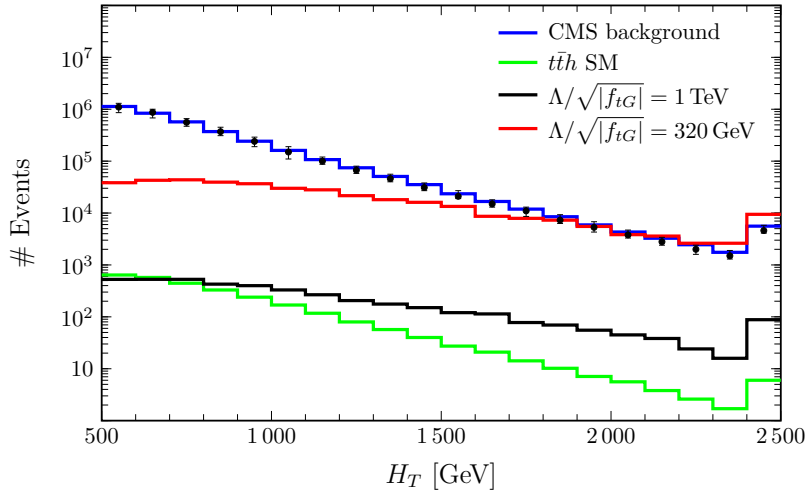

Figure 5.2: H_T distributions for $t\bar{t}h$ production for the Standard Model, $\Lambda/\sqrt{|f_{tG}|} = 1$ TeV corresponding to the top physics limit, and $\Lambda/\sqrt{|f_{tG}|} = 320$ GeV corresponding to the Higgs physics limit. The background estimate and the data points are from Ref. [253]. Figure taken from Ref. [3].

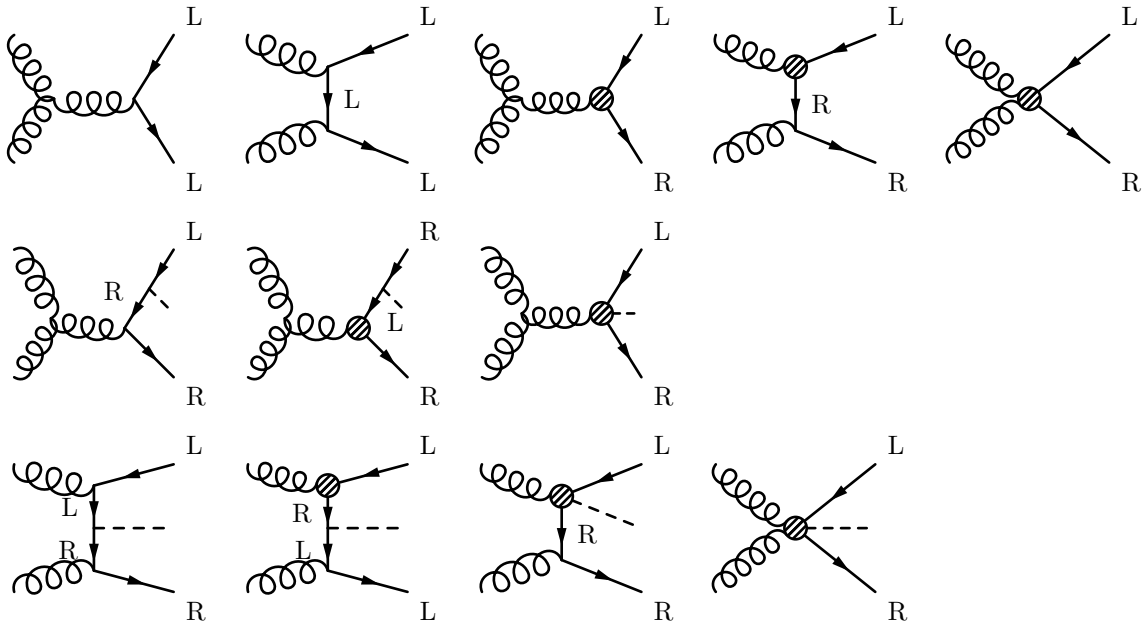

Figure 5.3: $t\bar{t}$ (upper panels) and $t\bar{t}h$ (middle and lower panels) production in the SM and through the chromo-magnetic top operator. The blobs denote insertions of the operator $\mathcal{O}_{tG}$. L and R label the chirality of the fermions.

5.4 Fitting framework and data set

One of the strength of SFitter as a tool for statistical analyses is its ability to deal with various uncertainty distributions and the inclusion of correlations. For our global fit we extract the signal and background rates from the experimental publications, whenever possible, and apply our own uncertainty treatment, instead of relying on the pre-processed coupling strength modifiers by ATLAS and CMS. We fully correlate systematic uncertainties of the same sources (e.g. luminosity) between different experimental channels, and define theoretical uncertainties using a flat likelihood. With the

shift of the experimental collaborations toward the application of multivariate analyses, the number of events quoted for a signal region is more and more frequently illustrated after simple cuts rather than the full analysis. In order not to lose sensitivity, we implement the signal strength modifiers in these cases, but we still apply our own treatment of the uncertainties. When reproducing distributions displayed in the experimental papers, we extract the signal efficiencies and higher-order effects by normalizing to the total event numbers provided by ATLAS and CMS.

Whenever kinematic information is relevant, we generate events for the Higgs and di-boson signals using MadGraph5-2.3.2.2 [254]. We use Pythia6-2.4.5 [255] for parton showering and hadronization, and Delphes3.1.2 [193] for the detector simulation. To include new physics effects, we use the same tool chain and a FeynRules [280] implementation of the dimension-six operators. We normalize the total event numbers to the SM predictions provided by the experimental collaborations to include detector effects as well as higher-order corrections and assume the same scaling of those effects for new physics contributions. This treatment is obviously justified for total rate measurements using the bulk of the phase space. For kinematic distributions, however, this is less clear, so we have checked that our approach is approximately correct [104, 241–245, 281]. Where available, higher-order corrections should eventually be included, see for instance Ref. [282] for QCD and EW corrections to kinematic distributions in di-boson production. Modifications of the Higgs branching ratios including dimension-six effects are calculated using the extended version of Hdecay [283].

As usual for our SFitter analyses, we include the interference with the SM amplitude as well as the squared dimension-six term in the calculation of modifications of the production amplitude. Dimension-six squared terms are expected to be small, but can become relevant whenever the interference with the Standard Model is suppressed. We neglect diagrams with more than one insertion of a dimension-six operators which could in principle interfere with the SM with the same suppression factor $1/\Lambda^2$ as the dimension-six squared terms. Finally, in our study of electroweak precision observables we neglect dimension-six squared contributions of the fermionic operators, since they will be strongly suppressed following Eq.(2.33) with a typical energy scale m_V. Along the same lines, we neglect effects

production	decay	ATLAS	CMS
	$h \to WW$	[259, 260]	[261–263]
	$h \to ZZ$	[260, 264]	[262, 263, 265, 266]
	$h \to \gamma\gamma$	[267]	[268]
	$h \to \tau\tau$	[260]	[262, 263, 269]
	$h \to Z\gamma$	[270]	[271]
WBF	$h \to$ inv		[272]
WBF	$h \to \tau\tau$		[269]
Vh	$h \to b\bar{b}$	[273]	[274]
Vh	$h \to \tau\tau$		[275]
Vh	$h \to$ inv	[174]	[276]
Vh	$h \to b\bar{b}$ (m_{Vh})	[277]	
$t\bar{t}h$	$h \to \gamma\gamma$	[256]	[268]
$t\bar{t}h$	$h \to ZZ \to 4\ell$	[256]	[265, 266]
$t\bar{t}h$	$h \to WW, ZZ, \tau\tau$	[260]	[262, 263]
$t\bar{t}h$	$h \to b\bar{b}$	[278]	[279]

Table 5.1: List of Run II Higgs measurements included in our analysis. For the m_{Vh} distribution our highest-momentum bin with observed events starts at $m_{Vh} = 990$ GeV and 1.2 TeV for the 0ℓ and 1ℓ final states.

of the fermionic operators on the decays of gauge bosons coming from Higgs decays. Assuming an approximately on-shell Higgs in our analyses, the hierarchy of scales combined with the well-defined external energy scale $E \lesssim m_h$ will render them numerically irrelevant.

Regarding the experimental input data, our analysis is based on the set of Run I measurements discussed in Refs [63, 64, 96]. In addition, we include the Run II Higgs measurements shown in Tab. 5.1 and the Run II di-boson measurements shown in Tab. 5.2. For dimension-six operators introducing new Lorentz structures and hence predicting modified event kinematics with respect to the Standard Model, the inclusion kinematic distributions provides powerful constraints, see also Section 2.5. This is particularly relevant for dimension-six operators which induce additional momentum dependences in the vertices. Momentum-related kinematic distributions such as a m_{Vh} distribution from an ATLAS resonance search [277] therefore provide especially powerful constraints. In case of the ATLAS distribution, we include the results of the zero-lepton and one-lepton final states and re-bin the reported result such that the most relevant high bins include a statistically meaningful number of events, giving us measurements exceeding $m_{Vh} = 1$ TeV. For decays of the Higgs boson such as $H \to 4\ell$ kinematic effects can be safely neglected in a global analysis. The on-shell condition limits the momentum flow through the Higgs decay vertex and any kinematic measurement of Vh or WBF production (which is influenced by the same dimension-six operators) will surpass their impact on a global analysis [284]. The fermionic Higgs-gauge operators in Eq. (5.2) are already highly constrained by electroweak precision data [110, 111]. In addition to the LHC measurements already discussed, we include the set of Z-pole and W properties given in Eq. (2.31) and Eq. (2.32).

We combine our data sets of LHC data and electroweak precision data, constructing a multi-dimensional, full exclusive likelihood map as discussed in Chapter 3. As we aim at describing small deviations from the Standard Model, a key assumption to be able to use an effective field theory framework, we can safely assume that local SM-like minima are also the global minima of our likelihood map, as we will further discuss later in this section. For the minimization of the constructed likelihood function, we have described multiple approaches in Section 3.2. Here, we will use the toy Monte Carlo method of Section 3.3. We generate 10.000 toy measurements, modeling the Poissonian, Gaussian or flat input distributions and taking into account correlations of systematic uncertainties. For each of the shifted measurements we determine the best-fitting point in the space of Wilson coefficients using Minuit. We then create one-dimensional histograms of the obtained best-fit points, effectively profile over the remaining parameters, and determine the 68% and 95% ranges around the SM-like central value. For the error bands we require the log-likelihood values at the lower and upper ends to be identical. We compare the limit setting procedure using toy Monte Carlos with a Markov Chain Monte Carlo fit. See Section 3.2.3 for details on the Markov Chain Monte Carlo approach. As it is hard to define a universal and efficient proposal function for a parameter space which behave quite differently in different directions, the Markov Chain Monte Carlo likelihood scan for our up to 19-dimensional parameter space becomes inefficient and computationally almost intractable. However, we find encouraging agreement of the limits obtained with both approaches for lower-dimensional fits.

Our toy Monte Carlo approach lets us define the 68% and 95% ranges around the SM-like central value without having to rely on the assumption of a Gaussian behavior. We can, however, compare our limit setting procedure with limits obtained by fitting a dual Gaussian to the 1D-histogram of the best-fit values of our toy Monte Carlo events, i.e. we define a function consisting of two Gaussians with the same central value, but different widths for the lower and upper half of our function. For all Wilson coefficients we find a good agreement of both limit setting procedures, see Fig. 5.4, even though for example the profile likelihood for f_W does not have a symmetric Gaussian shape. The shape for the invisible Higgs width is obviously distorted, since we do not allow for negative branching ratios. We make use of the Gaussian fit for the predictions of the best-fit points of the Wilson coefficients and quote the results of the non-Gaussian analysis for the 68% and 95% confidence regions. For additional details on the SFitter framework we refer to Refs. [54, 237, 238].

It is often argued that in analyses based on effective Lagrangians the dominance of the dimension-six squared contributions over the interferences of the dimension-six terms with the SM signal the breakdown of the expansion in $1/\Lambda$. However, there exist many physics reasons for the squared contributions to be larger than the interference terms [290], for instance when the diagrams including

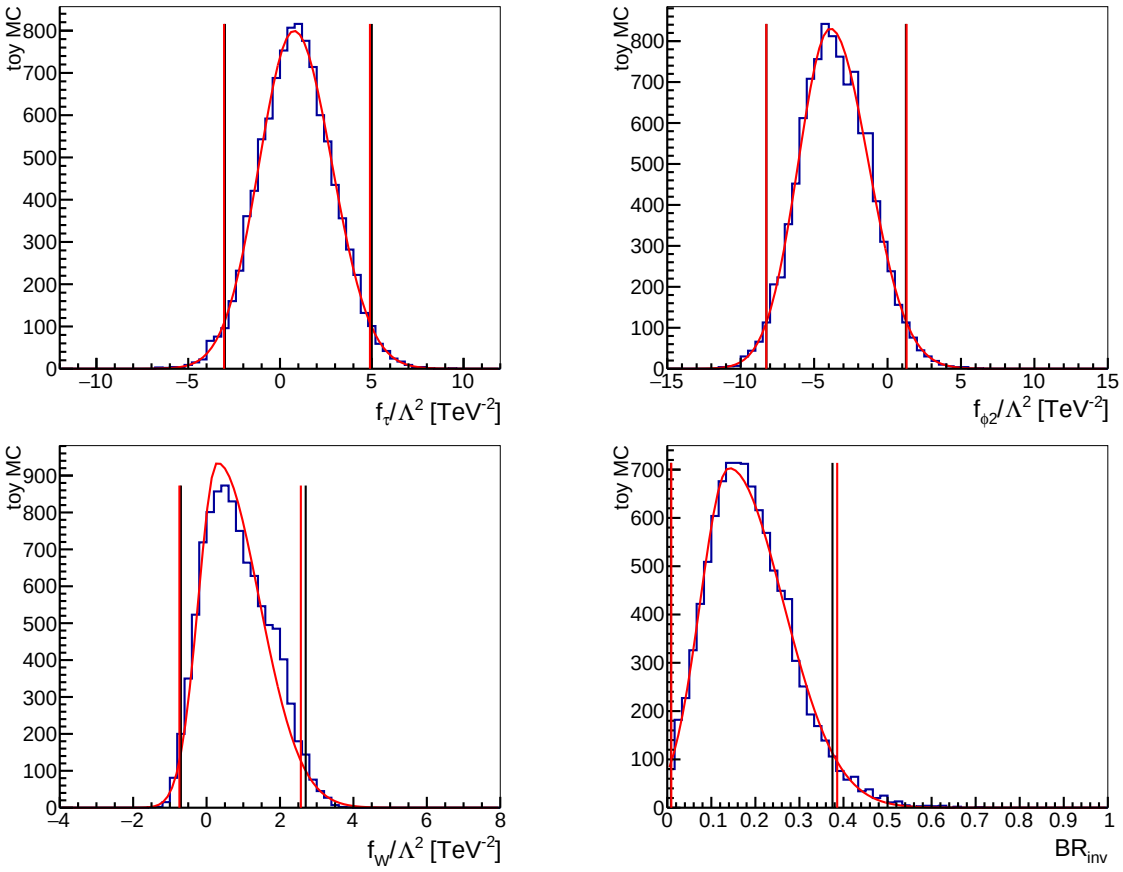

Figure 5.4: Distributions of the toy experiments for the operators $\mathcal{O}_\tau$, $\mathcal{O}_{\phi 2}$ and $\mathcal{O}_W$ as well as the invisible Higgs branching ratio, based on the full LHC data set. The lines show the 95% CL limits from the histogram (black) and the double-Gaussian fit (red). Figure taken from Ref. [3].

dimension-six contributions are incapable of interfering with the SM diagrams. Therefore, comparing the seize of the effects of dimension-eight operators with those of dimension-six can give useful hints about the validity of the truncation [291], but it does not have to. In practice, when we consider the dimension-six Lagrangians of Eqs. (5.1) and (5.2) as a low-energy approximation of a UV-complete theory, we simply need to ensure that none of its new particles contributes as a propagating degree of freedom on its mass shell [77, 292].

Since we aim at using the effective field theory framework to describe small deviation from the SM, we

	channel	distribution	#bins	max [GeV]	
8 TeV	$WW \to \ell^+\ell'^- + \not{E}_T$ $(0j)$	leading $p_{T,\ell}$	4	350	20.3 fb^{-1} [285]
	$WW \to \ell^+\ell^{(\prime)-} + \not{E}_T$ $(0j)$	$m_{\ell\ell^{(\prime)}}$	7	575	19.4 fb^{-1} [286]
	$WZ \to \ell^+\ell^-\ell^{(\prime)\pm}$	m_T^{WZ}	6	450	20.3 fb^{-1} [287]
	$WZ \to \ell^+\ell^-\ell^{(\prime)\pm} + \not{E}_T$	$p_T^{Z\to\ell\ell}$	8	350	19.6 fb^{-1} [288]
13 TeV	$WZ \to \ell^+\ell^-\ell^{(\prime)\pm}$	m_T^{WZ}	7	675	36.1 fb^{-1} [289]

Table 5.2: List of Run I and Run II di-boson measurements included in our analysis. The maximum value in GeV indicates the lower end of the highest-momentum bin we consider.

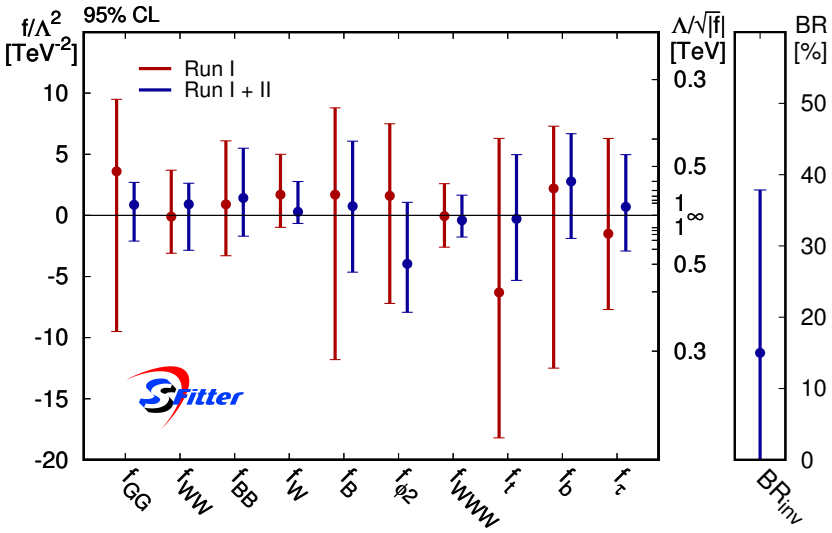

Figure 5.5: Allowed 95% CL ranges for individual Wilson coefficients f_x/Λ^2 from a one-dimensional profile likelihood. We show results from Run I (red) and using the additional Run II measurements (blue). We neglect all operators contributing to electroweak precision observables at tree level. Figure taken from Ref. [3].

will not take into account secondary solutions which appear, for instance, because of switched signs of Yukawa couplings. We expect those effects to be best tested in direct LHC searches rather than a global analysis, because they only require scales $\Lambda \sim m_h$, assuming weakly interacting new physics. As an example, the sign of the top Yukawa coupling, or rather the relative sign of the top Yukawa coupling and the sign of the Higgs coupling to W bosons, can be probed in the decay of the Higgs to a pair of photons or in $th(q)$ production, because of the interference of two diagrams with $t\bar{t}h$ and WWh couplings. An observation as striking as the one of a sign switch in a Yukawa coupling would signal a breakdown of the renormalizable Standard Model in its current form and would prompt us to modify our SMEFT hypothesis. Direct and indirect searches are of course closely linked when we look for new physics effects in kinematic distributions. For instance, the appearance of a shoulder in an invariant mass distribution could be an early sign of a mass peak in data [77, 292].

5.5 Global Higgs-gauge analysis in the SMEFT framework

We will now present our global analysis of the Higgs and electroweak gauge sector including LHC Run II data. To disentangle the effects of the inclusion of the new LHC Run II data and the inclusion of the additional set of (mostly) fermionic operators in Eq. (5.2) with respect to previous analyses in Refs. [63, 64, 96], we first perform a fit of the operators in Eq. (5.1) using LHC data only. Before we present the results of the fit, let us discuss our anticipation of the effects of the new Run II data. Not only do we expect the available 13 TeV data given in Tabs. 5.1 and 5.2 to generate a generic improvement in many of the standard measurements, we also anticipate a strong impact from three types of analyses in particular: the measurements of Higgs production in association with a top quark pair, the significant observation of (third family) fermionic Higgs decays, and the inclusion of the re-casted m_{Vh} distribution to very large energies. With respect to Run I, we expect the wealth of available $t\bar{t}h$ analyses at 13 TeV to help unwind the correlations between the operators contributing to the gluon fusion production process, i.e. $\mathcal{O}_{u\phi,33}$ influencing $ht\bar{t}$ couplings and $\mathcal{O}_{GG}$ which induces a tree-level hgg vertex.

In Fig. 5.5, we display the 95% CL limits on the Wilson coefficients of the included dimension-six operators taking into account LHC Run I and Run II data. The right axis indicates the new-physics scale Λ assuming reasonably strongly interacting new physics $f_x = 1$. Indeed, the limits limits on f_t,

f_b and f_τ have improved by more than a factor of two with respect to the Run I measurements only. As already discussed, the measurement of the top Yukawa in $t\bar{t}h$ measurements allows to disentangle the effects of f_t and the Higgs coupling to gluons due to $\mathcal{O}_{GG}$ which can only be extracted after we subtract the measured top loop contribution. The operators $\mathcal{O}_{\phi 2}$ and $\mathcal{O}_{d\phi,33}$ are highly correlated in a global analysis due to their strong influence in the total Higgs width. Modification of the Higgs width are induced by $\mathcal{O}_{\phi 2}$ due to its renormalization of the Higgs wave function, see Eq. (2.21), or by $\mathcal{O}_{d\phi,33}$ which affects the largest contribution to the Higgs width $h \to b\bar{b}$, compare Fig. 2.2. After Run II, their limits have significantly improved and both of them also show symmetric Gaussian log-likelihood distributions. The slight deviation of the central value from the SM expectation is due to both Run II ATLAS and CMS measurements of the $pp \to Vh$, $h \to b\bar{b}$ finding a signal strength of $\mu \sim 1.2$ [273, 274]. The improvement in the limits on f_W and f_B reflect the importance of testing the momentum-dependent operators in distributions, specifically distributions of associated Vh production for the corresponding operators $\mathcal{O}_W$ and $\mathcal{O}_B$. Comparing the distribution of the toy MC events for f_W in Fig. 5.4, we see that the limits are by no means symmetric and Gaussian, signaling the relative importance of the quadratic terms of the EFT expansion. The limits on the operators $\mathcal{O}_{WW}$ and $\mathcal{O}_{BB}$ show the least improvement with respect to Run I limits. This is due to the lack of high-impact kinematic WBF measurements in the Run II data set. Similarly, the limits on the operator $\mathcal{O}_{WWW}$ which only contributes to (anomalous) triple gauge couplings and is constrained by the di-boson production measurements listed in Tab. 5.2, are still dominated by the kinematic measurements at Run I. We expect the limits to improve once Run II WW measurements are available and will help to disentangle correlations between the bosonic operators.

Finally, we find a global limit on the Higgs branching ratio to invisible particles of

$$\mathrm{BR}_{\mathrm{inv}} < 38\% \qquad \text{at } 95\% \text{ CL.} \tag{5.9}$$

The best-fit point is given by $\mathrm{BR}_{\mathrm{inv}} = 14\%$. Our limit is significantly weaker than the limit of $\mathrm{BR}_{\mathrm{inv}} < 24\%$ quoted for instance by CMS [272] for a combination of the 13 TeV invisible Higgs searches in the most sensitive search channels. The stronger bound in the CMS analysis is due to the assumption of SM-like Higgs production modes in the CMS limit setting which is lifted in our global analysis. Indeed, there is a strong correlation between the invisible Higgs branching ratio and the Wilson coefficient of $\mathcal{O}_{\phi 2}$ which can be explained by their strong influence on the Higgs width. To compare with the CMS result, we fix $f_{\phi 2} = 0$ and obtain a limit of $\mathrm{BR}_{\mathrm{inv}} < 26\%$ which is in agreement with the experimental results. Altogether, the general reach of LHC Run II for the considered dimension-six operators $\Lambda/\sqrt{f}$ is between 400 GeV and 800 GeV if we consider Higgs and di-boson measurements alone.

Up until now, we have focussed on the effects of the new Run II measurements on the limits of the dimension-six operators listed in Eq. (5.1). We now want to go a step further and discuss the limits of a global analysis including also the operators in Eq. (5.2) and the constraints arising from electroweak precision observables, Eqs. (2.31) and (2.32). This is motivated by the large improvement of the limits on $\mathcal{O}_B$, an operator which is correlated with the fermionic operators in Eq. (5.2) due to their contribution to the Vh production process, see Fig 5.7. Comparing the typical limits on fermionic operators, Eq. (2.33), with the limits on $\mathcal{O}_B$, it seems counter-intuitive from a scale separation point of view that $\mathcal{O}_{\phi u}^{(1)}$ or $\mathcal{O}_{\phi Q}^{(3)}$ should have any effect on the LHC analysis [104, 241–245]. The ratio $\Lambda/\sqrt{f}$ is around one order of magnitude more strongly constrained for $\mathcal{O}_{\phi u}^{(1)}$ or $\mathcal{O}_{\phi Q}^{(3)}$ than for $\mathcal{O}_W$ and much more strongly for all other operators shown in Fig. 5.5. However, in Fig. 5.6 we see how the fermionic operator $\mathcal{O}_{\phi u}^{(1)}$ can affect Zh production in a very similar way as the bosonic operator $\mathcal{O}_B$ for a Wilson coefficient smaller by around a factor 1/50. This mainly reflects the fact that the fermionic operator contributes not only via the 3-point qqZ, but also through the 4-point $qqHZ$ vertices which are dominant at high energies [293]. The bosonic operators, on the other hand side, require the same s-channel Z-propagator we see in the Standard Model. We display the corresponding Feynman diagrams in Fig. 5.7 and infer the scalings for the diagrams including fermionic operators

$$\frac{g f_{\phi Q}\, v^2}{\Lambda^2} \quad (qqZ) \qquad \text{versus} \qquad \frac{g f_{\phi Q}\, v}{\Lambda^2} \quad (qqZh). \tag{5.10}$$

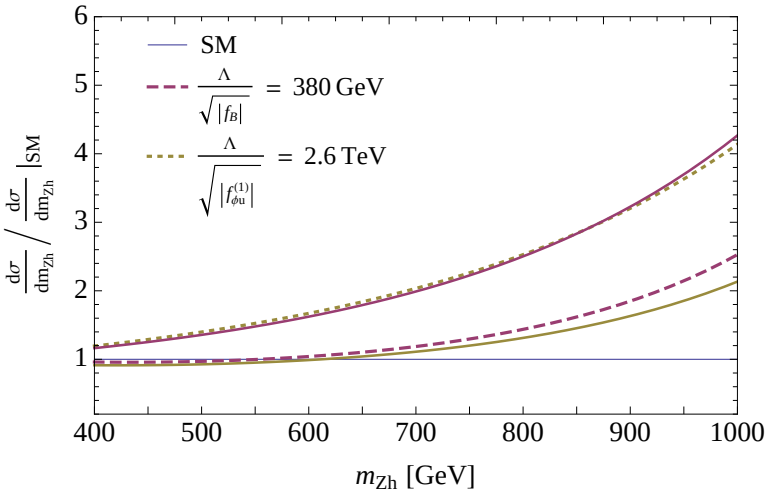

Figure 5.6: Invariant mass distribution m_{Zh} normalized to the Standard Model. The dashed lines correspond to $\Lambda/\sqrt{|f_B|} = 380$ GeV and $\Lambda/\sqrt{|f_{\phi u}^{(1)}|} = 2.6$ TeV with $f_x > 0$, while the solid lines correspond to the negative values of the Wilson coefficients with the same magnitude. Figure taken from Ref. [3].

This energy scaling explains the dominance of the 4-point interaction for the m_{Zh} distribution shown in Fig. 5.6. We have explicitly checked that for the fermionic operator it is dominated by the 4-point interaction, even though the 3-point interaction does interfere with the Standard Model. Eventually, the energy scaling in Eq. (5.10) will lead to unitarity violation [104].

The contribution of two operators with an apparently very different new physics scale to the m_{Zh} distribution at around the same rate can further be understood by the definitions of the operators: The definition of $\mathcal{O}_B$, Eq. (2.9), adds two powers of the coupling g' to a 3-point vertex. On the other hand, the 4-point contribution from $\mathcal{O}_{\phi u}^{(1)}$ lacks this second power of the coupling. With the dominance of the dimension-six-squared contribution over most of the parameter range shown in Fig. 5.6, we end up with a mis-match of four powers of the coupling from the definitions of the Wilson coefficients.

To further illustrate the interplay of the fermionic operators in the Lagrangian of Eq. (5.2) with the bosonic ones in Eq. (5.1), we display the correlation between these operators in Fig. 5.8 for our global analysis. Zh production leads to a clear correlation between f_B and $f_{\phi u}^{(1)}$, while Wh production is correlating f_W and $f_{\phi Q}^{(3)}$. Comparing the displayed parameter ranges, we find that the correlation relates very different values of the new physics scales for the fermionic and bosonic operators. In the lower panels of Fig. 5.8, we show the correlations of the bosonic operators f_B and f_W in a global fit before (left) and after (right) the inclusion of the fermionic operators and the constraints from electroweak precision data. The profiling over fermionic Wilson coefficients re-induces a correlation between f_B and f_W and weakens their limits.

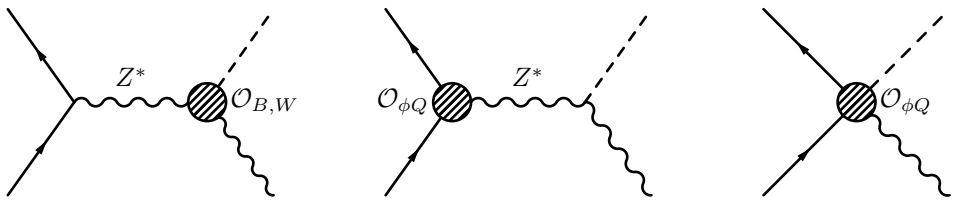

Figure 5.7: Dimension-six contribution to Zh production. We show sample diagrams for the usual bosonic corrections, the small fermionic corrections from a 3-point vertex, and the large fermionic corrections from a 4-point interaction.

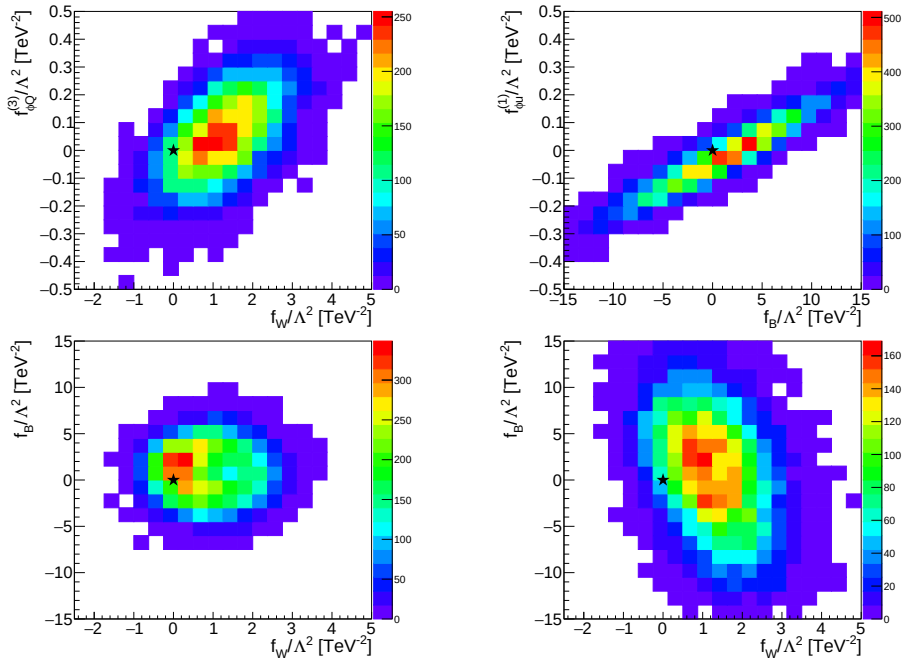

Figure 5.8: Correlations between the fermionic and bosonic operators (top row), and between the usual bosonic operators (bottom row). For the latter we show the purely LHC results (left) and the results after including the additional fermionic operators. Figure taken from Ref. [3].

The above discussion clearly highlights the importance of including the additional operators shown in Eq. (5.2) in a global fit at the level of precision reached in LHC Run II analyses [66, 103, 104, 241–245]. This is a result of the relative enhancement of the fermionic Higgs-gauge operators through their 4-point interactions. In Fig. 5.9, we show the limits of a global analysis on all considered dimension-six operators in Eq. (5.1) and (5.2), both at the 68% and 95% confidence levels. As our input data set, we consider all LHC measurements considered for Fig. 5.5 and in addition include electroweak precision observables. We quote the limits on the the triple-gluon operator $\mathcal{O}_G$ and the chromo-magnetic operator $\mathcal{O}_{tG}$ in Fig. 5.9, even though they are not included in our global fit. While these operators are in principle capable of influencing a global Higgs analysis, we have shown in Section 5.3 that they are strongly constrained by dedicated studies. Given the level of precision of those studies, their effects on the Higgs observables will not be visible in a global fit and they are effectively rendered irrelevant for analyses of the Higgs sector.

From the scaling of the 68% and 95% confidence limits, Fig. 5.9, we can deduce that they have a Gaussian behavior. If we compare the results for the bosonic operators with the limits in Fig. 5.8 for the global fit without the fermionic operators, we find that results on f_B are roughly a factor of two weaker once we profile over the fermionic Wilson coefficients. Comparing the limits on the fermionic Higgs-gauge operators with the constraints for the bosonic operators from our global analysis, we find that limits on fermionic operators are typically a factor 10 to 100 stronger. Finally, let us make the point that the interplay of the operators and data sets relevant for Higgs physics and electroweak precision observables is not a one-way street. Not only does the inclusion of the fermionic operators and electroweak precision observables influence the constraints on operators relevant for the Higgs sector, the operators of the Lagrangian in Eq. (5.2) also obtain meaningful constraints from LHC Higgs physics. To illustrate this behavior, in Fig. 5.10 we show the limits on the operators contributing to electroweak precision measurements with and without LHC Run II measurements as an input data set. Including LHC Run II measurements significantly improves the limits on operators which are relatively poorly probed by electroweak precision observables alone, such as $f_{\phi Q}^{(3)}$, $f_{\phi u}^{(1)}$ and, in particular, $f_{\phi d}^{(1)}$. The limits on other Wilson coefficients are not significantly improved, but shifted towards zero, i.e. symmetrized. All in all our finding highlight the importance of a global analysis covering Higgs and

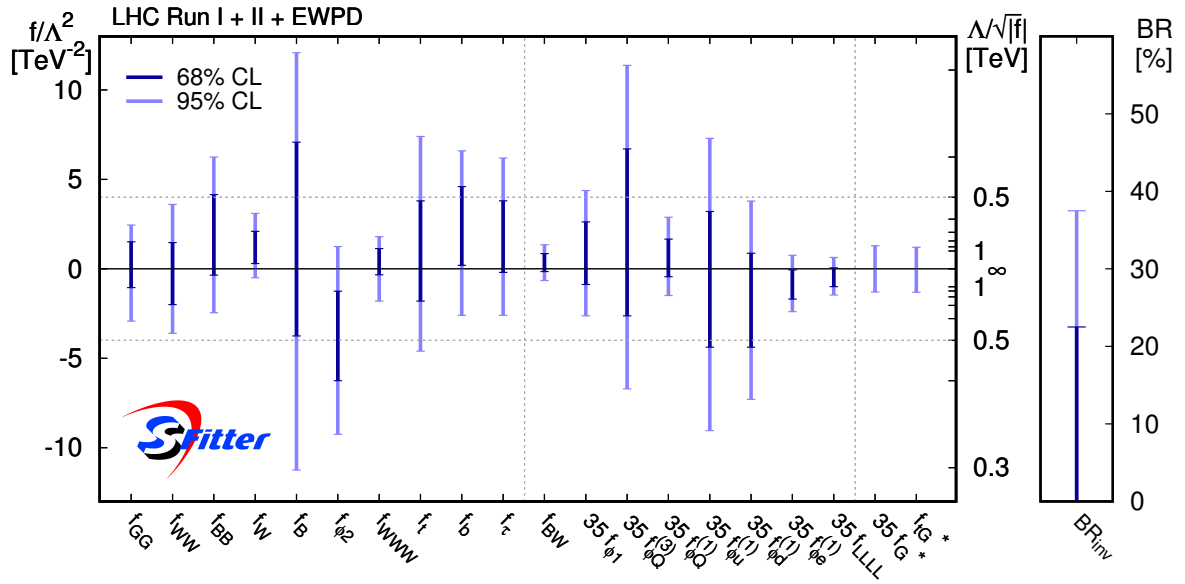

Figure 5.9: Allowed 68% and 95% CL ranges for individual Wilson coefficients f_x/Λ^2 from a one-dimensional profile likelihood. All results include the Run II measurements combined with electroweak precision data. We quote the best results for $\mathcal{O}_G$ [219] and $\mathcal{O}_{tG}$ [220] from non-Higgs analyses. Figure taken from Ref. [3].

di-boson observables at the LHC as well as electroweak precision data.

5.6 Conclusion and outlook

We have presented a global analysis of the LHC Run I and Run II data covering Higgs and di-boson measurements in the SMEFT framework to dimension six, including a total of 18 bosonic and fermionic operators and invisible decays of the Higgs boson through their branching ratio. In doing so, we have moved a significant step closer towards performing a global SMEFT fit for a precision analysis of LHC data. We have seen that the increased LHC sensitivity for Run II, especially to the anomalous gauge boson couplings to quarks, requires the inclusion of fermionic operators in a global fit and therefore demands a combination of LHC data with electroweak precision observables. In addition to the 18 operators included in our fit, we have discussed the limits on the operators $\mathcal{O}_G$ and $\mathcal{O}_{tG}$ which we find to be more strongly constrained by multi-jet production and $t\bar{t}$ production, respectively.

In our fit using the SFitter framework we do not only include ATLAS and CMS results in terms of pre-defined pseudo-observables, but we make use of raw event numbers and include their correlations for systematic and theoretical uncertainties whenever possible. In addition, we exploit kinematic distributions up to TeV energies for Vh production and di-boson production. For a fit of bosonic and Higgs-fermion operators only, all limits on dimension-six operators are consistently improved by adding the Run II data to the existing Run I dataset. Specifically, we see a large improvement of the limits in the Yukawa sector which stems from the large abundance of $t\bar{t}h$ measurements available for Run II and the significant observation of fermionic Higgs decays. Moreover, a kinematic measurement of Vh production significantly improves the limits on the operators $\mathcal{O}_W$ and $\mathcal{O}_B$. The typical Run II limits at 95% CL range around $\Lambda/\sqrt{f} = 400 \ldots 800$ GeV. In spite of being strongly constrained by electroweak precision data, fermionic Higgs-gauge operators have a non-negligible impact on Higgs and di-boson production. Their effect on our global fits highlights the relevance of the LHC for the precision study of couplings of weak bosons to quarks: For associated Higgs production, the effect of fermionic Higgs-gauge operators is enhanced through 4-point vertices, inducing strong correlations with $f_{B,W}$. The inclusion of and profiling over fermionic Higgs-gauge operators weakens the limits on

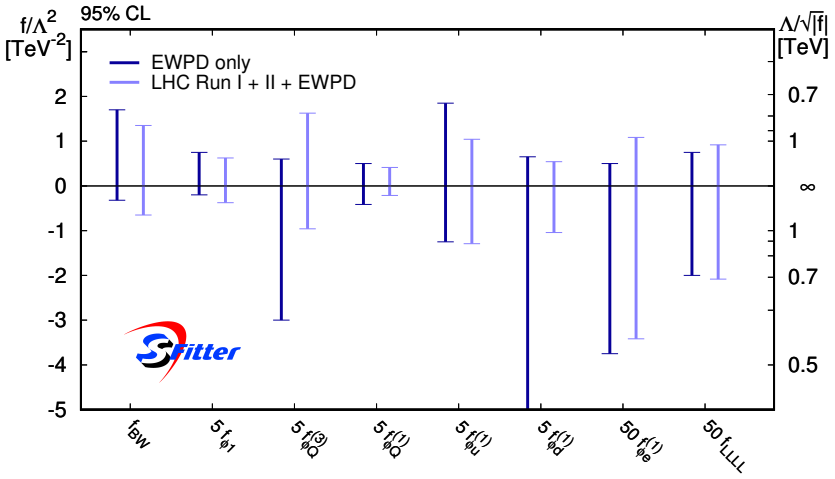

Figure 5.10: Allowed 95% CL ranges for the individual Wilson coefficients f_x/Λ^2 constrained in electroweak precision data, see Eq. (5.2), from a one-dimensional profile likelihood. We compare fits using only electroweak precision data as inputs with a combined fit including LHC Run I and Run II measurements.

f_B by a factor two. At the same time, LHC measurements of the couplings of weak bosons to fermions have already reached a similar or exceeding level of precision compared to electroweak precision data at LEP. As an example, the limits on $f_{\phi d}^{(1)}$ are highly improved by the inclusion of LHC data with respect to a fit of electroweak precision data only. In a global fit of all 18 operators considered in this analysis, bosonic operators typically probe a range $\Lambda/\sqrt{f}$ up to the TeV scale, while the fermionic Higgs-gauge operators are consistently constrained to 5 ... 10 TeV.

In summary, LHC Run II data significantly improve the existing limits on dimension-six operators in the SMEFT framework, in particular for Higgs-fermion and Higgs-gluon operators. These limits on Higgs couplings in the SMEFT framework can be mapped onto constraints for UV-complete BSM models [65, 66]. Moreover, they provide a crucial ingredient for future tests of the global structure of the Higgs potential [2, 11, 12]. Fermionic Higgs-gauge operators have proven to be relevant in global fits of LHC Higgs data and motivate the future combination of data from the Higgs and electroweak sectors with results from the top sector.

6 | A Global View on the Higgs-Gauge Sector at 27 TeV

In Chapter 5, we have performed a global analysis of the Higgs-gauge sector based on LHC Run II data in the SM effective field theory framework. For the next generation of colliders, a high-energy upgrade of the LHC (HE-LHC) with a center of mass energy of 27 TeV is currently under debate. To examine its reach for the Higgs sector and compare it to the sensitivity of other potential future colliders, we now want to turn to the question, how we could further improve the constraints on Higgs couplings at a 27 TeV upgrade of the LHC. We will present our results both in terms of Higgs coupling modifiers in the Δ-framework and in terms of a gauge-invariant effective Lagrangian, including invisible Higgs decays. For the latter, we will focus specifically on di-Higgs production as an additional measurement in our input data set which allows for a meaningful test of the Higgs self-coupling in a global analysis.

The following chapter is based on work in collaboration with Dorival Gonçalves, Tilman Plehn, Michihisa Takeuchi, Dirk Zerwas and, in the early stages, also Michael Rauch [2]. Most of the figures and tables as well as a significant part of the text are taken from the corresponding publication. The credit for the extrapolation of the LHC Run I rate measurements to 27 TeV is entirely entitled to Michael Rauch.

6.1 Introduction

The systematic and comprehensive study of the Higgs boson and its properties is one of the focusses of LHC physics [67]. In Chapter 5, we have examined the current status of LHC Run II measurements for a global study of Higgs couplings in the SM effective field theory framework. While LHC Run II analyses already set limits on a new physics scale Λ to the level of $\Lambda/\sqrt{f} = 400 \ldots 800$ GeV at 95% CL, they still leave room for new physics in the Higgs sector. A thorough analyses of the Higgs potential is left as a crucial task for next generation colliders. There exist several proposals for colliders apt for Higgs precision measurements beyond the LHC. Lepton colliders like the FCC-ee or the ILC as well as hadron colliders such as FCC-hh and a 27 TeV high-energy upgrade of the LHC and their reach for Higgs physics have already been discussed in the literature [12, 294–296]. We focus on one of those future colliders here, the HE-LHC, and discuss the question what level of precision for global Higgs analyses we can reach at a 27 TeV hadron collider with an attobarn-level integrated luminosity. Its high energy and large luminosity could extend current limits on Higgs couplings not only through precise measurements of single-Higgs production, but also by generating a statistically meaningful number of di-Higgs production events.

Our global study of the Higgs-gauge sector at the HE-LHC is based on the established SFitter analysis of the LHC Run I results [63, 64] and extrapolated to 27 TeV. We include measurements of invisible Higgs decays in terms of an invisible branching ratio using an in-house extrapolation of the analysis presented in Chapter 4. Finally, while in the global analysis of 13 TeV LHC data in Chapter 5 we could safely neglect the Higgs self-coupling given the precision of the data [297], at a 27 TeV hadron collider we expect measurements of Higgs pair production with statistically relevant event numbers [13, 247, 298, 299]. We will therefore include a kinematic distribution of di-Higgs production based on Ref. [13] in our global analysis.

We will discuss the 27 TeV projections for Higgs-coupling constraints in two frameworks: First, we analyze the reach of an upgraded LHC in terms of modified couplings of the SM Higgs boson in the Δ-framework, described by an effective Lagrangian with a non-linear realization of electroweak symmetry breaking in Sec. 6.2. We then interpret the results in terms of an effective Lagrangian based on the SMEFT framework in Sec. 6.3 which allows us to include kinematic distributions and to combine the global Higgs analysis with di-boson data. As a 27 TeV upgrade of the LHC would for the first time provide a meaningful measurement of di-Higgs production, we discuss the reach of such a collider for setting limits on a modification of the Higgs potential using differential measurements of di-Higgs production in Sec. 6.4.

There are strong analogies between the effective field theory analysis for a 27 TeV collider performed in Section 6.3 and the global analysis of LHC results, Chapter 5. Previously, we have compared the reach of LHC Run II results at 13 TeV with the limits of a fit of LHC Run I data at 8 TeV. In doing so, we have gained relevant insights on how an increase of the collider energy will tighten the constraints on dimension-six operators of an effective field theory. This will aid in identifying the potential of a global fit at an energy of 27 TeV. Our LHC Run II analysis profited from an energy increment in two ways: First, the increased energy allowed to test previously inaccessible processes and thereby disentangle correlations between operators contributing to the same experimental signatures. For the first time, an energy increase to 13 TeV allowed to observe Higgs production in association with a top quark pair [256, 300, 301], resulting in the first direct measurement of the top Yukawa coupling independent of the effective Higgs coupling to gluons. As a consequence, the limits on the dimension-six operators resulting in $ht\bar{t}$ and hgg couplings were significantly improved. Second, tighter limits on dimension-six operators inducing momentum-dependent couplings were obtained by studying kinematic distributions up to high energies. For our 13 TeV fit, the study of the invariant mass m_{Vh} distribution for Higgs production in association with a vector boson resulted in strong constraints on operators contributing to momentum-dependent hVV couplings and even improved the limits on fermionic Higgs-gauge operators modifying the quark couplings to vector bosons beyond the level of constraints from electroweak precision data. Consequently, for our study of a 27 TeV hadron collider in terms of an effective field theory description, we will focus on the inclusion of di-Higgs production in our input data set as an example of a previously inaccessible process and the inclusion of (momentum-related) kinematic distributions.

As an extrapolation from established and validated 8 TeV results, the limits presented in this brief study provide a reliable first estimate of the reach of an energy upgraded LHC with a large integrated luminosity. We neglect the effects of fermionic Higgs-gauge operators which should eventually be included in this analysis and combined with electroweak precision data [3,66,235,242,244,302]. Aiming towards a global fit including fermionic Higgs-gauge operators is not only motivated by their effect on the bosonic operators included in this study, we also expect a 27 TeV collider to significantly improve the existing limits on this additional set of operators. We leave a more detailed analysis also including a larger set of kinematic distributions [303] for future work. Regarding uncertainties, we will see that a conservative treatment is in order, because global Higgs analyses at a 27 TeV collider will rapidly enter systematics-limited and theory-limited territory, especially when they are based on rate measurements only.

6.2 Global Higgs analysis in terms of coupling modifiers

As discussed in Section 2.6, a model-independent and reproducible way to describe new physics effects on the Higgs sector is a parametrization of the deviations of the Higgs couplings g_x from their SM values $g_x^{\rm SM}$ by coupling modifiers

$$\begin{aligned} g_x &= g_x^{\rm SM}\,(1+\Delta_x) \\ g_{g,\gamma} &= g_{g,\gamma}^{\rm SM}\,(1+\Delta_{g,\gamma}^{\rm SM}+\Delta_{g,\gamma}) \equiv g_{g,\gamma}^{\rm SM}\,(1+\Delta_{g,\gamma}^{\rm SM+NP})\,. \end{aligned} \tag{6.1}$$

For the loop-induced Higgs couplings to photons and gluons, we need to include both the implicit shift due to the modifications of the dimension-four W boson and the top quark couplings described by $\Delta_{g,\gamma}^{\rm SM}$

and a secondary deviation that may arise from new particles running in the loop by higher-dimensional operators $\Delta_{g,\gamma}$.
The coupling modifiers Δ_x can be directly translated into the experimentally used κ notation

$$\kappa_x = (1 + \Delta_x) \tag{6.2}$$

at least modulo the treatment of the tree-level couplings contributing to the loop-induced operators. The corresponding global Higgs analysis is the main reason why we can now claim that the observed Higgs boson closely follows the Standard Model predictions. The Lagrangian corresponding to the shifts of the SM couplings of the Higgs by Δ is given by [63]

$$\begin{aligned}\mathcal{L} = \mathcal{L}_{\text{SM}} &+ \Delta_W \; g m_W h \, W^\mu W_\mu + \Delta_Z \; \frac{g}{2c_W} m_Z h \, Z^\mu Z_\mu - \sum_{\tau,b,t} \Delta_f \; \frac{m_f}{v} h \left(\bar{f}_R f_L + \text{h.c.} \right) \\ &+ \Delta_g F_G \; \frac{h}{v} \, G_{\mu\nu} G^{\mu\nu} + \Delta_\gamma F_A \; \frac{h}{v} \, A_{\mu\nu} A^{\mu\nu} + \text{invisible decays} \, . \end{aligned} \tag{6.3}$$

The constants F_G and F_A normalize the respective Higgs couplings to gluons and photons to their SM values

$$F_G = -\frac{\alpha_s}{16\pi} \sum_f F_{1/2}(\tau_f) \, , \qquad F_A = -\frac{\alpha}{8\pi} \left[\sum_f N_{c,f} \, Q_f^2 \, F_{1/2}(\tau_f) + F_0(\tau_W) \right] \, . \tag{6.4}$$

Here, the functions $F_{1/2}$ and F_0 describe the fermion and W boson loops respectively and $\tau_x = 4m_x^2/m_h^2$. For the Higgs couplings to weak gauge bosons and fermions, we only include SM-like dimension-four terms which will shift the SM-like Higgs couplings and break electroweak gauge invariance. For invisible Higgs decays, we do not include a term on the Lagrangian level. Instead, what we indicate by the invisible decays in Eq. (6.3) is that we account for an invisible Higgs branching ratio in terms of an additional contribution to the Higgs width. We refer to the discussion below Eq. (5.2) for more details. We refrain from including a more complete set of operators with non-SM like Lorentz structures, in order to be consistent with existing experimental analyses in this framework. The Lagrangian in Eq. (6.3) can trivially be translated into an effective Lagrangian with a non-linear representation of the Higgs and Goldstone fields in the HEFT framework [109, 304–306].
As already mentioned in the introduction of this chapter, one of the milestones of the physics program of a 27 TeV collider is to obtain the first probe of the Higgs self-coupling by measuring di-Higgs production. In principle, it would be possible to include this study of the Higgs self-coupling in a global, non-linear Higgs analysis in the Δ-framework. However, two caveats arise: First, we know that a measurement of di-Higgs production will not improve the limits on any of the parameters given in Eq. (6.3), as those can be constrained more precisely by single-Higgs production. Second, the impact of a modification of the Higgs self-coupling on single-Higgs production is negligible in the sense that its inclusion will not have visible effects on the limits on the coupling modifiers. Probing the Higgs self-coupling crucially depends on the study of kinematic distributions [13,297] which the Δ-framework

production	[%]	decay	[%]
GF	10.2	WW	2.63
qqh	3.0	ZZ	2.63
Wh	3.2	$\gamma\gamma$	3.31
Zh	5.7	$b\bar{b}$	2.17
$t\bar{t}h$	12.8	$Z\gamma$	7.33
hh	18.	$\tau\tau$	2.78

Table 6.1: Relative theory uncertainties for the different Higgs production and decay channels contributing to the global analysis. The numbers correspond to those quoted in Ref. [76].

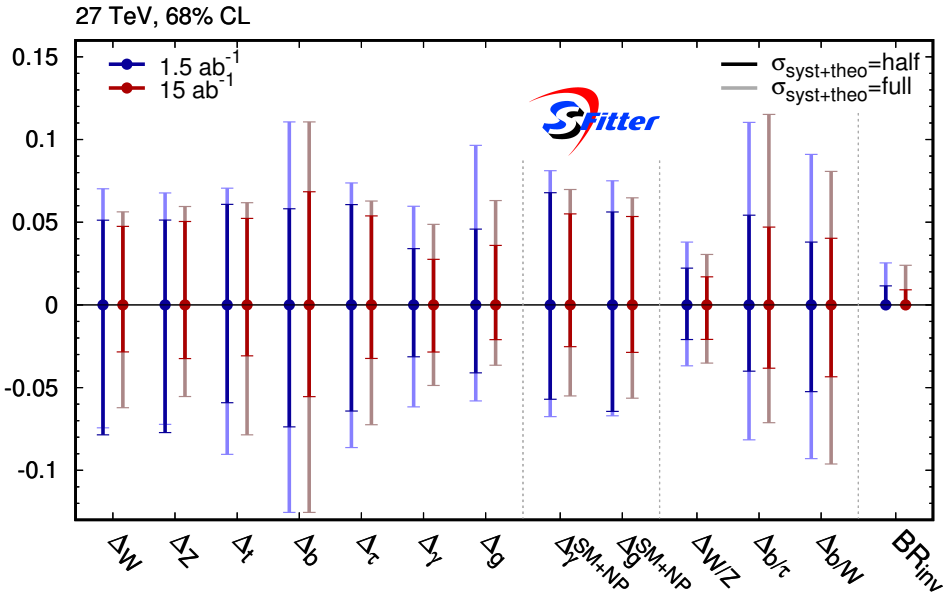

Figure 6.1: 68% CL limits on the coupling modifiers of Eq. (6.3) as a result of a global Higgs analysis with non-linearly realized electroweak symmetry breaking. All limits are shown as profiled over all other couplings. Figure taken from Ref. [2].

is completely insensitive to in our implementation. We therefore postpone this aspect to the global study within the effective field theory framework in Sec. 6.3, where we include a full set of di-boson and single- and di-Higgs distributions.

The input data set for our global Higgs analysis in the Δ-framework, is created by re-scaling the signal and background event numbers in the 8 TeV analyses included in SFitter [63] to 27 TeV, assuming two experiments. For invisible Higgs searches, we include an in-house extrapolation of the WBF analysis described in Chapter 4 to 27 TeV in our data set. We presume all 'measurements' to agree exactly with the SM predictions, i.e. the best-fit points of our parameters will always be their SM values. We do not include any kinematic distributions, since the analysis in terms of Eq. (6.3) only describes modifications of total cross sections in the Higgs sector.

For systematic uncertainties, we assume the same relative uncertainties and correlations as in the 8 TeV analyses. Statistical uncertainties are calculated from the signal and background event numbers assuming a Poisson distribution, taking into account that some backgrounds are measured in potentially larger control regions. The current theory uncertainties on the SM predictions of single and di-Higgs production as well as the considered branching ratios are listed in Tab. 6.1. As we assume flat theory uncertainties, we linearly add up different the uncertainties from different sources, including uncertainties on the parton distributions. For the latter, we make the assumption that dedicated fits will determine the PDFs at a 27 TeV collider will full luminosity at the same level as they are determined for the LHC now. Precision predictions for the Higgs observables and PDF extraction will be crucial at a 27 TeV collider which we illustrate by showing our results both with the current theory uncertainties as well as with halfed theory uncertainties and systematics.

In Fig. 6.1 we present the expected precision of the SM-like Higgs coupling measurements for a potential 27 TeV LHC upgrade in a global fit. Some of the couplings exhibit asymmetric upper and lower limits which arise due to correlations between different coupling modifier, but also reflect numerical uncertainties. We use different colors to compare two scenarios with different assumed integrated luminosities of 1.5 ab^{-1} and 15 ab^{-1} to illustrate the influence of the statistical uncertainties. For all coupling deviations, we find that the improvement of the limits with increased luminosity is much smaller than the rough factor three which one could expect from a scaling of the limits with the square-root of the luminosity. This behavior is an indication for those limits being limited by systematics and

theory uncertainties. In particular, ratios of couplings, like $\Delta_{W/Z}$, only see a fairly small improvement from an increased luminosity. To make the point that the insensitivity to an improved statistics is in fact due to systematics and theory uncertainties, we also compare today's theory and systematic uncertainties with an improvement to half the current uncertainties indicated by full and shaded bands. A reduction of theory uncertainties and systematics has a large impact on the limits of Δ_b and Δ_g, as well as for the coupling ratios. Generally, the typical precision a 27 TeV hadron collider can reach for measuring Higgs couplings is 3 ... 5%, when assuming the improved systematic and theoretical uncertainties. Ratios of couplings, such as the ratio of the W and Z couplings to the Higgs, can be constrained up to a factor two more precisely than the individual couplings due to a partial cancellation of the correlated uncertainties. The limit on the invisible Higgs branching ratio will be reduced to the level of 1 ... 2%. Comparing those numbers with the expected sensitivity of the high-luminosity LHC in Ref. [307], we find that a 27 TeV hadron collider with attobarn level integrated luminosity will double the precision on many of the Higgs coupling modifications.

6.3 Global Higgs-gauge analysis in the SMEFT framework

The global analysis in the Δ–framework does not allow for the inclusion of kinematic effects. To examine the impact of new Lorentz structures in our analysis, we will now perform a global fit of the Higgs-gauge sector in the SM effective field theory framework up to dimension-six. As discussed in detail in Chapter 2, Standard Model effective field theory provides a framework to interpret the LHC results in terms of an effective Lagrangian with linearly realized electroweak symmetry breaking [57–61, 83–85, 308, 309]. It has been used extensively for the performance of global fits for LHC Run I [63, 90, 232, 310] and Run II data [3, 66, 103] data as discussed for instance in Chapter 5, and allows for the combination of Higgs measurements with the results of experimental analyses of anomalous triple gauge couplings both from LEP [227, 306] and the LHC [63, 227, 233, 235, 236, 242, 311].

Our dimension-six operator set is based on the SM field content and (gauge) symmetries as discussed in detail in Chapter 2. We impose C and P invariance [89] and assume a Yukawa coupling structure for the Higgs couplings to fermions. This leaves us with the Lagrangian

$$\begin{aligned}\mathcal{L}_{\text{eff}} = &-\frac{\alpha_s}{8\pi}\frac{f_{GG}}{\Lambda^2}\mathcal{O}_{GG} + \frac{f_{BB}}{\Lambda^2}\mathcal{O}_{BB} + \frac{f_{WW}}{\Lambda^2}\mathcal{O}_{WW} + \frac{f_B}{\Lambda^2}\mathcal{O}_B + \frac{f_W}{\Lambda^2}\mathcal{O}_W + \frac{f_{WWW}}{\Lambda^2}\mathcal{O}_{WWW} \\ &+ \frac{f_{\phi 2}}{\Lambda^2}\mathcal{O}_{\phi 2} + \frac{f_{\phi 3}}{\Lambda^2}\mathcal{O}_{\phi 3} + \frac{f_\tau m_\tau}{v\Lambda^2}\mathcal{O}_{e\phi,33} + \frac{f_b m_b}{v\Lambda^2}\mathcal{O}_{d\phi,33} + \frac{f_t m_t}{v\Lambda^2}\mathcal{O}_{u\phi,33} \\ &+ \text{invisible decays}\,, \end{aligned} \tag{6.5}$$

with the operators defined in Eqs. (2.8)–(2.11) and $\Lambda \gg v$ being the scale of the assumed UV-complete model. Note that we include the operator $\mathcal{O}_{\phi 3}$, defined in Eq. (2.10), in our effective Lagrangian which describes a modification of the trilinear and quartic couplings of the Higgs potential. Invisible Higgs decays are included in terms of a contribution to the total Higgs width, the same way they were considered for our 13 TeV analysis, described below Eq. (5.2). All but one operator in Eq. (6.5) influence Higgs couplings to other SM particles. The pure gauge operator $\mathcal{O}_{WWW}$, on the other hand, is needed to fully describe anomalous triple gauge couplings in a gauge-invariant framework and is tightly constrained from kinematic distributions of di-boson final states. As already discussed in Sec. 5.3, an anomalous triple gluon operator can be neglected in a global Higgs analysis, since it is constrained by multi-jet production at 13 TeV to a level that will prevent it from having visible effects on the Higgs sector [219]. We assume that this pattern will be the same at a 27 TeV collider.

We have neglected the effect of fermionic Higgs-gauge operators in Eq. (2.12) for now which require a combination of the Higgs–gauge analysis with electroweak precision data. They contribute to Higgs production in association with a vector boson by modifying the $f\bar{f}V$ couplings and inducing new $ff\bar{f}VV$ and $f\bar{f}Vh$ vertices. Despite being aware of their relevance for a global fit as seen in Chapter 5 and discussed in Refs. [3, 235, 293], such an analysis is beyond the scope of this projection. Eventually the fermionic Higgs-gauge operators should be part of a global SMEFT fit, not only because of their influence on the operators given in Eq. (6.5), but also because we expect the fermionic operators themselves to obtain meaningful constraints from an analysis of 27 TeV Higgs data.

For the description of new physics effects in terms of the effective Lagrangian given in Eq. (6.5), we follow the approach of Chapter 5 and include contributions from the dimension-six squared term in our amplitude. For each diagram, we only allow for a single insertion of a dimension-six operator when considering kinematic distributions, i.e. we neglect kinematic effects of the operators on the decays of the Higgs and gauge bosons.

One of the main advantages of SM effective field theory with respect to a description in the Δ-framework, is its ability to describe new Lorentz structures. Therefore, we expect valuable constraints on its Wilson coefficients to come from kinematic distributions probing interactions with a large momentum flow. In our global analysis, we include four single Higgs and four di-boson distributions listed in Tab. 6.2. They are based on existing 8 TeV analyses [64] where they were validated with data [312,313]. For event generation we use the same tool chain as in Chapter 5, i.e. MadGraph5 [254] in combination with Pythia6 [255] which we run on our own FeynRules [280] implementation of the dimension-six operators. We employ a fast detector simulation with Delphes3 [193] and assume two ATLAS/CMS-like experiments. Since we are mostly interested in the high-momentum regime, we use the cuts for those whenever different cuts defined for different phase space regions. Finally, for Higgs pair production we make use of the kinematic information in the $pp \to hh \to b\bar{b}\gamma\gamma$ channel, as pioneered in Ref. [314]. We include a distribution in terms of m_{hh}, accounting for two different jet multiplicities [13]. We will discuss further details of the Higgs pair production process and the relevant operators in Sec. 6.4.

The range of the kinematic distributions is optimized such that the highest bins contain a sizeable number of signal events. Specifically, we ignore phase space regions with fewer than three signal events for an integrated luminosity of 15 ab^{-1}. Comparing the upper limits of the kinematic distributions listed in Tab. 6.2 we see that the di-boson channels probe a much larger momentum flow than the Vh channels. For example, comparing WZ production with Wh production, we find that the reach in p_T^V is 2.4 TeV for WZ, while Wh production is only sensitive up to $p_T^V < 750$ GeV. The reason for this are the momentum-dependent WWZ couplings, leading to larger signal rates for VV production, namely $\sigma_{WZ} = 61.1$ pb vs $\sigma_{Wh} = 2.8$ pb at 27 TeV and to leading order [254], as well as to larger tails.

In Fig. 6.2 we present the results of the global Higgs-gauge analysis in terms of the effective Lagrangian given in Eq. (6.5). The typical reach of a 27 TeV hadron collider is well above 1 TeV. Comparing this number to the ranges of the distributions given in Tab. 6.2, we find that our Higgs analysis does not have any serious EFT validity issues, provided we do not see a pole in the di-boson channels. For some of the Wilson coefficients we find asymmetric upper and lower limits which we will discuss in more detail in the next section.

Comparing the limits on the Wilson coefficients for our two luminosity benchmarks, we see that the

channel	observable	# bins	range [GeV]
$WW \to (\ell\nu)(\ell\nu)$	$m_{\ell\ell'}$	10	$0 - 4500$
$WW \to (\ell\nu)(\ell\nu)$	$p_T^{\ell_1}$	8	$0 - 1750$
$WZ \to (\ell\nu)(\ell\ell)$	m_T^{WZ}	11	$0 - 5000$
$WZ \to (\ell\nu)(\ell\ell)$	$p_T^{\ell\ell}$ (p_T^Z)	9	$0 - 2400$
WBF, $h \to \gamma\gamma$	$p_T^{\ell_1}$	9	$0 - 2400$
$Vh \to (0\ell)(b\bar{b})$	p_T^V	7	$150 - 750$
$Vh \to (1\ell)(b\bar{b})$	p_T^V	7	$150 - 750$
$Vh \to (2\ell)(b\bar{b})$	p_T^V	7	$150 - 750$
$hh \to (b\bar{b})(\gamma\gamma)$, $2j$	m_{hh}	9	$200 - 1000$
$hh \to (b\bar{b})(\gamma\gamma)$, $3j$	m_{hh}	9	$200 - 1000$

Table 6.2: Kinematic distributions included in the input data set of the analysis. The number of bins includes an overflow bin for all channels. See text for details on the event generation.

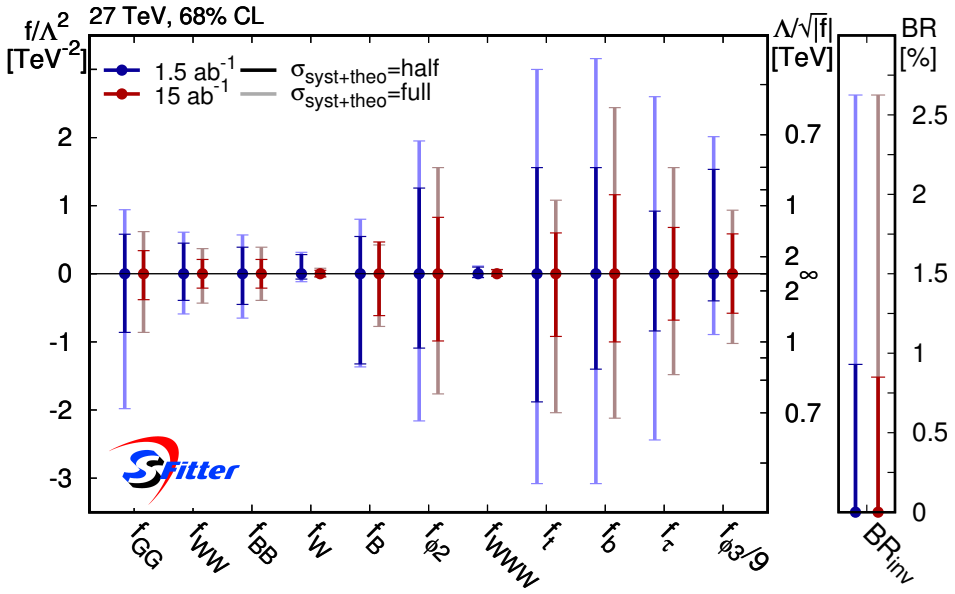

Figure 6.2: 68% limits on the Wilson coefficients of the effective dimension-six Lagrangian in Eq. (6.5) as a result of the global Higgs-gauge analysis. All limits are shown as profiled over all other Wilson coefficients. Figure taken from Ref. [2].

balance of statistical, systematic, and theory uncertainties in the SMEFT analysis is significantly different from the one based on the non-linear coupling modifiers shown in Fig. 6.1. An increase of the luminosity from 1.5 ab^{-1} to 15 ab^{-1} can significantly enhance the sensitivity of our global fit. This is due to that fact that a larger luminosity extends the reach of kinematic distributions, which in their tails are always statistically limited. Because of the correlation between the operators, this effect also translates to the modified Yukawa couplings $f_{t,b,\tau}$, which do not change the Lorentz structure. However, we see that the limits on those dimension-six operators are much more strongly influenced by the assumed systematic and theory uncertainties. As a result, we typically find stronger limits on the Wilson coefficients of operators which modify the Lorentz structure of some Higgs interaction than for the Yukawa-like operators or the operator $\mathcal{O}_{\phi 2}$, which introduces a wave function renormalization for the Higgs field and only changes the kinematics of Higgs pair production. Operators inducing additional momentum-dependences in interaction vertices can be constrained to the level of $\Lambda/\sqrt{f} \approx 3$ TeV and beyond, for high luminosity and improved systematics and theory uncertainties. A dedicated 27 TeV study developing analysis ideas not realized at 8 TeV is expected to further increase the sensitivity, especially for operators modifying kinematic distributions.

The asymmetric limits on f_B prompt us to study the limit setting on this Wilson coefficient in more detail. As we have already seen in Sec. 5.5, the corresponding operator which induces a new Lorentz structure for the hZZ coupling and a tree-level $hZ\gamma$ vertex is dominantly constrained through Vh production at high momentum transfer, i.e. through the p_T^V distributions from Tab. 6.2 for our analysis. In their highest bins we probe sizeable ratios p_T/Λ, which come, however, with large statistical uncertainties. In the range of the Wilson coefficient f_B that we are sensitive to, the dimension-six squared contributions can be of the same order as the interference terms of diagrams with an insertion of the dimension-six operator with the SM diagram. For $f_B/\Lambda > 0$ where the interference terms with the SM are negative, the dimension-six squared terms can compensate for the loss in event number and creates a second point in parameter space predicting the SM event counts, effectively leading to a secondary minimum of the log-likelihood. The precise position of this secondary solution differs for different values of $p_{T,V}$, i.e. for different bins considered in our analysis. In total, these effects lead to a slightly asymmetric measurement of f_B/Λ. The visibility of the dimension-six-squared term in a specific observable does by no means signal the breakdown of the effective Lagrangian [77]. The validity of the effective field theory is dependent on the specific assumptions on the underlying UV-

complete model, as the breakdown of the theory is caused by visible effects of the on-shell contributions of the new particles [292]. A truncation of the predicted number of events in the effective theory after the linear term in f/Λ^2 would lead to symmetric limits on the Wilson coefficients. Note, however, that using this approach would lead to a more narrow likelihood function and would overestimate the lower bounds on the parameter f_B. These uncertainties in the EFT framework are not considered in our global analysis. They should be considered when interpreting and matching our results to a UV complete model [315, 316].

6.4 Constraining the Higgs self-interaction in a global fit

The study of the Higgs self-coupling is a probe of the shape of the Higgs potential. A self-coupling enhanced with respect to the SM expectation could have interesting phenomenological consequences for vacuum stability and baryogenesis [37, 48]. Because of the modest reach of the LHC, the self-coupling is not yet included in most global analyses of SM-like Higgs couplings. Current LHC analyses deliver constraints of

$$\begin{aligned} -5.0 < \frac{\lambda_{3h}}{\lambda_{3h}^{\rm SM}} < 12.1 \qquad & \text{95\% CL, direct search in di-Higgs production [317]} \\ -3.2 < \frac{\lambda_{3h}}{\lambda_{3h}^{\rm SM}} < 11.9 \qquad & \text{95\% CL, indirect serch in single Higgs production [318].} \end{aligned} \tag{6.6}$$

A 27 TeV hadron collider with a large integrated luminosity, however, would deliver meaningful measurements of di-Higgs production as a probe of the Higgs self-coupling. Including those measurements as a new set of constraints and adding the operator $\mathcal{O}_{\phi 3}$ describing a modified Higgs potential with its corresponding Wilson coefficient as an additional parameter to our global fit is a significant improvement as compared to the Run I legacy analysis [64]. Dedicated studies for the expected reach of a 27 TeV hadron collider with an integrated luminosity of 15 ab^{-1} for the determination of the Higgs self-coupling already exist [13]. As a reference, we quote the expected limit from a one-parameter fit

$$\frac{\lambda_{3h}}{\lambda_{3h}^{\rm SM}} = \begin{cases} 1 \pm 15\% & \text{68\% CL} \\ 1 \pm 30\% & \text{95\% CL.} \end{cases} \tag{6.7}$$

To translate this limit on the Higgs self-coupling into our effective Lagrangian framework given by Eq. (6.5), we assume that the underlying new physics will only generate the operator $\mathcal{O}_{\phi 3}$. In that case we directly map the effect of a modified λ_{3h} onto the Wilson coefficient $f_{\phi 3}$, as no correlations between different operators arise. Since we are free to define a modified Higgs potential as our physics hypothesis [48], let us base our first analysis on the following simple description

$$V = \mu^2 \, \frac{(v+h)^2}{2} + \lambda \, \frac{(v+h)^4}{4} + \frac{f_{\phi 3}}{3\Lambda^2} \, \frac{(v+h)^6}{8} \, . \tag{6.8}$$

We find for the reach of the dedicated self-coupling analysis [117]

$$\lambda_{3h} = \lambda_{3h}^{\rm SM} \left(1 + \frac{2v^2}{3m_h^2} \, \frac{f_{\phi 3} v^2}{\Lambda^2} \right) \qquad \text{and} \qquad \left| \frac{\Lambda}{\sqrt{f_{\phi 3}}} \right| \gtrsim \begin{cases} 1 \text{ TeV} & \text{68\% CL} \\ 700 \text{ GeV} & \text{95\% CL.} \end{cases} \tag{6.9}$$

The above setup is in direct conflict with the effective Lagrangian approach, as we are not taking account all operators consistent with the symmetry assumptions. For our global study of the Higgs self-coupling, we will instead use the effective Lagrangian in Eq. (6.5). As we have already discussed in Sec. 2.4, the operator $\mathcal{O}_{\phi 2}$ also affects the Higgs pair production process by inducing a momentum-dependent self-coupling [117, 319].

In order to disentangle the effects of the operator $\mathcal{O}_{\phi 2}$, which induces a new Lorentz structures for triple Higgs couplings, from those of the operator $\mathcal{O}_{\phi 3}$, which modifies the total rate only, we can make use of the kinematic information from Higgs pair production encoded in the m_{hh} distribution [13, 297]. We

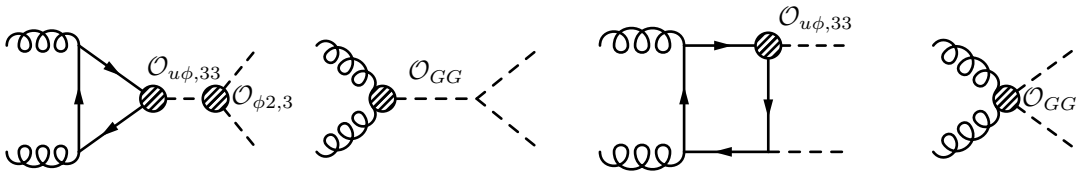

Figure 6.3: Leading order Feynman diagrams of the dominant modes for di-Higgs production including contributions from the dimension-six operators in the effective Lagrangian in Eq. (6.5).

should bear in mind, however, that di-Higgs production is not only influenced by operators modifying the Higgs self-coupling. In Fig. 6.3, we display the relevant leading order Feynman diagrams for di-Higgs production including the contributions from dimension-six operators. The process is also sensitive to modifications of the $ht\bar{t}$, hgg, $hhgg$ couplings induced by the operators $\mathcal{O}_{u\phi,33}$ and $\mathcal{O}_{GG}$. Those operators are also constrained from single Higgs production, as seen in Sec. 6.3. In principle, di-Higgs production can also be affected by the chromo-magnetic dipole operator $\mathcal{O}_{tG}$, defined in Eq. (5.6), due to its contribution to the $t\bar{t}g$ coupling. However, we neglect this operator in our analysis, see Sec. 5.3. For single Higgs production, following Refs. [320, 321] and especially Ref. [246] we will also neglect the loop effects of $\mathcal{O}_{\phi 3}$. Finally, as our limits on the Higgs self-coupling are base on a differential distribution, they will always be statistically limited even at the 27 TeV collider, in contrast to the typical total rate measurements discussed before.

As both $\mathcal{O}_{\phi 2}$ and $\mathcal{O}_{\phi 3}$ contribute to modifications of the Higgs self-coupling, we should study their correlation in detail. In fact, we find such correlation in Fig. 6.4, with asymmetric uncertainty bands for positive and negative values of the Wilson coefficients. The asymmetries arise from the fact that positive and negative deviations of the Higgs self-coupling affect different phase space regions as a result of the relative importance for the two dominant diagrams [297]: A value of the Higgs self-coupling enhanced with respect to the SM value can be tested around the threshold $m_{hh} \approx 2m_h$, because of the s-channel suppression in the diagram $gg \to h^* \to hh$. On the other hand, the best constraints on a decreased self-coupling, i.e. with an enhanced relative contribution from the box diagram, come from large values of m_{hh}. Since $\mathcal{O}_{\phi 2}$ induces momentum-dependent couplings, we expect large effects from this operator in the high-m_{hh} regime. As a result, $\mathcal{O}_{\phi 3}$ exhibits an asymmetric uncertainty band. The asymmetry is even more pronounced for the 95% confidence limits displayed in Fig. 6.5. From this

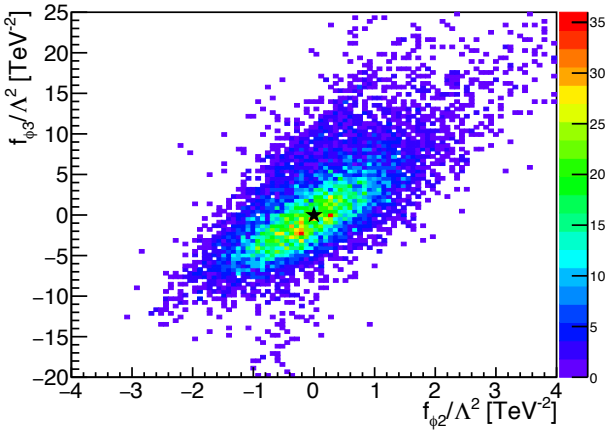

Figure 6.4: Distribution of the best fit points of our toy Monte Carlo data set in terms of the Wilson coefficients $f_{\phi 2}$ and $f_{\phi 3}$, demonstrating the correlations between the corresponding operators which dominantly influence Higgs pair production. The color coding represents the number of toy events. Figure taken from Ref. [2].

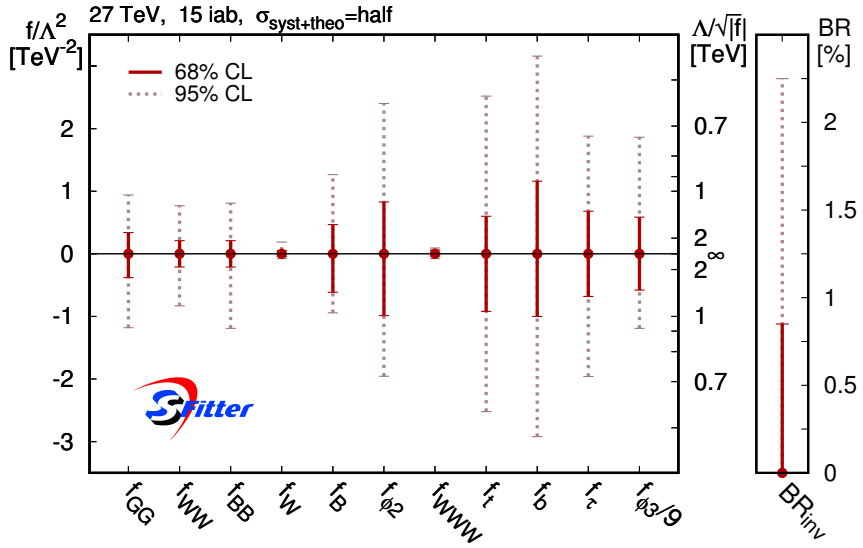

Figure 6.5: 68% and 95% CL limits on the Wilson coefficients of the effective dimension-six Lagrangian in Eq. (6.5) as a result of the global Higgs-gauge analysis, complementing the high-luminosity and improved-error scenario of Fig. 6.2. Notice that the 68% and 95% CL limits cannot be interpreted as Gaussian 1σ and 2σ limits for many of the Wilson coefficients. Figure taken from Ref. [2].

figure, we read off the limits on $f_{\phi 3}$

$$\begin{aligned} &\frac{\Lambda}{\sqrt{|f_{\phi 3}|}} > 430 \text{ GeV} && && 68\% \text{ CL} \\ &\frac{\Lambda}{\sqrt{|f_{\phi 3}|}} > 245 \text{ GeV} \quad (f_{\phi 3} > 0) \quad \text{and} && \frac{\Lambda}{\sqrt{|f_{\phi 3}|}} > 300 \text{ GeV} \quad (f_{\phi 3} < 0) && 95\% \text{ CL}. \end{aligned} \tag{6.10}$$

Obviously, the limits from our global analysis are diluted with respect to those from the one-parameter analysis quoted in Eq. (6.9), especially due to the correlation between $\mathcal{O}_{\phi 2}$ and $\mathcal{O}_{\phi 3}$. In fact, the effects from those two operators for similar values of f/Λ^2 cancel out at large momentum flow through the triple-Higgs vertex, $m_{hh} \gtrsim 1$ TeV. This partial cancellation of the effects of $\mathcal{O}_{\phi 2}$ and $\mathcal{O}_{\phi 3}$ is not accounted for in the usual Higgs pair analyses.

6.5 Conclusion and outlook

We have performed a global analysis of the Higgs-gauge sector of a 27 TeV hadron collider, following the established SFitter Run I legacy results [63,64] and adding Higgs pair production measurements, sensitive to the Higgs self-coupling, to our input data set.

We interpret our global analyses in two different frameworks: First, we use the Δ-framework describing modified SM-like Higgs couplings, motivated by an effective theory with non-linearly realized electroweak symmetry breaking. Our results suggest a sensitivity of a 27 TeV hadron collider to 3 ... 5% deviations from the SM coupling values. Since this framework can only describe modifications of total rates, the analyses are rapidly limited by systematics and theory uncertainties beyond attobarn-level integrated luminosities.

Second, using an effective Lagrangian in the SMEFT framework, allows us to describe changes in the Lorentz structures of the Higgs and gauge boson couplings. We can hence increase the sensitivity of our fit by including di-boson rates and momentum-dependent kinematic distributions in the global analysis. We find that a global Higgs-gauge analysis at a 27 TeV hadron collider will be sensitive to invisible Higgs branching ratios below one percent. With the inclusion of di-Higgs measurements in our data set, the global fit lets us set meaningful constraints on a modified Higgs potential at dimension

six. The Wilson coefficient of the additional operator describing such changes of the potential can be constrained by a kinematic analysis of Higgs pair production [13], if we control the correlation with the operator $\mathcal{O}_{\phi 2}$. We find a TeV-scale reach of our global analysis of the Higgs-gauge sector using an effective Lagrangian framework given order-one Wilson coefficients for most dimension-six operators. Operators inducing new Lorentz structures of the Higgs and gauge boson couplings can be more strongly constrained than those sensitive to modifications of total rates only, yielding limits beyond the 3 TeV level. If we compare those numbers with the current reach of LHC Run II discussed in Chapter 5 and in the literature [3, 66, 244], we find that an energy increase of the LHC to 27 TeV could increase the bounds on the new physics scale by more than 50%. The limits on operators describing modifications of the Higgs self-coupling are obviously diluted in a global fit compared to a one-parameter analysis [13]. This stresses the importance of precision test of the Higgs couplings to other SM particles in single-Higgs production for the extraction of information of the global structure of the Higgs potential. For a thorough investigation of the sensitivity of a 27 TeV hadron collider to the Higgs self-coupling, multiple production and decay modes of di-Higgs production should be combined. Experimental studies on the reach of a high-energy upgrade of the LHC for the trilinear Higgs self-coupling [322] suggest similar sensitivity for the included $b\bar{b}\gamma\gamma$ signature and $b\bar{b}\tau\tau$ and important contributions from $b\bar{b}b\bar{b}$, as well as, sub-dominantly, $b\bar{b}WW$ and $b\bar{b}ZZ$ with leptonic decays. Still, our analysis indicates that a 27 TeV hadron collider will for the first time deliver meaningful constraints on this fundamental physics parameter and probe the global structure of the Higgs potential.

7 | Conclusion and Outlook

The discovery of a Higgs boson [7,8] indicates that EWSB is indeed the mechanism behind the generation of gauge boson and fermion masses [4–6], making the exploration of the local and global properties of the Higgs potential one of the primary tasks of current and future research in particle physics. After EWSB, the local properties of the Higgs potential in the vicinity of the vacuum can be tested at the LHC in the form of Higgs couplings to other SM particles. A meaningful probe of its global structure through the direct measurement of the trilinear Higgs self-coupling will be left as a crucial task for next generation colliders. In this thesis, we focussed on a precise determination of Higgs couplings and their global analysis in a comprehensive framework. The results of these studies are not only a crucial input for future tests of the global structure of the Higgs potential, they also provide important constraints on physics beyond the Standard Model in the Higgs sector.

There is a plethora of models attempting to overcome the shortcomings of the Standard Model by modifications of the Higgs sector. In particular, an extended Higgs sector might solve the problem of vacuum stability [33–36], provide a candidate for dark matter [14–32], or might be related to an explanation for the baryon-antibaryon asymmetry in the universe through electroweak baryogenesis [37–49]. Testing and constraining these possible extensions of the SM Higgs sector, in principle requires both targeted searches for the exotic signatures predicted by those BSM models as well as a precise determination of the interactions anticipated in the SM. However, the lack of discoveries beyond the Higgs boson as well as ever more precise measurements of the various Higgs-production and decay channels have shifted our focus towards the latter. Aiming at increasing the precision of Higgs coupling measurements, we have discussed several aspects of data analysis and interpretation. First, we concentrated on fully exploiting the data in a specific Higgs-production and decay channel, namely Higgs decays to invisible particles in the weak-boson-fusion production mode, by using low-level input variables and performing a multivariate analysis. Second, the SM-like results of LHC measurements in the Higgs sector motivate an interpretation of new physics effects in a model-independent framework. Using the SMEFT framework, we performed a global analysis of the Higgs-gauge sector based on LHC Run I+II data and EWPD. Finally, we estimated the reach of a potential 27 TeV upgrade of the LHC, including a modified Higgs potential and di-Higgs data.

The Higgs decay-channel with arguably the largest motivation from a beyond Standard Model perspective is the Higgs decay into invisible particles. An invisible Higgs branching ratio is generically predicted by Higgs portal models, which have been developed in the context of dark matter [14–32] or electroweak baryogenesis [41–49]. In Chapter 4, we studied the most sensitive channel for the search for invisible Higgs decays at the LHC, Higgs production in weak boson fusion. Historically, in this channel QCD backgrounds are suppressed by the application of a central jet veto [144]. In our analysis, we aimed at improving the sensitivity to an invisible Higgs branching ratio by going beyond such a simple veto and taking advantage of the full jet- and subjet-level information on the two tagging jets. We focussed on a systematic study of subjet-level observables targeting quark/gluon discrimination and found that these variables indeed reflect the parton content of the WBF Higgs signal and its QCD backgrounds. However, in presence of jet-level observables, the subjet-level variables do not significantly increase the sensitivity to invisible Higgs searches in a multivariate analysis. This indicates that subjet observables are only over-constraining a process which is already fully described the jet-level variables. Nonetheless, we can increase the reach of our analysis by studying jets with low transverse

momenta. While this is clearly beyond the experimental possibilities, it motivates a dedicated study of the sensitivity of the WBF analysis in terms of track jets rather than fully reconstructed jets which we leave for future work.

In Chapter 2, we introduced SM effective field theory as a phenomenologically powerful and largely model-independent framework to describe the effects of new physics. In principle, at dimension six its effective Lagrangian consists of 59 independent operators barring hermitian conjugation and assuming flavor universality. However, only 18 of those operators are relevant for LHC Higgs physics in the sense that they either receive important constraints from the Higgs sector or that, within their constraints from other sectors, they influence the limits on other operators due to correlations. We confronted these operators with experimental data in global analyses using the SFitter fitting framework [62], which allows for the combination of statistical, systematic and theoretical uncertainties as well as their correlations, as discussed in Chapter 3.

We presented a global analysis of the LHC Run I+II data covering Higgs and di-boson measurements in the SMEFT framework in Chapter 5. We include a total of 18 bosonic and fermionic operators and account for invisible decays of the Higgs boson through their contribution to the Higgs width. Compared to previous SFitter analyses of the Higgs-gauge sector in which only 10 operators were considered [63,64], this brings us a significant step closer towards a global SMEFT fit. The inclusion of fermionic Higgs-gauge operators proved to be relevant for Higgs physics and demands a combination of LHC data with EWPD.

On the experimental side, the largest boosts for the sensitivity to Higgs couplings at LHC Run II result from the observation of all third family Yukawa couplings, a plethora of $t\bar{t}h$ measurements as well as momentum-related kinematic distributions for associated Higgs and di-boson production. To disentangle the effect of the additional set of operators relevant for EWPD from the effect of the new experimental results, we first restricted the set of input parameters to the Wilson coefficients of the 10 operators included in the Run I analysis [63, 64] and updated the experimental input data set only. We found that in this setup all limits on dimension-six operators are consistently improved by adding the Run II data to the existing Run I dataset. The typical Run II limits at 95% CL range around $\Lambda/\sqrt{f} = 400$ ... 800 GeV for bosonic and Higgs-fermion operators. Specifically, large improvements arise for the limits on a modified top Yukawa coupling and an effective Higgs-gluon coupling from the observation of $t\bar{t}h$ Higgs production. Moreover, the addition of a kinematic measurement of Vh production up to ~ 1 TeV energies significantly improves the limits on the bosonic operators $\mathcal{O}_W$ and $\mathcal{O}_B$.

A second fit of the LHC Run II data set and EWPD including fermionic Higgs-gauge operators revealed their relevance for the Higgs-gauge sector. In spite of being strongly constrained by EWPD, the effect of fermionic Higgs-gauge operators is enhanced through 4-point $hVf\bar{f}$ vertices in associated Higgs production. As a result, the Wilson coefficients of these operators induce strong correlations with $f_{B,W}$ and weaken their limits by up to a factor two after profiling. On the other hand, we found that LHC Higgs data add to the sensitivity to operators constrained by EWPD in a global fit. Generally, fermionic Higgs-gauge operators are consistently constrained to $\Lambda/\sqrt{f} = 5$ ... 10 TeV. Our results motivate the future combination of data from the Higgs and electroweak sectors with results from e.g. the top sector for a more comprehensive view on the LHC physics picture.

Future colliders will not only allow us to improve the current limits on Higgs couplings to other SM particles, a milestone of their physics program will be the probe of the trilinear Higgs self-coupling in di-Higgs production. A meaningful constraint on the triple-Higgs coupling will provide valuable insight on the global structure of the Higgs potential. Currently, several ideas for next generation colliders are discussed. We focussed our analysis on a proposed 27 TeV upgrade of the LHC and performed a global analysis of the Higgs-gauge sector in Chapter 6. Our analysis is extrapolated from SFitter Run I legacy results [63, 64], including kinematic distributions of Higgs and di-boson production, and complemented by di-Higgs production measurements.

We carried out our global analyses both in terms of Higgs-coupling modifiers in the Δ-framework and in terms of a dimension-six Lagrangian in the SMEFT framework. For coupling modifiers, we found that a 27 TeV hadron collider will be sensitive to deviations from the SM coupling-values at the level of 3 ... 5%. To include the effects of modified Lorentz structures of the Higgs and gauge-boson couplings, we further investigated the reach of the HE-LHC in the SMEFT framework based on 11 dimension-six operators including a modification of the Higgs potential. Given order-one Wilson coefficients, we found a TeV-scale reach for most dimension-six operators in our global analysis of the Higgs-gauge sector. Stronger constraints, yielding limits beyond the 3 TeV level, can be obtained for those operators that modify kinematic distributions through new Lorentz structures of the Higgs and gauge-boson couplings. Comparing those numbers with the current reach of LHC Run II discussed in Chapter 5, we found that the HE-LHC will increase the bounds on the new physics scale by more than 50%.

The inclusion of di-Higgs measurements [13] in our data set allowed us to set constraints on a modified Higgs potential at dimension six. In our global fit, we found a rather strong dilution of the limit on the operator $\mathcal{O}_{\phi 3}$, describing such an alteration of the Higgs potential, with respect to a one-parameter analysis [13]. The weakened constraints result from strong correlations between the operator $\mathcal{O}_{\phi 3}$ and other operators influencing di-Higgs measurements on the production side. The fact that these operators also affect single-Higgs production highlights the importance of precise Higgs-coupling measurements for the extraction of the Higgs self-coupling in a global analysis. Still, our results indicate that a 27 TeV high-energy upgrade of the LHC will for the first time probe the structure of the Higgs potential through a meaningful measurement of the Higgs self-coupling.

The strong impact of the inclusion of fermionic Higgs-gauge operators and the combination of the Higgs-gauge data set with EWPD on the limits on some of the bosonic operators (in particular on $\mathcal{O}_B$) for the 13 TeV fit in Chapter 5 motivates the extension of our global analysis for a 27 TeV collider by this operator and data set. Moreover, the inclusion of more kinematic analyses and their adjustment to the increased energy will further refine our conservative estimate of the reach of such a machine. For a thorough investigation of the sensitivity of a 27 TeV hadron collider to the Higgs self-coupling, the combination of multiple production and decay modes of di-Higgs production will provide a more complete picture.

In summary, LHC Run II measurements allow for a precise determination of Higgs couplings to other SM particles and thereby probe the local properties of the Higgs potential. Data driven analysis techniques increase the LHC sensitivity to the couplings of the Higgs boson for individual production and decay channels which we can describe and combine using the SMEFT framework. Global fits of the Wilson coefficients of dimension-six operators in the SMEFT framework grant a comprehensive picture of the status of LHC Higgs physics. The inclusion of more operators and measurements, e.g. of the top sector, in our analysis will further broaden our view on the experimental constraints and effort to harness this data is underway. Besides increasing the significance of single-Higgs measurements, future colliders will be capable of producing a statistically relevant number of di-Higgs events. Thereby, they will provide meaningful constraints on the Higgs self-coupling and hence deliver the first direct collider probes of the global structure of the Higgs potential. Overall, our detailed discussion of invisible Higgs decays as well as our analyses of LHC Run II data and prospects for a future 27 TeV collider in the SMEFT framework provide a global view on Higgs couplings at the current and at an energy-upgraded LHC.

Acknowledgments

First of all, I am grateful to my thesis advisor Tilman Plehn for his enthusiasm and support and for truly committing to the word *Doktorvater*. It has been a pleasure to work with him, to learn from him and, how do I put this most elegantly, to have some refreshing discussions with him.

Moreover, I would like to thank Jan Martin Pawlowski for refereeing this thesis and Hans-Christian Schultz-Coulon as well as Björn Malte Schäfer for completing my examination committee.

I gratefully acknowledge (not only financial) support from the Research Training Group "Particle Physics at the LHC" and the International Max Planck Research School "Precision Tests of Fundamental Symmetries". In particular, I would like to thank the many brilliant women in our physics department for our lunches and trainings, for their openness and good advice.

The projects presented in this thesis are based on work in collaboration with sharp and kind people: I am indebted to Michael Rauch and Dirk Zerwas on the SFitter side, to Dorival Gonçalves and Michihisa Takeuchi, and especially to Tyler Corbett from whom I learned a lot about effective field theory.

A big thank-you also goes to my proof-readers, Sebastian Bruggisser, Anja Butter, Patrick Foldenauer, Sebastian Schenk and Ramon Winterhalder, who turned this piece of text into a readable format. Especially to Sebastian, not only for reading every single one of what felt like a thousand iterations of parts of my thesis.

In Philosophenweg, I would like to thank everyone in our pheno group or, as I like to call them, the participants of my social studies. In particular (but not exclusively!) and in a random order, I would like to thank Anja Butter (the smarter half of the A-Team), Sebastian Bruggisser and Juan González Fraile for suffering through the pains of SFitter with me; Rhea Moutafis, Fabian Keilbach and Amartya Sengupta for the fun collaboration and for challenging me with their questions; Johann Brehmer for teaching me a million things on EFTs; Torben Schell for fixing a similar amount of compiler problems; Jennie Thompson for joining my first PhD project when I was a bit lost; Gonzalo Alonso-Álvarez for trampolining; Marco Bellagente - graaaazie; Nastya Filimonova for introducing us to an entirely new universe of sweets and for a fun road trip; the *Prolls*, Michael Rüssel for sharing his favorite poem, Peter Reimitz for our french connection and for keeping the entrance to *Schmelzpunkt* safe, and Ramon Winterhalder for teaching me to tie my shoes and for always being a perfect host; Simon Kast and Katja Böhnke for discussing about any aspect of life with me; and especially to the editors of the "LHC weekly" (Get the latest p_T cuts!), Patrick Foldauer and Amplitudian Schenk, who shared my PhD journey from day one until the end and who will luckily (at least for me) continue to share my path a little bit further down the way. Thank you for keeping me mentally sane, for sharing my terrible sense of humor, for always knowing to say the right thing.

This thesis would never have been finished without the continuous motivation and support by my parents and my sister Kerstin. I am very lucky to have you.

A | Appendix

A.1 EFT basis

In Section 2.3, we have explicitly listed the operators relevant for our study of Higgs physics. Here, we want to list the remaining operators in our basis for completeness. We will only list the operators including bosonic fields and refer to Table 1 of Ref. [309] for a complete list of four-fermion operators.

There are six bosonic CP-violating operators

$$\begin{aligned} &\mathcal{O}_{G\tilde{G}} = \phi^\dagger\phi\, G^a_{\mu\nu}\tilde{G}^{a\mu\nu} \qquad \mathcal{O}_{B\tilde{B}} = -\frac{g'^2}{4}\phi^\dagger B_{\mu\nu}\tilde{B}^{\mu\nu}\phi \qquad \mathcal{O}_{W\tilde{W}} = -\frac{g^2}{4}\phi^\dagger W_{\mu\nu}\tilde{W}^{\mu\nu}\phi \\ &\mathcal{O}_{B\tilde{W}} = -\frac{gg'}{4}\phi^\dagger B_{\mu\nu}\tilde{W}^{\mu\nu}\phi \quad \mathcal{O}_{WW\tilde{W}} = -\frac{ig^3}{8}\,\mathrm{Tr}\left(\tilde{W}_{\mu\nu}W^{\nu\rho}W^{\mu}_{\rho}\right) \qquad \mathcal{O}_{\tilde{G}} = f_{abc}\tilde{G}^{\rho}_{a\nu}G^{\nu}_{b\lambda}G^{\lambda}_{c\rho}\,, \end{aligned} \tag{A.1}$$

where we explicitly write out additional powers of the coupling strength g and g' instead of using the hatted fields as in Eq. (2.9) and the dual field strength tensors are defined as

$$\tilde{V}_{\mu,\nu} = \frac{1}{2}\epsilon_{\mu\nu\rho\sigma}V^{\rho\sigma}\,, \tag{A.2}$$

for $V = B$, W, G.

There are eight dipole operators, fermionic Higgs-gauge operators with a non SM-like Lorentz structure

$$\begin{aligned} &\mathcal{O}_{uW} = (\bar{Q}\sigma^{\mu\nu}u_R)\tau^a\,\tilde{\phi}\,W^a_{\mu\nu} \qquad \mathcal{O}_{uB} = (\bar{Q}\sigma^{\mu\nu}u_R)\,\tilde{\phi}\,B_{\mu\nu} \qquad \mathcal{O}_{uG} = (\bar{Q}\sigma^{\mu\nu}T^a u_R)\,\tilde{\phi}\,G^a_{\mu\nu} \\ &\mathcal{O}_{dW} = (\bar{Q}\sigma^{\mu\nu}d_R)\tau^a\,\phi\,W^a_{\mu\nu} \qquad \mathcal{O}_{dB} = (\bar{Q}\sigma^{\mu\nu}d_R)\,\phi\,B_{\mu\nu} \qquad \mathcal{O}_{dG} = (\bar{Q}\sigma^{\mu\nu}T^a d_R)\,\phi\,G^a_{\mu\nu} \\ &\mathcal{O}_{\ell W} = (\bar{L}\sigma^{\mu\nu}\ell_R)\tau^a\,\phi\,W^a_{\mu\nu} \qquad \mathcal{O}_{\ell B} = (\bar{L}\sigma^{\mu\nu}\ell_R)\,\phi\,B_{\mu\nu}\,. \end{aligned} \tag{A.3}$$

A.2 Combination of likelihoods

In Section 3.1.2, we have seen how to combine two likelihood functions which depend on the same nuisance parameter. Here, we want to combine the likelihood functions and profile over the nuisance parameter explicitly for the combination of Gaussian, Poissonian and flat uncertainties. In most cases, we will not take into account constant factors in the likelihoods (the normalization of the probability density functions) as they will result in irrelevant constants in a log-likelihood analysis anyways.

1. **Gauss + Gauss**
   The combination of two Gaussian likelihood functions can be performed analytically. We will consider the case of a background measurement in a control region. Profiling over the background

measurement ν_b^* yields a combined likelihood function of [117]

$$\begin{aligned} L_{\text{Gauss}}(\nu_s) &= \max_{\nu_b^*} \frac{1}{\sqrt{2\pi\sigma_d}} e^{-\frac{(d-\nu_b^*-\nu_s)^2}{2\sigma_d}} \frac{1}{\sqrt{2\pi\sigma_b}} e^{-\frac{(b-\nu_b^*)^2}{2\sigma_b}} \\ &= \frac{1}{2\pi\sqrt{\sigma_d\sigma_b}} e^{-\frac{(d-b-\nu_s)^2}{2(\sigma_d+\sigma_b)}} \,. \end{aligned} \tag{A.4}$$

Combining two Gaussian likelihood functions leads again to a Gaussian distributed likelihood function with the new width being the quadratic sum of the individual contributions.

2. **Poisson + Poisson**
We have already discussed the combination of two Poissonian distributed likelihood functions in Section 3.1.2. The combined likelihood, given the background measurement as a nuisance parameter is given by

$$L_{\text{Pois}}(\nu_s) = \max_{\nu_b^*} \frac{(\nu_s+\nu_b^*)^d}{d!} e^{-(\nu_s+\nu_b^*)} \frac{(\nu_b^*)^b}{b!} e^{-\nu_b^*} \,. \tag{A.5}$$

For large event numbers, we can approximate the Poisson distribution as a Gaussian and perform the profiling analytically. This is, however, not possible for small numbers for which we need to solve the problem numerically. Instead of numerically solving Eq. (A.5) we can also approximate the result using the formula

$$\frac{1}{\log L_{\text{Pois}}} \approx \frac{1}{\log L_{\text{Pois},d}} + \frac{1}{\log L_{\text{Pois},b}} \,, \tag{A.6}$$

which becomes exact in the Gaussian limit in Eq. (A.4).

3. **Flat + Flat**
Flat uncertainties are only applied to theoretical uncertainties in our framework. As such, they are irrelevant for the data and only concern the signal predictions. To account for several sources of theoretical uncertainties, we need to add up the individual uncertainties linearly and construct the total likelihood using the summed flat uncertainty [117]

$$L(\nu_s) \sim \theta(s-(\nu_s-\sigma_{\text{theo}}))\,\theta((\nu_s+\sigma_{\text{theo}})-s) \,, \qquad \sigma_{\text{theo}} = \sum_{\text{i}} \sigma_{\text{theo, i}} \,. \tag{A.7}$$

4. **Flat + Gauss**
Since we only apply flat uncertainties for theoretical uncertainties on the signal extraction, we will explicitly consider the case of uncertainties on the signal here.

$$\begin{aligned} L(\nu_s) &\sim \max_{s^*} \Theta\left[s^*-(\nu_s-\sigma_{\text{theo}})\right] \Theta\left[(\nu_s+\sigma_{\text{theo}})-s^*\right] \exp\left(-\frac{(s-s^*)^2}{2\,\sigma_{sys,s}^2}\right) \\ &= \max_{s^*\in[\nu_s-\sigma_{\text{theo}},\,\nu_s+\sigma_{\text{theo}}]} \exp\left(-\frac{(s-s^*)^2}{2\,\sigma_{sys,s}^2}\right) \\ &= \begin{cases} \exp\left(\dfrac{(s-(\nu_s+\sigma_{\text{theo}}))^2}{2\,\sigma_{sys,s}^2}\right), & \nu_s < s-\sigma_{\text{theo}} \\ 1, & |s-\nu_s| < \sigma_{\text{theo}} \\ \exp\left(\dfrac{(s-(\nu_s-\sigma_{\text{theo}}))^2}{2\,\sigma_{sys,s}^2}\right), & \nu_s > s+\sigma_{\text{theo}} \,. \end{cases} \end{aligned} \tag{A.8}$$

This procedure is called the RFit scheme [323]. Effectively, it corresponds to a shift of the predicted signal ν_s towards the measured signal s by the theoretical uncertainty σ_{theo}. The resulting log-likelihood function is a parabola with a flat plateau around its minimum.

5. **Flat + Poisson**
   The combination of flat and Poissonian uncertainties is equivalent to the combination of flat uncertainties with Gaussian uncertainties. The combined likelihood is flat in the region around the measured signal and in the tails the signal prediction is shifted towards the measurement

$$L(\nu_s) \sim \begin{cases} \frac{(\nu_s-\sigma_{\text{theo}})^s}{s!} e^{(\nu_s-\sigma_{\text{theo}})}, & \nu_s < s-\sigma_{\text{theo}} \\ 1, & |s-\nu_s| < \sigma_{\text{theo}} \\ \frac{(\nu_s+\sigma_{\text{theo}})^s}{s!} e^{(\nu_s+\sigma_{\text{theo}})}, & \nu_s > s+\sigma_{\text{theo}} \,. \end{cases} \tag{A.9}$$

6. **Gauss + Poisson**
   Finally, we need to combine the likelihood functions corresponding to Poissonian and Gaussian distributions. The combination of the likelihood functions would require a numerical profiling over the nuisance parameters, analogous to the combination of two Poissonian likelihoods. We again approximate the result as

$$\frac{1}{\log L} \approx \frac{1}{\log L_{\text{Gauss}}} + \frac{1}{\log L_{\text{Pois}}} \,, \tag{A.10}$$

   which is exact for large event numbers and agrees within a few percent for small event numbers. The likelihood contribution with the larger uncertainty (smaller likelihood) will dominate the combined likelihood.

A.3 Invisible Higgs decays - Zh benchmark

We compare our results for the sensitivity of invisible Higgs decays in weak boson fusion with the reach the leptonic associated production channel

$$pp \to Zh_{\text{inv}} \to \ell^+\ell^- \, h_{\text{inv}} \tag{A.11}$$

at the HL-LHC. With a signature of two same-flavor opposite-sign (SFOS) leptons plus missing energy, this channel is expected to suffer less from an increase of trigger thresholds compared to hadronic signatures. We generate events at 14 TeV using Sherpa and Delphes3.3, taking into account both the tree-level quark-induced production mode and the loop-level gluon-induced contribution with OpenLoops. The latter can have sizeable impact on the sensitivity of this search channel [161].

The dominant backgrounds to invisible Higgs decays in the leptonic Zh channel come from quark-induced and gluon-induced $Z_{\ell\ell}Z_{\nu\nu}$ production. Important background contributions also come from WZ production with a missing lepton from the W decay, WW production with the invariant mass of the leptons being accidentally close to the Z mass, and leptonic $t\bar{t}$ production. We generate events for all of these background processes using Sherpa, including a loop-level sample for the irreducible gluon-induced ZZ background using OpenLoops. We normalized the total rates to their respective NNLO predictions [76, 324–328].
For the leptonic Zh channel we do not expect a large benefit from using a BDT compared to a cut-and-count analysis because of the simple $2 \to 2$ kinematics. Nonetheless, to compare the results to our

Systematics	Luminosity [fb^{-1}]			
	36.1* [174]	36.1	300	3000
1% sys.	39%	39%	17%	8%
2% sys.		43%	20%	11%

Table A.1: 95% CLs limits on the invisible Higgs branching ratio from the leptonic Zh channel. The ATLAS result, indicated by an asterisk, is taken from Ref. [174].

WBF analysis we also apply a TMVA BDT analysis to this channel. We require the baseline cuts

$$\begin{aligned} p_{T,\ell_1} > 26\,\text{GeV} \qquad & p_{T,\ell_2} > 7\,\text{GeV} \qquad & \eta_e < 2.47 \qquad & \eta_\mu < 2.5 \\ |m_{\ell\ell} - m_Z| < 5\,\text{GeV} \qquad & \Delta R_{\ell\ell} < 1.8 \qquad & \not{E}_T > 60\,\text{GeV} \qquad & \Delta\phi(p_T^{\ell\ell}, \not{E}_T) > 2.7\,. \end{aligned} \tag{A.12}$$

In addition to the above variables, in the BDT analysis we include the observables

$$\left\{ \eta_{\ell_1},\ \eta_{\ell_2},\ \phi_{\ell_1},\ \phi_{\ell_2},\ \phi_{\not{E}_T},\ \frac{p_T^{\ell\ell}}{m_T},\ N_{\text{leptons}},\ N_{\text{jets}} \right\}\,. \tag{A.13}$$

We present the resulting 95% CLs limits in Table A.1, assuming a systematic uncertainty of 2%. We also show the results for a 1% uncertainty as a reference. We compare our finding with the expected ATLAS limit [172–174] at 13 TeV and find that appropriate data-driven background rejection techniques can compensate for otherwise large systematics. One of the main difference of our analysis with respect to the ATLAS search is the normalization of the leading ZZ background, where we apply a global K-factor to account for the NNLO correction [76, 324–328], while ATLAS uses bin-wise factors for m_{ZZ} [166, 329].

References

[1] A. Biekötter, F. Keilbach, R. Moutafis, T. Plehn, and J. Thompson, "Tagging Jets in Invisible Higgs Searches," *SciPost Phys.* **4** (2018) no. 6, 035, arXiv:1712.03973 [hep-ph].

[2] A. Biekötter, D. Gonçalves, T. Plehn, M. Takeuchi, and D. Zerwas, "The Global Higgs Picture at 27 TeV," *SciPost Phys.* **6** (2019) no. 2, 024, arXiv:1811.08401 [hep-ph].

[3] A. Biekötter, T. Corbett, and T. Plehn, "The Gauge-Higgs Legacy of the LHC Run II," arXiv:1812.07587 [hep-ph].

[4] P. W. Higgs, "Broken Symmetries and the Masses of Gauge Bosons," *Phys. Rev. Lett.* **13** (1964) 508–509.

[5] P. W. Higgs, "Broken symmetries, massless particles and gauge fields," *Phys. Lett.* **12** (1964) 132–133.

[6] F. Englert and R. Brout, "Broken Symmetry and the Mass of Gauge Vector Mesons," *Phys. Rev. Lett.* **13** (1964) 321–323.

[7] **ATLAS** Collaboration, G. Aad *et al.*, "Observation of a new particle in the search for the Standard Model Higgs boson with the ATLAS detector at the LHC," *Phys. Lett.* **B716** (2012) 1–29, arXiv:1207.7214 [hep-ex].

[8] **CMS** Collaboration, S. Chatrchyan *et al.*, "Observation of a new boson at a mass of 125 GeV with the CMS experiment at the LHC," *Phys. Lett.* **B716** (2012) 30–61, arXiv:1207.7235 [hep-ex].

[9] **ATLAS** Collaboration, M. Aaboud *et al.*, "Combined measurements of Higgs boson production and decay using up to 80 fb^{-1} of proton–proton collision data at $\sqrt{s} = 13$ TeV collected with the ATLAS experiment," Tech. Rep. ATLAS-CONF-2019-005, CERN, Geneva, Mar, 2019. https://cds.cern.ch/record/2668375.

[10] **CMS** Collaboration, A. M. Sirunyan *et al.*, "Combined measurements of Higgs boson couplings in proton-proton collisions at $\sqrt{s} = 13$ TeV," *Submitted to: Eur. Phys. J.* (2018) , arXiv:1809.10733 [hep-ex].

[11] J. H. Kim, Y. Sakaki, and M. Son, "Combined analysis of double Higgs production via gluon fusion at the HL-LHC in the effective field theory approach," *Phys. Rev.* **D98** (2018) no. 1, 015016, arXiv:1801.06093 [hep-ph].

[12] S. Di Vita, G. Durieux, C. Grojean, J. Gu, Z. Liu, G. Panico, M. Riembau, and T. Vantalon, "A global view on the Higgs self-coupling at lepton colliders," *JHEP* **02** (2018) 178, arXiv:1711.03978 [hep-ph].

[13] D. Gonçalves, T. Han, F. Kling, T. Plehn, and M. Takeuchi, "Higgs boson pair production at future hadron colliders: From kinematics to dynamics," *Phys. Rev.* **D97** (2018) no. 11, 113004, arXiv:1802.04319 [hep-ph].

[14] R. M. Schabinger and J. D. Wells, "A Minimal spontaneously broken hidden sector and its impact on Higgs boson physics at the large hadron collider," *Phys. Rev.* **D72** (2005) 093007, arXiv:hep-ph/0509209 [hep-ph].

[15] R. Barbieri, T. Gregoire, and L. J. Hall, "Mirror world at the large hadron collider," arXiv:hep-ph/0509242 [hep-ph].

[16] B. Patt and F. Wilczek, "Higgs-field portal into hidden sectors," arXiv:hep-ph/0605188 [hep-ph].

[17] O. Bertolami and R. Rosenfeld, "The Higgs portal and an unified model for dark energy and dark matter," *Int. J. Mod. Phys.* **A23** (2008) 4817–4827, arXiv:0708.1784 [hep-ph].

[18] M. Gonderinger, Y. Li, H. Patel, and M. J. Ramsey-Musolf, "Vacuum Stability, Perturbativity, and Scalar Singlet Dark Matter," *JHEP* **01** (2010) 053, arXiv:0910.3167 [hep-ph].

[19] S. Andreas, C. Arina, T. Hambye, F.-S. Ling, and M. H. G. Tytgat, "A light scalar WIMP through the Higgs portal and CoGeNT," *Phys. Rev.* **D82** (2010) 043522, arXiv:1003.2595 [hep-ph].

[20] M. H. G. Tytgat, "A light scalar WIMP through the Higgs portal?," *PoS* **IDM2010** (2011) 126, arXiv:1012.0576 [hep-ph].

[21] C. Englert, T. Plehn, D. Zerwas, and P. M. Zerwas, "Exploring the Higgs portal," *Phys. Lett.* **B703** (2011) 298–305, arXiv:1106.3097 [hep-ph].

[22] M. Pospelov and A. Ritz, "Higgs decays to dark matter: beyond the minimal model," *Phys. Rev.* **D84** (2011) 113001, arXiv:1109.4872 [hep-ph].

[23] X.-G. He and J. Tandean, "Hidden Higgs Boson at the LHC and Light Dark Matter Searches," *Phys. Rev.* **D84** (2011) 075018, arXiv:1109.1277 [hep-ph].

[24] P. J. Fox, R. Harnik, J. Kopp, and Y. Tsai, "Missing Energy Signatures of Dark Matter at the LHC," *Phys. Rev.* **D85** (2012) 056011, arXiv:1109.4398 [hep-ph].

[25] I. Low, P. Schwaller, G. Shaughnessy, and C. E. M. Wagner, "The dark side of the Higgs boson," *Phys. Rev.* **D85** (2012) 015009, arXiv:1110.4405 [hep-ph].

[26] C. Englert, T. Plehn, M. Rauch, D. Zerwas, and P. M. Zerwas, "LHC: Standard Higgs and Hidden Higgs," *Phys. Lett.* **B707** (2012) 512–516, arXiv:1112.3007 [hep-ph].

[27] A. Djouadi, O. Lebedev, Y. Mambrini, and J. Quevillon, "Implications of LHC searches for Higgs–portal dark matter," *Phys. Lett.* **B709** (2012) 65–69, arXiv:1112.3299 [hep-ph].

[28] B. Batell, S. Gori, and L.-T. Wang, "Exploring the Higgs Portal with 10/fb at the LHC," *JHEP* **06** (2012) 172, arXiv:1112.5180 [hep-ph].

[29] S. Baek, P. Ko, and W.-I. Park, "Invisible Higgs Decay Width vs. Dark Matter Direct Detection Cross Section in Higgs Portal Dark Matter Models," *Phys. Rev.* **D90** (2014) no. 5, 055014, arXiv:1405.3530 [hep-ph].

[30] A. Butter, T. Plehn, M. Rauch, D. Zerwas, S. Henrot-Versillé, and R. Lafaye, "Invisible Higgs Decays to Hooperons in the NMSSM," *Phys. Rev.* **D93** (2016) 015011, arXiv:1507.02288 [hep-ph].

[31] S. Banerjee, B. Batell, and M. Spannowsky, "Invisible decays in Higgs boson pair production," *Phys. Rev.* **D95** (2017) no. 3, 035009, arXiv:1608.08601 [hep-ph].

[32] R. K. Barman, G. Belanger, B. Bhattacherjee, R. Godbole, G. Mendiratta, and D. Sengupta, "Invisible decay of the Higgs boson in the context of a thermal and nonthermal relic in MSSM," *Phys. Rev.* **D95** (2017) no. 9, 095018, arXiv:1703.03838 [hep-ph].

[33] M. Sher, "Electroweak Higgs Potentials and Vacuum Stability," *Phys. Rept.* **179** (1989) 273–418.

[34] J. A. Casas, J. R. Espinosa, and M. Quiros, "Standard model stability bounds for new physics within LHC reach," *Phys. Lett.* **B382** (1996) 374–382, arXiv:hep-ph/9603227 [hep-ph].

[35] G. Degrassi, S. Di Vita, J. Elias-Miro, J. R. Espinosa, G. F. Giudice, G. Isidori, and A. Strumia, "Higgs mass and vacuum stability in the Standard Model at NNLO," *JHEP* **08** (2012) 098, arXiv:1205.6497 [hep-ph].

[36] A. V. Bednyakov, B. A. Kniehl, A. F. Pikelner, and O. L. Veretin, "Stability of the Electroweak Vacuum: Gauge Independence and Advanced Precision," *Phys. Rev. Lett.* **115** (2015) no. 20, 201802, arXiv:1507.08833 [hep-ph].

[37] C. Grojean, G. Servant, and J. D. Wells, "First-order electroweak phase transition in the standard model with a low cutoff," *Phys. Rev.* **D71** (2005) 036001, arXiv:hep-ph/0407019 [hep-ph].

[38] C. Delaunay, C. Grojean, and J. D. Wells, "Dynamics of Non-renormalizable Electroweak Symmetry Breaking," *JHEP* **04** (2008) 029, arXiv:0711.2511 [hep-ph].

[39] A. Noble and M. Perelstein, "Higgs self-coupling as a probe of electroweak phase transition," *Phys. Rev.* **D78** (2008) 063518, arXiv:0711.3018 [hep-ph].

[40] P. Huang, A. Joglekar, B. Li, and C. E. M. Wagner, "Probing the Electroweak Phase Transition at the LHC," *Phys. Rev.* **D93** (2016) no. 5, 055049, arXiv:1512.00068 [hep-ph].

[41] A. Kobakhidze, L. Wu, and J. Yue, "Electroweak Baryogenesis with Anomalous Higgs Couplings," *JHEP* **04** (2016) 011, arXiv:1512.08922 [hep-ph].

[42] K. Assamagan *et al.*, "The Higgs Portal and Cosmology," 2016. arXiv:1604.05324 [hep-ph]. http://lss.fnal.gov/archive/test-fn/1000/fermilab-fn-1010-e-ppd.pdf.

[43] C.-Y. Chen, J. Kozaczuk, and I. M. Lewis, "Non-resonant Collider Signatures of a Singlet-Driven Electroweak Phase Transition," *JHEP* **08** (2017) 096, arXiv:1704.05844 [hep-ph].

[44] X. Gan, A. J. Long, and L.-T. Wang, "Electroweak sphaleron with dimension-six operators," *Phys. Rev.* **D96** (2017) no. 11, 115018, arXiv:1708.03061 [hep-ph].

[45] Q.-H. Cao, F. P. Huang, K.-P. Xie, and X. Zhang, "Testing the electroweak phase transition in scalar extension models at lepton colliders," *Chin. Phys.* **C42** (2018) no. 2, 023103, arXiv:1708.04737 [hep-ph].

[46] B. Jain, S. J. Lee, and M. Son, "Validity of the effective potential and the precision of Higgs field self-couplings," *Phys. Rev.* **D98** (2018) no. 7, 075002, arXiv:1709.03232 [hep-ph].

[47] J. de Vries, M. Postma, J. van de Vis, and G. White, "Electroweak Baryogenesis and the Standard Model Effective Field Theory," *JHEP* **01** (2018) 089, arXiv:1710.04061 [hep-ph].

[48] M. Reichert, A. Eichhorn, H. Gies, J. M. Pawlowski, T. Plehn, and M. M. Scherer, "Probing baryogenesis through the Higgs boson self-coupling," *Phys. Rev.* **D97** (2018) no. 7, 075008, arXiv:1711.00019 [hep-ph].

[49] M. Carena, Z. Liu, and M. Riembau, "Probing the electroweak phase transition via enhanced di-Higgs boson production," *Phys. Rev.* **D97** (2018) no. 9, 095032, arXiv:1801.00794 [hep-ph].

[50] A. D. Sakharov, "Violation of CP Invariance, C asymmetry, and baryon asymmetry of the universe," *Pisma Zh. Eksp. Teor. Fiz.* **5** (1967) 32–35. [Usp. Fiz. Nauk161,no.5,61(1991)].

[51] A. Kosowsky, M. S. Turner, and R. Watkins, "Gravitational waves from first order cosmological phase transitions," *Phys. Rev. Lett.* **69** (1992) 2026–2029.

[52] A. D. Dolgov, D. Grasso, and A. Nicolis, "Relic backgrounds of gravitational waves from cosmic turbulence," *Phys. Rev.* **D66** (2002) 103505, arXiv:astro-ph/0206461 [astro-ph].

[53] M. Chala, V. V. Khoze, M. Spannowsky, and P. Waite, "Mapping the shape of the scalar potential with gravitational waves," arXiv:1905.00911 [hep-ph].

[54] R. Lafaye, T. Plehn, M. Rauch, D. Zerwas, and M. Duhrssen, "Measuring the Higgs Sector," *JHEP* **08** (2009) 009, arXiv:0904.3866 [hep-ph].

[55] **LHC Higgs Cross Section Working Group** Collaboration, A. David, A. Denner, M. Duehrssen, M. Grazzini, C. Grojean, G. Passarino, M. Schumacher, M. Spira, G. Weiglein, and M. Zanetti, "LHC HXSWG interim recommendations to explore the coupling structure of a Higgs-like particle," arXiv:1209.0040 [hep-ph].

[56] S. Weinberg, "Phenomenological Lagrangians," *Physica* **A96** (1979) no. 1-2, 327–340.

[57] C. N. Leung, S. T. Love, and S. Rao, "Low-Energy Manifestations of a New Interaction Scale: Operator Analysis," *Z. Phys.* **C31** (1986) 433.

[58] W. Buchmuller and D. Wyler, "Effective Lagrangian Analysis of New Interactions and Flavor Conservation," *Nucl. Phys.* **B268** (1986) 621–653.

[59] M. C. Gonzalez-Garcia, "Anomalous Higgs couplings," *Int. J. Mod. Phys.* **A14** (1999) 3121–3156, arXiv:hep-ph/9902321 [hep-ph].

[60] B. Grzadkowski, M. Iskrzynski, M. Misiak, and J. Rosiek, "Dimension-Six Terms in the Standard Model Lagrangian," *JHEP* **10** (2010) 085, arXiv:1008.4884 [hep-ph].

[61] G. Passarino, "NLO Inspired Effective Lagrangians for Higgs Physics," *Nucl. Phys.* **B868** (2013) 416–458, arXiv:1209.5538 [hep-ph].

[62] R. Lafaye, T. Plehn, M. Rauch, and D. Zerwas, "Measuring Supersymmetry," *Eur. Phys. J.* **C54** (2008) 617–644, arXiv:0709.3985 [hep-ph].

[63] T. Corbett, O. J. P. Eboli, D. Gonçalves, J. Gonzalez-Fraile, T. Plehn, and M. Rauch, "The Higgs Legacy of the LHC Run I," *JHEP* **08** (2015) 156, arXiv:1505.05516 [hep-ph].

[64] A. Butter, O. J. P. Éboli, J. Gonzalez-Fraile, M. C. Gonzalez-Garcia, T. Plehn, and M. Rauch, "The Gauge-Higgs Legacy of the LHC Run I," *JHEP* **07** (2016) 152, arXiv:1604.03105 [hep-ph].

[65] J. de Blas, J. C. Criado, M. Perez-Victoria, and J. Santiago, "Effective description of general extensions of the Standard Model: the complete tree-level dictionary," *JHEP* **03** (2018) 109, arXiv:1711.10391 [hep-ph].

[66] J. Ellis, C. W. Murphy, V. Sanz, and T. You, "Updated Global SMEFT Fit to Higgs, Diboson and Electroweak Data," *JHEP* **06** (2018) 146, arXiv:1803.03252 [hep-ph].

[67] S. Dawson, C. Englert, and T. Plehn, "Higgs Physics: It ain't over till it's over," arXiv:1808.01324 [hep-ph].

[68] J. Brehmer, *New Ideas for Effective Higgs Measurements*. PhD thesis, U. Heidelberg, 2017. http://www.thphys.uni-heidelberg.de/~plehn/includes/theses/brehmer_d.pdf.

[69] T. Corbett, *Effective Lagrangians for Higgs physics*. PhD thesis, Stony Brook U., 2015-04-30. http://graduate.physics.sunysb.edu/announ/theses/corbett-tyler-may-2015.pdf.

[70] S. L. Glashow, "Partial Symmetries of Weak Interactions," *Nucl. Phys.* **22** (1961) 579–588.

[71] A. Salam and J. C. Ward, "Electromagnetic and weak interactions," *Phys. Lett.* **13** (1964) 168–171.

[72] S. Weinberg, "A Model of Leptons," *Phys. Rev. Lett.* **19** (1967) 1264–1266.

[73] J. Goldstone, A. Salam, and S. Weinberg, "Broken Symmetries," *Phys. Rev.* **127** (1962) 965–970.

[74] Y. Nambu, "Axial vector current conservation in weak interactions," *Phys. Rev. Lett.* **4** (1960) 380–382.

[75] J. Goldstone, "Field Theories with Superconductor Solutions," *Nuovo Cim.* **19** (1961) 154–164.

[76] **LHC Higgs Cross Section Working Group** Collaboration, D. de Florian *et al.*, "Handbook of LHC Higgs Cross Sections: 4. Deciphering the Nature of the Higgs Sector," `arXiv:1610.07922 [hep-ph]`.

[77] R. Contino, A. Falkowski, F. Goertz, C. Grojean, and F. Riva, "On the Validity of the Effective Field Theory Approach to SM Precision Tests," *JHEP* **07** (2016) 144, `arXiv:1604.06444 [hep-ph]`.

[78] K. G. Wilson, "Renormalization group and critical phenomena. 1. Renormalization group and the Kadanoff scaling picture," *Phys. Rev.* **B4** (1971) 3174–3183.

[79] K. G. Wilson, "Renormalization group and critical phenomena. 2. Phase space cell analysis of critical behavior," *Phys. Rev.* **B4** (1971) 3184–3205.

[80] E. Fermi, "An attempt of a theory of beta radiation. 1.," *Z. Phys.* **88** (1934) 161–177.

[81] H. Georgi, *Weak Interactions and Modern Particle Theory.* 1984.

[82] J. F. Donoghue, E. Golowich, and B. R. Holstein, "Dynamics of the standard model," *Camb. Monogr. Part. Phys. Nucl. Phys. Cosmol.* **2** (1992) 1–540.

[83] A. De Rujula, M. B. Gavela, P. Hernandez, and E. Masso, "The Selfcouplings of vector bosons: Does LEP-1 obviate LEP-2?," *Nucl. Phys.* **B384** (1992) 3–58.

[84] K. Hagiwara, S. Ishihara, R. Szalapski, and D. Zeppenfeld, "Low-energy effects of new interactions in the electroweak boson sector," *Phys. Rev.* **D48** (1993) 2182–2203.

[85] K. Hagiwara, S. Matsumoto, and R. Szalapski, "Constraints on new physics in the electroweak bosonic sector from current data and future experiments," *Phys. Lett.* **B357** (1995) 411–418, `arXiv:hep-ph/9505322 [hep-ph]`.

[86] K. Hagiwara, T. Hatsukano, S. Ishihara, and R. Szalapski, "Probing nonstandard bosonic interactions via W boson pair production at lepton colliders," *Nucl. Phys.* **B496** (1997) 66–102, `arXiv:hep-ph/9612268 [hep-ph]`.

[87] G. F. Giudice, C. Grojean, A. Pomarol, and R. Rattazzi, "The Strongly-Interacting Light Higgs," *JHEP* **06** (2007) 045, `arXiv:hep-ph/0703164 [hep-ph]`.

[88] J. Elias-Miró, C. Grojean, R. S. Gupta, and D. Marzocca, "Scaling and tuning of EW and Higgs observables," *JHEP* **05** (2014) 019, `arXiv:1312.2928 [hep-ph]`.

[89] T. Corbett, O. J. P. Eboli, J. Gonzalez-Fraile, and M. C. Gonzalez-Garcia, "Constraining anomalous Higgs interactions," *Phys. Rev.* **D86** (2012) 075013, `arXiv:1207.1344 [hep-ph]`.

[90] T. Corbett, O. J. P. Eboli, J. Gonzalez-Fraile, and M. C. Gonzalez-Garcia, "Robust Determination of the Higgs Couplings: Power to the Data," *Phys. Rev.* **D87** (2013) 015022, `arXiv:1211.4580 [hep-ph]`.

[91] J. Brehmer, F. Kling, T. Plehn, and T. M. P. Tait, "Better Higgs-CP Tests Through Information Geometry," *Phys. Rev.* **D97** (2018) no. 9, 095017, arXiv:1712.02350 [hep-ph].

[92] F. U. Bernlochner, C. Englert, C. Hays, K. Lohwasser, H. Mildner, A. Pilkington, D. D. Price, and M. Spannowsky, "Angles on CP-violation in Higgs boson interactions," *Phys. Lett.* **B790** (2019) 372–379, arXiv:1808.06577 [hep-ph].

[93] G. F. Giudice, P. Paradisi, and M. Passera, "Testing new physics with the electron g-2," *JHEP* **11** (2012) 113, arXiv:1208.6583 [hep-ph].

[94] A. Buckley, C. Englert, J. Ferrando, D. J. Miller, L. Moore, M. Russell, and C. D. White, "Global fit of top quark effective theory to data," *Phys. Rev.* **D92** (2015) no. 9, 091501, arXiv:1506.08845 [hep-ph].

[95] **CDF, D0** Collaboration, T. Aaltonen *et al.*, "Combination of CDF and D0 measurements of the W boson helicity in top quark decays," *Phys. Rev.* **D85** (2012) 071106, arXiv:1202.5272 [hep-ex].

[96] T. Corbett, O. J. P. Eboli, D. Gonçalves, J. Gonzalez-Fraile, T. Plehn, and M. Rauch, "The Non-Linear Higgs Legacy of the LHC Run I," arXiv:1511.08188 [hep-ph].

[97] J. de Blas, O. Eberhardt, and C. Krause, "Current and Future Constraints on Higgs Couplings in the Nonlinear Effective Theory," *JHEP* **07** (2018) 048, arXiv:1803.00939 [hep-ph].

[98] M. E. Peskin and T. Takeuchi, "A New constraint on a strongly interacting Higgs sector," *Phys. Rev. Lett.* **65** (1990) 964–967.

[99] M. E. Peskin and T. Takeuchi, "Estimation of oblique electroweak corrections," *Phys. Rev.* **D46** (1992) 381–409.

[100] V. Cirigliano, J. Jenkins, and M. Gonzalez-Alonso, "Semileptonic decays of light quarks beyond the Standard Model," *Nucl. Phys.* **B830** (2010) 95–115, arXiv:0908.1754 [hep-ph].

[101] A. Falkowski, M. González-Alonso, and K. Mimouni, "Compilation of low-energy constraints on 4-fermion operators in the SMEFT," *JHEP* **08** (2017) 123, arXiv:1706.03783 [hep-ph].

[102] S. Alioli, V. Cirigliano, W. Dekens, J. de Vries, and E. Mereghetti, "Right-handed charged currents in the era of the Large Hadron Collider," *JHEP* **05** (2017) 086, arXiv:1703.04751 [hep-ph].

[103] E. da Silva Almeida, A. Alves, N. Rosa Agostinho, O. J. P. Éboli, and M. C. Gonzalez–Garcia, "Electroweak Sector Under Scrutiny: A Combined Analysis of LHC and Electroweak Precision Data," *Phys. Rev.* **D99** (2019) no. 3, 033001, arXiv:1812.01009 [hep-ph].

[104] T. Corbett, O. J. P. Éboli, and M. C. Gonzalez-Garcia, "Unitarity Constraints on Dimension-six Operators II: Including Fermionic Operators," *Phys. Rev.* **D96** (2017) no. 3, 035006, arXiv:1705.09294 [hep-ph].

[105] K. Hagiwara, R. D. Peccei, D. Zeppenfeld, and K. Hikasa, "Probing the Weak Boson Sector in e+ e- —> W+ W-," *Nucl. Phys.* **B282** (1987) 253–307.

[106] R. Alonso, M. B. Gavela, L. Merlo, S. Rigolin, and J. Yepes, "The Effective Chiral Lagrangian for a Light Dynamical "Higgs Particle"," *Phys. Lett.* **B722** (2013) 330–335, arXiv:1212.3305 [hep-ph]. [Erratum: Phys. Lett.B726,926(2013)].

[107] G. Buchalla, O. Catà, and C. Krause, "Complete Electroweak Chiral Lagrangian with a Light Higgs at NLO," *Nucl. Phys.* **B880** (2014) 552–573, arXiv:1307.5017 [hep-ph]. [Erratum: Nucl. Phys.B913,475(2016)].

[108] M. B. Gavela, J. Gonzalez-Fraile, M. C. Gonzalez-Garcia, L. Merlo, S. Rigolin, and J. Yepes, "CP violation with a dynamical Higgs," *JHEP* **10** (2014) 044, arXiv:1406.6367 [hep-ph].

[109] I. Brivio, J. Gonzalez-Fraile, M. C. Gonzalez-Garcia, and L. Merlo, "The complete HEFT Lagrangian after the LHC Run I," *Eur. Phys. J.* **C76** (2016) no. 7, 416, arXiv:1604.06801 [hep-ph].

[110] **SLD Electroweak Group, DELPHI, ALEPH, SLD, SLD Heavy Flavour Group, OPAL, LEP Electroweak Working Group, L3** Collaboration, S. Schael *et al.*, "Precision electroweak measurements on the Z resonance," *Phys. Rept.* **427** (2006) 257–454, arXiv:hep-ex/0509008 [hep-ex].

[111] **Particle Data Group** Collaboration, M. Tanabashi *et al.*, "Review of Particle Physics," *Phys. Rev.* **D98** (2018) no. 3, 030001.

[112] J. de Blas, M. Ciuchini, E. Franco, S. Mishima, M. Pierini, L. Reina, and L. Silvestrini, "The Global Electroweak and Higgs Fits in the LHC era," *PoS* **EPS-HEP2017** (2017) 467, arXiv:1710.05402 [hep-ph].

[113] D. Zeppenfeld, R. Kinnunen, A. Nikitenko, and E. Richter-Was, "Measuring Higgs boson couplings at the CERN LHC," *Phys. Rev.* **D62** (2000) 013009, arXiv:hep-ph/0002036 [hep-ph].

[114] M. Duhrssen, S. Heinemeyer, H. Logan, D. Rainwater, G. Weiglein, and D. Zeppenfeld, "Extracting Higgs boson couplings from CERN LHC data," *Phys. Rev.* **D70** (2004) 113009, arXiv:hep-ph/0406323 [hep-ph].

[115] A. Butter, *Global Fits for New Physics at the LHC and Beyond*. PhD thesis, U. Heidelberg, 2017. http://www.thphys.uni-heidelberg.de/~plehn/includes/theses/butter_d.pdf.

[116] K. Cranmer, "Practical Statistics for the LHC," in *Proceedings, 2011 European School of High-Energy Physics (ESHEP 2011): Cheile Gradistei, Romania, September 7-20, 2011*, pp. 267–308. 2015. arXiv:1503.07622 [physics.data-an].

[117] T. Plehn, "Lectures on LHC Physics," *Lect. Notes Phys.* **844** (2012) 1–193, arXiv:0910.4182 [hep-ph].

[118] G. Cowan, *Statistical data analysis*. 1998.

[119] J. Neyman and E. S. Pearson, "On the Problem of the Most Efficient Tests of Statistical Hypotheses," *Philosophical Transactions of the Royal Society of London* **A231** (1933) 289–337.

[120] G. Cowan, K. Cranmer, E. Gross, and O. Vitells, "Asymptotic formulae for likelihood-based tests of new physics," *Eur. Phys. J.* **C71** (2011) 1554, arXiv:1007.1727 [physics.data-an]. [Erratum: Eur. Phys. J.C73,2501(2013)].

[121] S. S. Wilks, "The Large-Sample Distribution of the Likelihood Ratio for Testing Composite Hypotheses," *Annals Math. Statist.* **9** (1938) no. 1, 60–62.

[122] A. Wald, "Tests of statistical hypotheses concerning several parameters when the number of observations is large," *Transactions of the American Mathematical Society* **54** (1943) no. 3, 426–482.

[123] W. Verkerke and D. P. Kirkby, "The RooFit toolkit for data modeling," *eConf* **C0303241** (2003) MOLT007, arXiv:physics/0306116 [physics].

[124] F. James and M. Winkler, "MINUIT User's Guide,".

[125] A. A. Markov, "Rasprostranenie zakona bol'shih chisel na velichiny, zavisyaschie drug ot druga," *Izvestiya Fiziko-matematicheskogo obschestva pri Kazanskom universitete* **15** (1906) no. 135-156, 18.

[126] B. C. Allanach and C. G. Lester, "Multi-dimensional mSUGRA likelihood maps," *Phys. Rev.* **D73** (2006) 015013, arXiv:hep-ph/0507283 [hep-ph].

[127] N. Metropolis, A. W. Rosenbluth, M. N. Rosenbluth, A. H. Teller, and E. Teller, "Equation of state calculations by fast computing machines," *The Journal of Chemical Physics* **21** (1953) no. 6, 1087–1092. http://link.aip.org/link/?JCP/21/1087/1.

[128] W. K. Hastings, "Monte carlo sampling methods using markov chains and their applications," *Biometrika* **57** (1970) no. 1, 97–109, http://biomet.oxfordjournals.org/cgi/reprint/57/1/97.pdf.

[129] A. Corana, M. Marchesi, C. Martini, and S. Ridella, "Minimizing Multimodal Functions of Continuous Variables with the "Simulated Annealing" Algorithm," *ACM Trans. Math. Softw.* **13** (1987) no. 3, 262–280. http://doi.acm.org/10.1145/29380.29864.

[130] M. Dittmar *et al.*, "Parton Distributions," arXiv:0901.2504 [hep-ph].

[131] J. Gao, L. Harland-Lang, and J. Rojo, "The Structure of the Proton in the LHC Precision Era," *Phys. Rept.* **742** (2018) 1–121, arXiv:1709.04922 [hep-ph].

[132] N. P. Hartland, F. Maltoni, E. R. Nocera, J. Rojo, E. Slade, E. Vryonidou, and C. Zhang, "A Monte Carlo global analysis of the Standard Model Effective Field Theory: the top quark sector," arXiv:1901.05965 [hep-ph].

[133] G. Arcadi, A. Djouadi, and M. Raidal, "Dark Matter through the Higgs portal," arXiv:1903.03616 [hep-ph].

[134] R. E. Shrock and M. Suzuki, "Invisible Decays of Higgs Bosons," *Phys. Lett.* **110B** (1982) 250.

[135] L.-F. Li, Y. Liu, and L. Wolfenstein, "HIDDEN HIGGS PARTICLES," *Phys. Lett.* **159B** (1985) 45–48.

[136] K. Griest and H. E. Haber, "Invisible Decays of Higgs Bosons in Supersymmetric Models," *Phys. Rev.* **D37** (1988) 719.

[137] M. C. Bento, O. Bertolami, and R. Rosenfeld, "Cosmological constraints on an invisibly decaying Higgs boson," *Phys. Lett.* **B518** (2001) 276–281, arXiv:hep-ph/0103340 [hep-ph].

[138] G. Belanger, B. Dumont, U. Ellwanger, J. F. Gunion, and S. Kraml, "Status of invisible Higgs decays," *Phys. Lett.* **B723** (2013) 340–347, arXiv:1302.5694 [hep-ph].

[139] V. Silveira and A. Zee, "Scalar Phatons," *Phys. Lett.* **161B** (1985) 136–140.

[140] J. McDonald, "Gauge singlet scalars as cold dark matter," *Phys. Rev.* **D50** (1994) 3637–3649, arXiv:hep-ph/0702143 [HEP-PH].

[141] C. P. Burgess, M. Pospelov, and T. ter Veldhuis, "The Minimal model of nonbaryonic dark matter: A Singlet scalar," *Nucl. Phys.* **B619** (2001) 709–728, arXiv:hep-ph/0011335 [hep-ph].

[142] Y. Mambrini, "Higgs searches and singlet scalar dark matter: Combined constraints from XENON 100 and the LHC," *Phys. Rev.* **D84** (2011) 115017, arXiv:1108.0671 [hep-ph].

[143] P. Athron, J. M. Cornell, F. Kahlhoefer, J. Mckay, P. Scott, and S. Wild, "Impact of vacuum stability, perturbativity and XENON1T on global fits of $\mathbb{Z}_2$ and $\mathbb{Z}_3$ scalar singlet dark matter," *Eur. Phys. J.* **C78** (2018) no. 10, 830, arXiv:1806.11281 [hep-ph].

[144] O. J. P. Eboli and D. Zeppenfeld, "Observing an invisible Higgs boson," *Phys. Lett.* **B495** (2000) 147–154, arXiv:hep-ph/0009158 [hep-ph].

[145] B. Di Girolamo and L. Neukermans, "Observing an invisibly decaying Higgs boson in ATLAS via vector boson fusion,".

[146] Y. Bai, P. Draper, and J. Shelton, "Measuring the Invisible Higgs Width at the 7 and 8 TeV LHC," *JHEP* **07** (2012) 192, arXiv:1112.4496 [hep-ph].

[147] D. Ghosh, R. Godbole, M. Guchait, K. Mohan, and D. Sengupta, "Looking for an Invisible Higgs Signal at the LHC," *Phys. Lett.* **B725** (2013) 344–351, arXiv:1211.7015 [hep-ph].

[148] C. Bernaciak, T. Plehn, P. Schichtel, and J. Tattersall, "Spying an invisible Higgs boson," *Phys. Rev.* **D91** (2015) 035024, arXiv:1411.7699 [hep-ph].

[149] R. Kleiss and W. J. Stirling, "Tagging the Higgs," *Phys. Lett.* **B200** (1988) 193–199.

[150] U. Baur and E. W. N. Glover, "Tagging the Higgs boson in p p —> W+ W- j j," *Phys. Lett.* **B252** (1990) 683–689.

[151] V. D. Barger, K.-m. Cheung, T. Han, J. Ohnemus, and D. Zeppenfeld, "A Comparative study of the benefits of forward jet tagging in heavy Higgs production at the SSC," *Phys. Rev.* **D44** (1991) 1426–1437.

[152] D. L. Rainwater, R. Szalapski, and D. Zeppenfeld, "Probing color singlet exchange in Z + two jet events at the CERN LHC," *Phys. Rev.* **D54** (1996) 6680–6689, arXiv:hep-ph/9605444 [hep-ph].

[153] B. E. Cox, J. R. Forshaw, and A. D. Pilkington, "Extracting Higgs boson couplings using a jet veto," *Phys. Lett.* **B696** (2011) 87–91, arXiv:1006.0986 [hep-ph].

[154] E. Gerwick, T. Plehn, and S. Schumann, "Understanding Jet Scaling and Jet Vetos in Higgs Searches," *Phys. Rev. Lett.* **108** (2012) 032003, arXiv:1108.3335 [hep-ph].

[155] C. Bernaciak, M. S. A. Buschmann, A. Butter, and T. Plehn, "Fox-Wolfram Moments in Higgs Physics," *Phys. Rev.* **D87** (2013) 073014, arXiv:1212.4436 [hep-ph].

[156] C. Bernaciak, B. Mellado, T. Plehn, P. Schichtel, and X. Ruan, "Improving Higgs plus Jets analyses through Fox–Wolfram Moments," *Phys. Rev.* **D89** (2014) no. 5, 053006, arXiv:1311.5891 [hep-ph].

[157] D. Choudhury and D. P. Roy, "Signatures of an invisibly decaying Higgs particle at LHC," *Phys. Lett.* **B322** (1994) 368–373, arXiv:hep-ph/9312347 [hep-ph].

[158] R. M. Godbole, M. Guchait, K. Mazumdar, S. Moretti, and D. P. Roy, "Search for 'invisible' Higgs signals at LHC via associated production with gauge bosons," *Phys. Lett.* **B571** (2003) 184–192, arXiv:hep-ph/0304137 [hep-ph].

[159] H. Davoudiasl, T. Han, and H. E. Logan, "Discovering an invisibly decaying Higgs at hadron colliders," *Phys. Rev.* **D71** (2005) 115007, arXiv:hep-ph/0412269 [hep-ph].

[160] H. Okawa, J. Kunkle, and E. Lipeles, "Prospects on the search for invisible Higgs decays in the ZH channel at the LHC and HL-LHC: A Snowmass White Paper," in *Proceedings, 2013 Community Summer Study on the Future of U.S. Particle Physics: Snowmass on the Mississippi (CSS2013): Minneapolis, MN, USA, July 29-August 6, 2013*. 2013. arXiv:1309.7925 [hep-ex]. http://www.slac.stanford.edu/econf/C1307292/docs/submittedArxivFiles/1309.7925.pdf.

[161] D. Gonçalves, F. Krauss, S. Kuttimalai, and P. Maierhöfer, "Boosting invisible searches via ZH : From the Higgs boson to dark matter simplified models," *Phys. Rev.* **D94** (2016) no. 5, 053014, arXiv:1605.08039 [hep-ph].

[162] J. F. Gunion, "Detecting an invisibly decaying Higgs boson at a hadron supercollider," *Phys. Rev. Lett.* **72** (1994) 199–202, arXiv:hep-ph/9309216 [hep-ph].

[163] N. Zhou, Z. Khechadoorian, D. Whiteson, and T. M. P. Tait, "Bounds on Invisible Higgs boson Decays from $t\bar{t}H$ Production," *Phys. Rev. Lett.* **113** (2014) 151801, arXiv:1408.0011 [hep-ph]. [Erratum: Phys. Rev. Lett.114,no.22,229901(2015)].

[164] M. R. Buckley and D. Gonçalves, "Constraining the Strength and CP Structure of Dark Production at the LHC: the Associated Top-Pair Channel," *Phys. Rev.* **D93** (2016) no. 3, 034003, arXiv:1511.06451 [hep-ph].

[165] **CMS** Collaboration, A. M. Sirunyan *et al.*, "Search for invisible decays of a Higgs boson produced through vector boson fusion in proton-proton collisions at $\sqrt{s} = 13$ TeV," arXiv:1809.05937 [hep-ex].

[166] **CMS** Collaboration, V. Khachatryan *et al.*, "Search for invisible Higgs bosons in $\mathrm{pp} \to \mathrm{ZH} \to 2\ell + E_{\mathrm{T}}^{\mathrm{miss}}$ channels at $\sqrt{s} = 13$ TeV,".

[167] **CMS** Collaboration, S. Chatrchyan *et al.*, "Search for invisible decays of Higgs bosons in the vector boson fusion and associated ZH production modes," *Eur. Phys. J.* **C74** (2014) 2980, arXiv:1404.1344 [hep-ex].

[168] **CMS** Collaboration, V. Khachatryan *et al.*, "Searches for invisible decays of the Higgs boson in pp collisions at $\sqrt{s} = 7$, 8, and 13 TeV," *JHEP* **02** (2017) 135, arXiv:1610.09218 [hep-ex].

[169] **CMS** Collaboration, V. Khachatryan *et al.*, "First constraints on invisible Higgs boson decays using $\mathrm{t\bar{t}H}$ production at $\sqrt{s} = 13$ TeV," Tech. Rep. CMS-PAS-HIG-18-008, CERN, Geneva, 2019. https://cds.cern.ch/record/2668677.

[170] **ATLAS** Collaboration, G. Aad *et al.*, "Search for invisible decays of a Higgs boson using vector-boson fusion in *pp* collisions at $\sqrt{s} = 8$ TeV with the ATLAS detector," *JHEP* **01** (2016) 172, arXiv:1508.07869 [hep-ex].

[171] **ATLAS** Collaboration, M. Aaboud *et al.*, "Search for invisible Higgs boson decays in vector boson fusion at $\sqrt{s} = 13$ TeV with the ATLAS detector," arXiv:1809.06682 [hep-ex].

[172] **ATLAS** Collaboration, G. Aad *et al.*, "Search for Invisible Decays of a Higgs Boson Produced in Association with a Z Boson in ATLAS," *Phys. Rev. Lett.* **112** (2014) 201802, arXiv:1402.3244 [hep-ex].

[173] **ATLAS** Collaboration, G. Aad *et al.*, "Search for invisible decays of the Higgs boson produced in association with a hadronically decaying vector boson in *pp* collisions at $\sqrt{s} = 8$ TeV with the ATLAS detector," *Eur. Phys. J.* **C75** (2015) no. 7, 337, arXiv:1504.04324 [hep-ex].

[174] **ATLAS** Collaboration, M. Aaboud *et al.*, "Search for an invisibly decaying Higgs boson or dark matter candidates produced in association with a Z boson in *pp* collisions at $\sqrt{s} = 13$ TeV with the ATLAS detector," *Phys. Lett.* **B776** (2018) 318–337, arXiv:1708.09624 [hep-ex].

[175] **ATLAS** Collaboration, G. Aad *et al.*, "Constraints on new phenomena via Higgs boson couplings and invisible decays with the ATLAS detector," *JHEP* **11** (2015) 206, arXiv:1509.00672 [hep-ex].

[176] **ATLAS** Collaboration, M. Aaboud *et al.*, "Combination of searches for invisible Higgs boson decays with the ATLAS experiment," *Submitted to: Phys. Rev. Lett.* (2019) , arXiv:1904.05105 [hep-ex].

[177] D. Gonçalves, T. Plehn, and J. M. Thompson, "Weak boson fusion at 100 TeV," *Phys. Rev.* **D95** (2017) no. 9, 095011, arXiv:1702.05098 [hep-ph].

[178] V. V. Khoze, G. Ro, and M. Spannowsky, "Spectroscopy of scalar mediators to dark matter at the LHC and at 100 TeV," *Phys. Rev.* **D92** (2015) no. 7, 075006, arXiv:1505.03019 [hep-ph].

[179] T. Gleisberg, S. Hoeche, F. Krauss, M. Schonherr, S. Schumann, F. Siegert, and J. Winter, "Event generation with SHERPA 1.1," *JHEP* **02** (2009) 007, arXiv:0811.4622 [hep-ph].

[180] S. Catani, F. Krauss, R. Kuhn, and B. R. Webber, "QCD matrix elements + parton showers," *JHEP* **11** (2001) 063, arXiv:hep-ph/0109231 [hep-ph].

[181] T. Gleisberg and S. Hoeche, "Comix, a new matrix element generator," *JHEP* **12** (2008) 039, arXiv:0808.3674 [hep-ph].

[182] C.-H. Chan, K. Cheung, Y.-L. Chung, and P.-H. Hsu, "Vector Boson Fusion versus Gluon Fusion," *Phys. Rev.* **D96** (2017) no. 9, 096009, arXiv:1706.02864 [hep-ph].

[183] A. Denner and S. Dittmaier, "Reduction of one loop tensor five point integrals," *Nucl. Phys.* **B658** (2003) 175–202, arXiv:hep-ph/0212259 [hep-ph].

[184] A. Denner and S. Dittmaier, "Reduction schemes for one-loop tensor integrals," *Nucl. Phys.* **B734** (2006) 62–115, arXiv:hep-ph/0509141 [hep-ph].

[185] G. Ossola, C. G. Papadopoulos, and R. Pittau, "CutTools: A Program implementing the OPP reduction method to compute one-loop amplitudes," *JHEP* **03** (2008) 042, arXiv:0711.3596 [hep-ph].

[186] A. van Hameren, "OneLOop: For the evaluation of one-loop scalar functions," *Comput. Phys. Commun.* **182** (2011) 2427–2438, arXiv:1007.4716 [hep-ph].

[187] A. Denner and S. Dittmaier, "Scalar one-loop 4-point integrals," *Nucl. Phys.* **B844** (2011) 199–242, arXiv:1005.2076 [hep-ph].

[188] F. Cascioli, P. Maierhofer, and S. Pozzorini, "Scattering Amplitudes with Open Loops," *Phys. Rev. Lett.* **108** (2012) 111601, arXiv:1111.5206 [hep-ph].

[189] A. Denner, S. Dittmaier, and L. Hofer, "Collier: a fortran-based Complex One-Loop LIbrary in Extended Regularizations," *Comput. Phys. Commun.* **212** (2017) 220–238, arXiv:1604.06792 [hep-ph].

[190] M. Cacciari and G. P. Salam, "Dispelling the N^3 myth for the k_t jet-finder," *Phys. Lett.* **B641** (2006) 57–61, arXiv:hep-ph/0512210 [hep-ph].

[191] M. Cacciari, G. P. Salam, and G. Soyez, "The Anti-k(t) jet clustering algorithm," *JHEP* **04** (2008) 063, arXiv:0802.1189 [hep-ph].

[192] M. Cacciari, G. P. Salam, and G. Soyez, "FastJet User Manual," *Eur. Phys. J.* **C72** (2012) 1896, arXiv:1111.6097 [hep-ph].

[193] **DELPHES 3** Collaboration, J. de Favereau, C. Delaere, P. Demin, A. Giammanco, V. Lemaître, A. Mertens, and M. Selvaggi, "DELPHES 3, A modular framework for fast simulation of a generic collider experiment," *JHEP* **02** (2014) 057, arXiv:1307.6346 [hep-ex].

[194] **ATLAS** Collaboration, G. Aad *et al.*, "Electron efficiency measurements with the ATLAS detector using the 2015 LHC proton-proton collision data,".

[195] **ATLAS** Collaboration, G. Aad *et al.*, "Muon reconstruction performance of the ATLAS detector in proton-proton collision data at $\sqrt{s}$ =13 TeV," *Eur. Phys. J.* **C76** (2016) no. 5, 292, arXiv:1603.05598 [hep-ex].

[196] M. Rauch and D. Zeppenfeld, "Jet clustering dependence of Higgs boson production in vector-boson fusion," *Phys. Rev.* **D95** (2017) no. 11, 114015, arXiv:1703.05676 [hep-ph].

[197] S. Catani, G. Turnock, and B. R. Webber, "Jet broadening measures in e^+e^- annihilation," *Phys. Lett.* **B295** (1992) 269–276.

[198] C. F. Berger, T. Kucs, and G. F. Sterman, "Event shape / energy flow correlations," *Phys. Rev.* **D68** (2003) 014012, arXiv:hep-ph/0303051 [hep-ph].

[199] J. Gallicchio and M. D. Schwartz, "Quark and Gluon Tagging at the LHC," *Phys. Rev. Lett.* **107** (2011) 172001, arXiv:1106.3076 [hep-ph].

[200] P. T. Komiske, E. M. Metodiev, and M. D. Schwartz, "Deep learning in color: towards automated quark/gluon jet discrimination," *JHEP* **01** (2017) 110, arXiv:1612.01551 [hep-ph].

[201] Z.-B. Kang, F. Ringer, and W. J. Waalewijn, "The Energy Distribution of Subjets and the Jet Shape," *JHEP* **07** (2017) 064, arXiv:1705.05375 [hep-ph].

[202] V. Rentala, N. Vignaroli, H.-n. Li, Z. Li, and C. P. Yuan, "Discriminating Higgs production mechanisms using jet energy profiles," *Phys. Rev.* **D88** (2013) no. 7, 073007, arXiv:1306.0899 [hep-ph].

[203] G. Altarelli and G. Parisi, "Asymptotic Freedom in Parton Language," *Nucl. Phys.* **B126** (1977) 298–318.

[204] J. Pumplin, "How to tell quark jets from gluon jets," *Phys. Rev.* **D44** (1991) 2025–2032.

[205] A. J. Larkoski, G. P. Salam, and J. Thaler, "Energy Correlation Functions for Jet Substructure," *JHEP* **06** (2013) 108, arXiv:1305.0007 [hep-ph].

[206] D. Krohn, M. D. Schwartz, T. Lin, and W. J. Waalewijn, "Jet Charge at the LHC," *Phys. Rev. Lett.* **110** (2013) no. 21, 212001, arXiv:1209.2421 [hep-ph].

[207] **CMS** Collaboration, CMS, "Performance of quark/gluon discrimination in 8 TeV pp data,".

[208] A. Hocker *et al.*, "TMVA - Toolkit for Multivariate Data Analysis," arXiv:physics/0703039 [physics.data-an].

[209] I. Antcheva *et al.*, "ROOT: A C++ framework for petabyte data storage, statistical analysis and visualization," *Comput. Phys. Commun.* **182** (2011) 1384–1385.

[210] Y. Freund and R. E. Schapire, "A Decision-Theoretic Generalization of On-Line Learning and an Application to Boosting," *J. Comput. Syst. Sci.* **55** (1997) no. 1, 119–139.

[211] A. L. Read, "Presentation of search results: The CL(s) technique," *J. Phys.* **G28** (2002) 2693–2704.

[212] D. Dercks, N. Desai, J. S. Kim, K. Rolbiecki, J. Tattersall, and T. Weber, "CheckMATE 2: From the model to the limit," *Comput. Phys. Commun.* **221** (2017) 383–418, arXiv:1611.09856 [hep-ph].

[213] E. H. Simmons, "Dimension-six Gluon Operators as Probes of New Physics," *Phys. Lett.* **B226** (1989) 132–136.

[214] H. K. Dreiner, A. Duff, and D. Zeppenfeld, "How well do we know the three gluon vertex?," *Phys. Lett.* **B282** (1992) 441–447.

[215] L. J. Dixon and Y. Shadmi, "Testing gluon selfinteractions in three jet events at hadron colliders," *Nucl. Phys.* **B423** (1994) 3–32, arXiv:hep-ph/9312363 [hep-ph]. [Erratum: Nucl. Phys.B452,724(1995)].

[216] P. L. Cho and E. H. Simmons, "Searching for G3 in $t\bar{t}$ production," *Phys. Rev.* **D51** (1995) 2360–2370, arXiv:hep-ph/9408206 [hep-ph].

[217] S. Alioli, M. Farina, D. Pappadopulo, and J. T. Ruderman, "Precision Probes of QCD at High Energies," *JHEP* **07** (2017) 097, arXiv:1706.03068 [hep-ph].

[218] V. Hirschi, F. Maltoni, I. Tsinikos, and E. Vryonidou, "Constraining anomalous gluon self-interactions at the LHC: a reappraisal," *JHEP* **07** (2018) 093, arXiv:1806.04696 [hep-ph].

[219] F. Krauss, S. Kuttimalai, and T. Plehn, "LHC multijet events as a probe for anomalous dimension-six gluon interactions," *Phys. Rev.* **D95** (2017) no. 3, 035024, arXiv:1611.00767 [hep-ph].

[220] A. Buckley, C. Englert, J. Ferrando, D. J. Miller, L. Moore, M. Russell, and C. D. White, "Constraining top quark effective theory in the LHC Run II era," *JHEP* **04** (2016) 015, arXiv:1512.03360 [hep-ph].

[221] C. Zhang and S. Willenbrock, "Effective-Field-Theory Approach to Top-Quark Production and Decay," *Phys. Rev.* **D83** (2011) 034006, arXiv:1008.3869 [hep-ph].

[222] C. Zhang, "Constraining *qqtt* operators from four-top production: a case for enhanced EFT sensitivity," *Chin. Phys.* **C42** (2018) no. 2, 023104, arXiv:1708.05928 [hep-ph].

[223] C. Degrande, F. Maltoni, K. Mimasu, E. Vryonidou, and C. Zhang, "Single-top associated production with a Z or H boson at the LHC: the SMEFT interpretation," *JHEP* **10** (2018) 005, arXiv:1804.07773 [hep-ph].

[224] M. Chala, J. Santiago, and M. Spannowsky, "Constraining four-fermion operators using rare top decays," arXiv:1809.09624 [hep-ph].

[225] J. Aebischer, J. Kumar, P. Stangl, and D. M. Straub, "A Global Likelihood for Precision Constraints and Flavour Anomalies," arXiv:1810.07698 [hep-ph].

[226] E. Massó and V. Sanz, "Limits on anomalous couplings of the Higgs boson to electroweak gauge bosons from LEP and the LHC," *Phys. Rev.* **D87** (2013) no. 3, 033001, arXiv:1211.1320 [hep-ph].

[227] A. Falkowski, M. Gonzalez-Alonso, A. Greljo, and D. Marzocca, "Global constraints on anomalous triple gauge couplings in effective field theory approach," *Phys. Rev. Lett.* **116** (2016) no. 1, 011801, arXiv:1508.00581 [hep-ph].

[228] G. Brooijmans *et al.*, "Les Houches 2013: Physics at TeV Colliders: New Physics Working Group Report," arXiv:1405.1617 [hep-ph].

[229] M. Trott, "On the consistent use of Constructed Observables," *JHEP* **02** (2015) 046, arXiv:1409.7605 [hep-ph].

[230] A. Falkowski and F. Riva, "Model-independent precision constraints on dimension-6 operators," *JHEP* **02** (2015) 039, arXiv:1411.0669 [hep-ph].

[231] T. Corbett, O. J. P. Éboli, J. Gonzalez-Fraile, and M. C. Gonzalez-Garcia, "Determining Triple Gauge Boson Couplings from Higgs Data," *Phys. Rev. Lett.* **111** (2013) 011801, arXiv:1304.1151 [hep-ph].

[232] J. Ellis, V. Sanz, and T. You, "The Effective Standard Model after LHC Run I," *JHEP* **03** (2015) 157, arXiv:1410.7703 [hep-ph].

[233] A. Falkowski, M. Gonzalez-Alonso, A. Greljo, D. Marzocca, and M. Son, "Anomalous Triple Gauge Couplings in the Effective Field Theory Approach at the LHC," *JHEP* **02** (2017) 115, arXiv:1609.06312 [hep-ph].

[234] A. Azatov, J. Elias-Miro, Y. Reyimuaji, and E. Venturini, "Novel measurements of anomalous triple gauge couplings for the LHC," *JHEP* **10** (2017) 027, arXiv:1707.08060 [hep-ph].

[235] R. Franceschini, G. Panico, A. Pomarol, F. Riva, and A. Wulzer, "Electroweak Precision Tests in High-Energy Diboson Processes," *JHEP* **02** (2018) 111, arXiv:1712.01310 [hep-ph].

[236] D. Liu and L.-T. Wang, "Precision Measurement with Diboson at the LHC," arXiv:1804.08688 [hep-ph].

[237] M. Klute, R. Lafaye, T. Plehn, M. Rauch, and D. Zerwas, "Measuring Higgs Couplings from LHC Data," *Phys. Rev. Lett.* **109** (2012) 101801, arXiv:1205.2699 [hep-ph].

[238] T. Plehn and M. Rauch, "Higgs Couplings after the Discovery," *EPL* **100** (2012) no. 1, 11002, arXiv:1207.6108 [hep-ph].

[239] M. Farina, G. Panico, D. Pappadopulo, J. T. Ruderman, R. Torre, and A. Wulzer, "Energy helps accuracy: electroweak precision tests at hadron colliders," *Phys. Lett.* **B772** (2017) 210–215, arXiv:1609.08157 [hep-ph].

[240] C. Grojean, M. Montull, and M. Riembau, "Diboson at the LHC vs LEP," *JHEP* **03** (2019) 020, arXiv:1810.05149 [hep-ph].

[241] Z. Zhang, "Time to Go Beyond Triple-Gauge-Boson-Coupling Interpretation of W Pair Production," *Phys. Rev. Lett.* **118** (2017) no. 1, 011803, arXiv:1610.01618 [hep-ph].

[242] J. Baglio, S. Dawson, and I. M. Lewis, "An NLO QCD effective field theory analysis of W^+W^- production at the LHC including fermionic operators," *Phys. Rev.* **D96** (2017) no. 7, 073003, arXiv:1708.03332 [hep-ph].

[243] J. Baglio, S. Dawson, and I. M. Lewis, "NLO effects in EFT fits to W^+W^- production at the LHC," *Phys. Rev.* **D99** (2019) no. 3, 035029, arXiv:1812.00214 [hep-ph].

[244] A. Alves, N. Rosa-Agostinho, O. J. P. Éboli, and M. C. Gonzalez-Garcia, "Effect of Fermionic Operators on the Gauge Legacy of the LHC Run I," *Phys. Rev.* **D98** (2018) no. 1, 013006, arXiv:1805.11108 [hep-ph].

[245] S. Dawson and A. Ismail, "Standard model EFT corrections to Z boson decays," *Phys. Rev.* **D98** (2018) no. 9, 093003, arXiv:1808.05948 [hep-ph].

[246] S. Di Vita, C. Grojean, G. Panico, M. Riembau, and T. Vantalon, "A global view on the Higgs self-coupling," *JHEP* **09** (2017) 069, arXiv:1704.01953 [hep-ph].

[247] S. Homiller and P. Meade, "Measurement of the Triple Higgs Coupling at a HE-LHC," arXiv:1811.02572 [hep-ph].

[248] J. Chang, K. Cheung, J. S. Lee, C.-T. Lu, and J. Park, "Higgs-boson-pair production $H(\to b\bar{b})H(\to \gamma\gamma)$ from gluon fusion at the HL-LHC and HL-100 TeV hadron collider," arXiv:1804.07130 [hep-ph].

[249] S. Borowka, C. Duhr, F. Maltoni, D. Pagani, A. Shivaji, and X. Zhao, "Probing the scalar potential via double Higgs boson production at hadron colliders," *Submitted to: JHEP* (2018) , arXiv:1811.12366 [hep-ph].

[250] D. Ghosh and M. Wiebusch, "Dimension-six triple gluon operator in Higgs+jet observables," *Phys. Rev.* **D91** (2015) no. 3, 031701, arXiv:1411.2029 [hep-ph].

[251] F. Maltoni, E. Vryonidou, and C. Zhang, "Higgs production in association with a top-antitop pair in the Standard Model Effective Field Theory at NLO in QCD," *JHEP* **10** (2016) 123, arXiv:1607.05330 [hep-ph].

[252] E. Vryonidou and C. Zhang, "Dimension-six electroweak top-loop effects in Higgs production and decay," *JHEP* **08** (2018) 036, arXiv:1804.09766 [hep-ph].

[253] **CMS** Collaboration, A. M. Sirunyan *et al.*, "Search for $\mathrm{t\bar{t}H}$ production in the all-jet final state in proton-proton collisions at $\sqrt{s} = 13$ TeV," *JHEP* **06** (2018) 101, arXiv:1803.06986 [hep-ex].

[254] J. Alwall, R. Frederix, S. Frixione, V. Hirschi, F. Maltoni, O. Mattelaer, H. S. Shao, T. Stelzer, P. Torrielli, and M. Zaro, "The automated computation of tree-level and next-to-leading order differential cross sections, and their matching to parton shower simulations," *JHEP* **07** (2014) 079, arXiv:1405.0301 [hep-ph].

[255] T. Sjostrand, S. Mrenna, and P. Z. Skands, "PYTHIA 6.4 Physics and Manual," *JHEP* **05** (2006) 026, arXiv:hep-ph/0603175 [hep-ph].

[256] **ATLAS** Collaboration, M. Aaboud *et al.*, "Observation of Higgs boson production in association with a top quark pair at the LHC with the ATLAS detector," *Phys. Lett.* **B784** (2018) 173–191, arXiv:1806.00425 [hep-ex].

[257] **ATLAS** Collaboration, M. Aaboud *et al.*, "Measurements of the $t\bar{t}$ production cross-section in the dilepton and lepton-plus-jets channels and of the ratio of the $t\bar{t}$ and Z boson cross-sections in pp collisions at $\sqrt{s} = 13$ TeV with the ATLAS detector,".

[258] S. Biswas, R. Frederix, E. Gabrielli, and B. Mele, "Enhancing the $t\bar{t}H$ signal through top-quark spin polarization effects at the LHC," *JHEP* **07** (2014) 020, arXiv:1403.1790 [hep-ph].

[259] **ATLAS** Collaboration, M. Aaboud *et al.*, "Measurement of gluon fusion and vector boson fusion Higgs boson production cross-sections in the $H \to WW^* \to e\nu\mu\nu$ decay channel in pp collisions at $\sqrt{s} = 13$ TeV with the ATLAS detector,".

[260] **ATLAS** Collaboration, M. Aaboud *et al.*, "Evidence for the associated production of the Higgs boson and a top quark pair with the ATLAS detector," *Phys. Rev.* **D97** (2018) no. 7, 072003, arXiv:1712.08891 [hep-ex].

[261] **CMS** Collaboration, A. M. Sirunyan *et al.*, "Measurements of properties of the Higgs boson decaying to a W boson pair in pp collisions at $\sqrt{s} = 13$ TeV," *Phys. Lett.* **B791** (2019) 96, arXiv:1806.05246 [hep-ex].

[262] **CMS** Collaboration, V. Khachatryan *et al.*, "Search for Higgs boson production in association with top quarks in multilepton final states at $\sqrt{s} = 13$ TeV,".

[263] **CMS** Collaboration, A. M. Sirunyan *et al.*, "Evidence for associated production of a Higgs boson with a top quark pair in final states with electrons, muons, and hadronically decaying τ leptons at $\sqrt{s} = 13$ TeV," *JHEP* **08** (2018) 066, arXiv:1803.05485 [hep-ex].

[264] **ATLAS** Collaboration, M. Aaboud *et al.*, "Measurement of the Higgs boson coupling properties in the $H \to ZZ^* \to 4\ell$ decay channel at $\sqrt{s} = 13$ TeV with the ATLAS detector," *JHEP* **03** (2018) 095, arXiv:1712.02304 [hep-ex].

[265] **CMS** Collaboration, A. M. Sirunyan *et al.*, "Measurements of properties of the Higgs boson decaying into the four-lepton final state in pp collisions at $\sqrt{s} = 13$ TeV," *JHEP* **11** (2017) 047, arXiv:1706.09936 [hep-ex].

[266] **CMS** Collaboration, V. Khachatryan *et al.*, "Measurements of properties of the Higgs boson in the four-lepton final state at $\sqrt{s} = 13$ TeV,".

[267] **ATLAS** Collaboration, M. Aaboud *et al.*, "Measurements of Higgs boson properties in the diphoton decay channel with 36 fb^{-1} of pp collision data at $\sqrt{s} = 13$ TeV with the ATLAS detector," *Phys. Rev.* **D98** (2018) 052005, arXiv:1802.04146 [hep-ex].

[268] **CMS** Collaboration, A. M. Sirunyan *et al.*, "Measurements of Higgs boson properties in the diphoton decay channel in proton-proton collisions at $\sqrt{s} = 13$ TeV," *JHEP* **11** (2018) 185, arXiv:1804.02716 [hep-ex].

[269] **CMS** Collaboration, A. M. Sirunyan *et al.*, "Observation of the Higgs boson decay to a pair of τ leptons with the CMS detector," *Phys. Lett.* **B779** (2018) 283–316, arXiv:1708.00373 [hep-ex].

[270] **ATLAS** Collaboration, M. Aaboud *et al.*, "Searches for the $Z\gamma$ decay mode of the Higgs boson and for new high-mass resonances in pp collisions at $\sqrt{s} = 13$ TeV with the ATLAS detector," *JHEP* **10** (2017) 112, arXiv:1708.00212 [hep-ex].

[271] **CMS** Collaboration, A. M. Sirunyan *et al.*, "Search for the decay of a Higgs boson in the $\ell\ell\gamma$ channel in proton-proton collisions at $\sqrt{s} = 13$ TeV," *JHEP* **11** (2018) 152, arXiv:1806.05996 [hep-ex].

[272] **CMS** Collaboration, V. Khachatryan *et al.*, "Search for invisible decays of the Higgs boson produced through vector boson fusion at $\sqrt{s} = 13$ TeV,".

[273] **ATLAS** Collaboration, M. Aaboud *et al.*, "Evidence for the $H \to b\bar{b}$ decay with the ATLAS detector," *JHEP* **12** (2017) 024, arXiv:1708.03299 [hep-ex].

[274] **CMS** Collaboration, A. M. Sirunyan *et al.*, "Evidence for the Higgs boson decay to a bottom quark-antiquark pair," *Phys. Lett.* **B780** (2018) 501–532, arXiv:1709.07497 [hep-ex].

[275] **CMS** Collaboration, V. Khachatryan *et al.*, "Search for the standard model Higgs boson decaying to a pair of τ leptons and produced in association with a W or a Z boson in proton-proton collisions at $\sqrt{s} = 13$ TeV,".

[276] **CMS** Collaboration, A. M. Sirunyan *et al.*, "Search for new physics in events with a leptonically decaying Z boson and a large transverse momentum imbalance in proton-proton collisions at $\sqrt{s} = 13$ TeV," *Eur. Phys. J.* **C78** (2018) no. 4, 291, arXiv:1711.00431 [hep-ex].

[277] **ATLAS** Collaboration, M. Aaboud *et al.*, "Search for heavy resonances decaying into a W or Z boson and a Higgs boson in final states with leptons and b-jets in 36 fb^{-1} of $\sqrt{s} = 13$ TeV pp collisions with the ATLAS detector," *JHEP* **03** (2018) 174, arXiv:1712.06518 [hep-ex]. [Erratum: JHEP11,051(2018)].

[278] **ATLAS** Collaboration, M. Aaboud *et al.*, "Search for the standard model Higgs boson produced in association with top quarks and decaying into a $b\bar{b}$ pair in pp collisions at $\sqrt{s} = 13$ TeV with the ATLAS detector," *Phys. Rev.* **D97** (2018) no. 7, 072016, arXiv:1712.08895 [hep-ex].

[279] **CMS** Collaboration, A. M. Sirunyan *et al.*, "Search for $\mathrm{t\bar{t}H}$ production in the $\mathrm{H} \to \mathrm{b\bar{b}}$ decay channel with leptonic $\mathrm{t\bar{t}}$ decays in proton-proton collisions at $\sqrt{s} = 13$ TeV," *JHEP* **03** (2019) 026, arXiv:1804.03682 [hep-ex].

[280] N. D. Christensen and C. Duhr, "FeynRules - Feynman rules made easy," *Comput. Phys. Commun.* **180** (2009) 1614–1641, arXiv:0806.4194 [hep-ph].

[281] S. Dawson. Private communication.

[282] M. Chiesa, A. Denner, and J.-N. Lang, "Anomalous triple-gauge-boson interactions in vector-boson pair production with RECOLA2," *Eur. Phys. J.* **C78** (2018) no. 6, 467, arXiv:1804.01477 [hep-ph].

[283] R. Contino, M. Ghezzi, C. Grojean, M. Mühlleitner, and M. Spira, "eHDECAY: an Implementation of the Higgs Effective Lagrangian into HDECAY," *Comput. Phys. Commun.* **185** (2014) 3412–3423, arXiv:1403.3381 [hep-ph].

[284] J. Brehmer, K. Cranmer, F. Kling, and T. Plehn, "Better Higgs boson measurements through information geometry," *Phys. Rev.* **D95** (2017) no. 7, 073002, arXiv:1612.05261 [hep-ph].

[285] **ATLAS** Collaboration, G. Aad *et al.*, "Measurement of total and differential W^+W^- production cross sections in proton-proton collisions at $\sqrt{s} = 8$ TeV with the ATLAS detector and limits on anomalous triple-gauge-boson couplings," *JHEP* **09** (2016) 029, arXiv:1603.01702 [hep-ex].

[286] **CMS** Collaboration, V. Khachatryan *et al.*, "Measurement of the $\mathrm{W^+W^-}$ cross section in pp collisions at $\sqrt{s} = 8$ TeV and limits on anomalous gauge couplings," *Eur. Phys. J.* **C76** (2016) no. 7, 401, arXiv:1507.03268 [hep-ex].

[287] **ATLAS** Collaboration, G. Aad *et al.*, "Measurements of $W^{\pm}Z$ production cross sections in pp collisions at $\sqrt{s} = 8$ TeV with the ATLAS detector and limits on anomalous gauge boson self-couplings," *Phys. Rev.* **D93** (2016) no. 9, 092004, arXiv:1603.02151 [hep-ex].

[288] **CMS** Collaboration, V. Khachatryan *et al.*, "Measurement of the WZ production cross section in pp collisions at $\sqrt{s} = 7$ and 8 TeV and search for anomalous triple gauge couplings at $\sqrt{s} = 8$ TeV," *Eur. Phys. J.* **C77** (2017) no. 4, 236, arXiv:1609.05721 [hep-ex].

[289] **ATLAS** Collaboration, M. Aaboud *et al.*, "Measurement of $W^{\pm}Z$ production cross sections and gauge boson polarisation in pp collisions at $\sqrt{s} = 13$ TeV with the ATLAS detector,".

[290] A. Helset and M. Trott, "On interference and non-interference in the SMEFT," *JHEP* **04** (2018) 038, arXiv:1711.07954 [hep-ph].

[291] C. Hays, A. Martin, V. Sanz, and J. Setford, "On the impact of dimension-eight SMEFT operators on Higgs measurements," *JHEP* **02** (2019) 123, arXiv:1808.00442 [hep-ph].

[292] A. Biekötter, J. Brehmer, and T. Plehn, "Extending the limits of Higgs effective theory," *Phys. Rev.* **D94** (2016) no. 5, 055032, arXiv:1602.05202 [hep-ph].

[293] S. Banerjee, C. Englert, R. S. Gupta, and M. Spannowsky, "Probing Electroweak Precision Physics via boosted Higgs-strahlung at the LHC," *Phys. Rev.* **D98** (2018) no. 9, 095012, arXiv:1807.01796 [hep-ph].

[294] J. de Blas, M. Ciuchini, E. Franco, S. Mishima, M. Pierini, L. Reina, and L. Silvestrini, "Electroweak precision constraints at present and future colliders," *PoS* **ICHEP2016** (2017) 690, arXiv:1611.05354 [hep-ph].

[295] K. Peters, "Prospects for beyond Standard Model Higgs boson searches at future LHC runs and other machines," *PoS* **CHARGED2016** (2017) 028, arXiv:1701.05124 [hep-ex].

[296] **ATLAS, CMS** Collaboration, M. Aaboud *et al.*, "Report on the Physics at the HL-LHC and Perspectives for the HE-LHC," in *HL/HE-LHC Physics Workshop: final jamboree Geneva, CERN, March 1, 2019*. 2019. arXiv:1902.10229 [hep-ex].

[297] F. Kling, T. Plehn, and P. Schichtel, "Maximizing the significance in Higgs boson pair analyses," *Phys. Rev.* **D95** (2017) no. 3, 035026, arXiv:1607.07441 [hep-ph].

[298] W. Kilian, S. Sun, Q.-S. Yan, X. Zhao, and Z. Zhao, "Multi-Higgs Production and Unitarity in Vector-Boson Fusion at Future Hadron Colliders," arXiv:1808.05534 [hep-ph].

[299] W. Bizo?, U. Haisch, and L. Rottoli, "Constraints on the quartic Higgs self-coupling from double-Higgs production at future hadron colliders," arXiv:1810.04665 [hep-ph].

[300] **CMS** Collaboration, V. Khachatryan *et al.*, "Measurement of the associated production of a Higgs boson and a pair of top-antitop quarks with the Higgs boson decaying to two photons in proton-proton collisions at $\sqrt{s} = 13$ TeV," Tech. Rep. CMS-PAS-HIG-18-018, CERN, Geneva, 2018. https://cds.cern.ch/record/2649208.

[301] **CMS** Collaboration, V. Khachatryan *et al.*, "Measurement of the associated production of a Higgs boson with a top quark pair in final states with electrons, muons and hadronically decaying τ leptons in data recorded in 2017 at $\sqrt{s} = 13$ TeV," Tech. Rep. CMS-PAS-HIG-18-019, CERN, Geneva, 2018. https://cds.cern.ch/record/2649199.

[302] J. de Blas, M. Ciuchini, E. Franco, S. Mishima, M. Pierini, L. Reina, and L. Silvestrini, "Electroweak precision observables and Higgs-boson signal strengths in the Standard Model and beyond: present and future," *JHEP* **12** (2016) 135, arXiv:1608.01509 [hep-ph].

[303] C. Englert, R. Kogler, H. Schulz, and M. Spannowsky, "Higgs coupling measurements at the LHC," *Eur. Phys. J.* **C76** (2016) no. 7, 393, arXiv:1511.05170 [hep-ph].

[304] G. Buchalla and O. Cata, "Effective Theory of a Dynamically Broken Electroweak Standard Model at NLO," *JHEP* **07** (2012) 101, arXiv:1203.6510 [hep-ph].

[305] G. Buchalla, O. Catà, and C. Krause, "On the Power Counting in Effective Field Theories," *Phys. Lett.* **B731** (2014) 80–86, arXiv:1312.5624 [hep-ph].

[306] I. Brivio, T. Corbett, O. J. P. Éboli, M. B. Gavela, J. Gonzalez-Fraile, M. C. Gonzalez-Garcia, L. Merlo, and S. Rigolin, "Disentangling a dynamical Higgs," *JHEP* **03** (2014) 024, arXiv:1311.1823 [hep-ph].

[307] M. Klute, R. Lafaye, T. Plehn, M. Rauch, and D. Zerwas, "Measuring Higgs Couplings at a Linear Collider," *EPL* **101** (2013) no. 5, 51001, arXiv:1301.1322 [hep-ph].

[308] K. Hagiwara, R. Szalapski, and D. Zeppenfeld, "Anomalous Higgs boson production and decay," *Phys. Lett.* **B318** (1993) 155–162, arXiv:hep-ph/9308347 [hep-ph].

[309] I. Brivio and M. Trott, "The Standard Model as an Effective Field Theory," arXiv:1706.08945 [hep-ph].

[310] S. Banerjee, S. Mukhopadhyay, and B. Mukhopadhyaya, "Higher dimensional operators and the LHC Higgs data: The role of modified kinematics," *Phys. Rev.* **D89** (2014) no. 5, 053010, arXiv:1308.4860 [hep-ph].

[311] L. Berthier, M. Björn, and M. Trott, "Incorporating doubly resonant $W^{\pm}$ data in a global fit of SMEFT parameters to lift flat directions," *JHEP* **09** (2016) 157, arXiv:1606.06693 [hep-ph].

[312] **ATLAS** Collaboration, G. Aad *et al.*, "Measurements of Higgs boson production and couplings in diboson final states with the ATLAS detector at the LHC," *Phys. Lett.* **B726** (2013) 88–119, arXiv:1307.1427 [hep-ex]. [Erratum: Phys. Lett.B734,406(2014)].

[313] **CMS** Collaboration, S. Chatrchyan *et al.*, "Observation of a new boson with mass near 125 GeV in pp collisions at $\sqrt{s} = 7$ and 8 TeV," *JHEP* **06** (2013) 081, arXiv:1303.4571 [hep-ex].

[314] U. Baur, T. Plehn, and D. L. Rainwater, "Probing the Higgs selfcoupling at hadron colliders using rare decays," *Phys. Rev.* **D69** (2004) 053004, arXiv:hep-ph/0310056 [hep-ph].

[315] J. Brehmer, A. Freitas, D. Lopez-Val, and T. Plehn, "Pushing Higgs Effective Theory to its Limits," *Phys. Rev.* **D93** (2016) no. 7, 075014, arXiv:1510.03443 [hep-ph].

[316] A. Helset and M. Trott, "Equations of motion, symmetry currents and EFT below the electroweak scale," arXiv:1812.02991 [hep-ph].

[317] **ATLAS** Collaboration, M. Aaboud *et al.*, "Combination of searches for Higgs boson pairs in *pp* collisions at 13 TeV with the ATLAS experiment.,".

[318] **ATLAS** Collaboration, M. Aaboud *et al.*, "Constraint of the Higgs boson self-coupling from Higgs boson differential production and decay measurements," Tech. Rep. ATL-PHYS-PUB-2019-009, CERN, Geneva, Mar, 2019. http://cds.cern.ch/record/2667570.

[319] V. Barger, T. Han, P. Langacker, B. McElrath, and P. Zerwas, "Effects of genuine dimension-six Higgs operators," *Phys. Rev.* **D67** (2003) 115001, arXiv:hep-ph/0301097 [hep-ph].

[320] W. Bizon, M. Gorbahn, U. Haisch, and G. Zanderighi, "Constraints on the trilinear Higgs coupling from vector boson fusion and associated Higgs production at the LHC," *JHEP* **07** (2017) 083, arXiv:1610.05771 [hep-ph].

[321] F. Maltoni, D. Pagani, A. Shivaji, and X. Zhao, "Trilinear Higgs coupling determination via single-Higgs differential measurements at the LHC," *Eur. Phys. J.* **C77** (2017) no. 12, 887, arXiv:1709.08649 [hep-ph].

[322] **Physics of the HL-LHC Working Group** Collaboration, M. Cepeda *et al.*, "Higgs Physics at the HL-LHC and HE-LHC," arXiv:1902.00134 [hep-ph].

[323] A. Hocker, H. Lacker, S. Laplace, and F. Le Diberder, "A New approach to a global fit of the CKM matrix," *Eur. Phys. J.* **C21** (2001) 225–259, arXiv:hep-ph/0104062 [hep-ph].

[324] F. Cascioli, T. Gehrmann, M. Grazzini, S. Kallweit, P. Maierhöfer, A. von Manteuffel, S. Pozzorini, D. Rathlev, L. Tancredi, and E. Weihs, "ZZ production at hadron colliders in NNLO QCD," *Phys. Lett.* **B735** (2014) 311–313, arXiv:1405.2219 [hep-ph].

[325] M. Grazzini, S. Kallweit, D. Rathlev, and M. Wiesemann, "$W^{\pm}Z$ production at hadron colliders in NNLO QCD," *Phys. Lett.* **B761** (2016) 179–183, arXiv:1604.08576 [hep-ph].

[326] T. Gehrmann, M. Grazzini, S. Kallweit, P. Maierhöfer, A. von Manteuffel, S. Pozzorini, D. Rathlev, and L. Tancredi, "W^+W^- Production at Hadron Colliders in Next to Next to Leading Order QCD," *Phys. Rev. Lett.* **113** (2014) no. 21, 212001, arXiv:1408.5243 [hep-ph].

[327] M. Czakon and A. Mitov, "Top++: A Program for the Calculation of the Top-Pair Cross-Section at Hadron Colliders," *Comput. Phys. Commun.* **185** (2014) 2930, arXiv:1112.5675 [hep-ph].

[328] "Top quark pair cross section." https://twiki.cern.ch/twiki/bin/view/LHCPhysics/TtbarNNLO#Top_quark_pair_cross_sections_at. [Accessed: 2017-12-01].

[329] M. Grazzini, S. Kallweit, and D. Rathlev, "ZZ production at the LHC: fiducial cross sections and distributions in NNLO QCD," *Phys. Lett.* **B750** (2015) 407–410, arXiv:1507.06257 [hep-ph].